UNIVERSIDADE DE LISBOA
FACULDADE DE CIÊNCIAS
DEPARTAMENTO DE FÍSICA

ATLAS JET TRIGGER: PERFORMANCE AND *IN-SITU* CALIBRATION STUDIES

Joana Machado Miguéns

MESTRADO EM FÍSICA
(Área de Especialização em Física Nuclear e Partículas)

2009

UNIVERSIDADE DE LISBOA
FACULDADE DE CIÊNCIAS
DEPARTAMENTO DE FÍSICA

ATLAS JET TRIGGER: PERFORMANCE AND *IN-SITU* CALIBRATION STUDIES

Joana Machado Miguéns

MESTRADO EM FÍSICA
(Área de Especialização em Física Nuclear e Partículas)

Dissertação orientada por: Professora Doutora Amélia Maio
Co-orientada por: Doutora Patricia Conde Muíño

2009

Abstract

The LHC at CERN will provide collisions of proton beams with a pioneer energy of 14TeV and an unprecedented luminosity of $10^{34}\text{cm}^{-2}\text{s}^{-1}$, extending the frontiers of Particle Physics.

ATLAS is a general-purpose detector, designed to cover the widest range of physics possible by analyzing the myriad of particles produced by the LHC.

Collision data from the LHC will be delivered to ATLAS at an unsustainable rate of 40MHz. Working in three steps, the ATLAS trigger system will effectively reject uninteresting events, still maintaining an excellent and unbiased efficiency for rare signals, in order to reduce the input rate to a manageable 200Hz.

Hadronic jets will be among the most commonly produced objects at the LHC. They will represent, at the same time, signatures for many physics processes and background for nearly every physics analysis. Thus, the performance of the trigger system depends heavily on its ability to reconstruct jets. Moreover, precise jet reconstruction cannot be achieved without energy calibration, which is why the energy of trigger jet is calibrated at Level-2.

The work presented in this thesis was developed in two steps.

First, the performance of the ATLAS jet trigger system was evaluated using data from cosmic muon runs. This was done by comparing the properties of the jets reconstructed by the trigger and reconstructed offline. The analysis was simple but, nonetheless, powerful, since it allowed the identification of noisy cells and calibration problems.

For the second study, a *in-situ* calibration method was applied to MonteCarlo simulated jets to evaluate if the method can be used with real collision data to validate and tune the calibration applied to Level-2 trigger jets.

The method, named intercalibration in η, proved capable of improving the Level-2 jet energy scale up to an uncertainty of 1% for jets with transverse momenta above 1TeV. Furthermore, the analysis strongly suggests that the method can be used with real data for the same purposes.

Keywords: CERN, LHC, ATLAS, hadronic jets, trigger, *in-situ* calibration.

Resumo

O LHC no CERN vai provocar colisões de feixes de protões em condições sem precedentes - energia de 14TeV e luminosidade de $10^{34}\mathrm{cm}^{-2}\mathrm{s}^{-1}$ - alargando as fronteiras da Física de Partículas

ATLAS é um detector de carácter genérico, concebido para identificar a míriade de particulas produzidas no LHC, cobrindo um vasto leque de processos de física.

ATLAS receberá dados das colisões no LHC a uma taxa insustentável de 40MHz. O sistema de *trigger* de ATLAS actua em três níveis para rejeitar eventos, mantendo-se eficaz na detecção de processos de física interessantes e de sinais raros, reduzindo a taxa para 200Hz.

No LHC os jactos hadrónicos serão dos objectos produzidos em maior abundância. Para ATLAS, os jactos são, por um lado, assinaturas de processos físicos relevantes e, por outro, fundo para a maior parte das análises de física. Assim, o desempenho do sistema de *trigger* depende fortemente da sua capacidade de reconstruir jactos. Para além disso, uma reconstrução precisa requer calibração da energia dos jactos, que a nível do *trigger* é efectuada no Level-2.

O trabalho apresentado nesta tese foi desenvolvido em duas partes.

Primeiro, o desempenho do *trigger* de jactos de ATLAS foi avaliado com dados de *runs* de muões cósmicos. A avaliação foi feita comparando as propriedades dos jactos reconstruídos pelo *trigger* e reconstruídos *offline*. Apesar de simples, a análise mostrou-se poderosa, permitindo a identificação de células ruidosas e problemas de calibração do detector.

Para o segundo estudo, aplicou-se um método de calibração *in-situ* a jactos simulados de MonteCarlo, por forma a determinar se o método pode ser utilizado com dados reais de colisões para validar e afinar a calibração

aplicada aos jactos do Level-2 do *trigger*. Com este método, designado por "intercalibração em η", foi possível melhorar a incerteza na escala de energia dos jactos do Level-2 com momentos transversos superiores a 1TeV até 1%. Para além disso, análise feita sugere fortemente que resultados semelhantes podem ser obtidos com a aplicação do método a dados reais.

Palavras Chave: CERN, LHC, ATLAS, jactos hadrónicos, *trigger*, calibração *in-situ*.

Resumo Alargado

Trigger de Jactos de ATLAS: Estudos de Desempenho e de Calibração *In-situ*

Os quarks, partículas elementares que constituem os hadrões, de que é exemplo o protão, nunca foram observados isoladamente. As tentativas ao longo da história de "quebrar" protões de forma a poder observar isoladamente os seus constituintes fundamentais levaram à descoberta dos jactos. De facto, os quarks estão confinados no interior dos hadrões. Quando se tenta separar um quark de um hadrão, o resultado é um "chuveiro" de partículas variadas que emerge na direcção esperada para o quark. Essas partículas podem ser mesões, bariões, leptões, fotões e constituem aquilo a que se chama um jacto. O processo pelo qual os quarks originam jactos é denominado hadronização. Os jactos são uma evidência experimental e, como tal, foram incorporados na teoria que descreve as interacções entre quarks e gluões ou interacções fortes - a cromodinâmica quântica (QCD).

Uma explicação rudimentar para o fenómeno da hadronização envolve o modo como a interacção forte evolui com a distância entre as partículas. Ao contrário da interacção electromagnética, como por exemplo a interacção entre um electrão e um positrão que é tanto menos intensa quanto mais eles se afastam, a intensidade da interacção forte diminui para distâncias muito curtas, sendo que os quarks são praticamente livres nestas condições. A este fenómeno dá-se o nome de liberdade assimptótica. Por outras palavras, ao tentar afastar, por exemplo, um quark de um anti-quark, a energia potencial vai aumentando. Quando a distância entre eles é "grande", essa energia é convertida num conjunto de várias partículas a que chamamos jacto. É de notar que este raciocínio também se pode aplicar a gluões, i.e., os bosões

mediadores da interacção forte. Ao contrário dos fotões, que são os bosões mediadores da interacção electromagnética, não têm carga eléctrica e não podem, portanto, interagir entre si, os gluões têm cor e "sentem" a interacção forte, podendo interagir entre eles. O resultado é que os jactos são não só a assinatura dos quarks mas também dos gluões, ou, genericamente, dos partões.

A nível experimental, quando um jacto é produzido, por exemplo num colisionador protão-protão como o LHC, o que se observa são os traços e as deposições de energia que as partículas que o constituem deixam nos detectores de traços e nos calorímetros dos detectores de partículas. O jacto, em si, tem que ser reconstruído. O objectivo de reconstrução é determinar as propriedades do partão que originou o jacto com base nas propriedades do jacto. A reconstrução é feita com base numa definição apresentada sob a forma de um algoritmo de jacto. Um algoritmo de jacto de cone, por exemplo, usa a informação dos calorímetros e agrupa as deposições de energia deixadas pelas partículas num cone, formando o jacto a nível de calorímetro. O passo seguinte da reconstrução envolve a calibração da energia do jacto. Primeiro, aplicam-se correcções para desconvoluir os efeitos do calorímetro sobre as partículas que constituem o jacto. Após estas correcções obtém-se um jacto a nível de partículas. Mais correcções podem, por fim, ser aplicadas para corrigir os efeitos físicos como os da hadronização, de forma a obter o jacto a nível do partão que o originou.

O Large Hadron Collider (LHC) é o mais recente acelerador de partículas do CERN. No interior do seu anel, com 27km de perímetro, circularão dois feixes de protões em direcções opostas, a uma velocidade que atingirá 99.999% da velocidade da luz. No LHC os feixes cruzar-se-ão gerando colisões protão-protão (pp) em condições de luminosidade e energia sem precedentes, que poderão mudar o rumo da Física de Partículas, permitindo não só medidas precisas de fenómenos já conhecidos, bem como a descoberta de novos fenómenos. Em particular, as colisões vão dar-se a uma luminosidade de $10^{34}\mathrm{cm}^{-2}\mathrm{s}^{-1}$, com uma energia de centro de massa de $\sqrt{s} = 14\mathrm{TeV}$ e a uma taxa de $\approx 40\mathrm{MHz}$. Estas são as condições de funcionamento previstas para o LHC mas, na realidade, o acelerador entrará em funcionamento no final do presente ano 2009, com uma energia do centro de massa de 7TeV e uma luminosidade de aproximadamente $10^{31}\mathrm{cm}^{-2}\mathrm{s}^{-1}$.

As colisões no LHC ocorrerão em quatro pontos, onde quatro detectores de partículas, com características distintas, estão colocados de forma a identificar os resultados das colisões. Um desses detectores é ATLAS (A Toroidal LHC Apparatus), um detector de carácter geral, concebido para explorar todo o potencial oferecido pelas colisões no LHC. O detector ATLAS é, basicamente, constituído por várias camadas de subdetectores construídas em torno do ponto de colisão e por um sofisticado sistema magnético. Os subdetectores incluem detectores de traços (o Detector Interno e as Câmaras de Muões), que permitem determinar as trajectórias e, em conjunto com o sistema magnético, os momentos das partículas, e calorímetros, que fornecem as medidas das energias. O sistema de calorímetros de ATLAS é particularmente importante para o trabalho desenvolvido, dado que é nos calorímetros que se inicia a reconstrução dos jactos. Em ATLAS há dois tipos de calorímetros que usam tecnologias diferentes para atingir diferentes objectivos. Os calorímetros electromagnético e hadrónico na zona *forward* do detector, também chamados LAr por utilizarem árgon líquido, e o calorímetro hadrónico, ou TileCal, que funciona à base de telhas cintilantes e fibras ópticas na zona central do detector.

O LHC vai cruzar pacotes de protões a uma taxa de $\approx$ 40MHz. Ao cruzamento de dois pacotes chama-se evento e de cada evento podem resultar mais de 20 colisões *pp*. Porque é impossível para o detector ATLAS guardar e analisar toda a informação referente às colisões e também porque na maior parte dos casos resultarão eventos de pouco interesse, i.e. os eventos "mais interessantes" têm secções eficazes de produção baixas, ATLAS possui um sistema de *trigger* cujo objectivo é rejeitar eventos em tempo real, de modo a reduzir a taxa a que a informação é produzida. Nas condições de funcionamento do LHC, jactos serão dos objectos produzidos com maior frequência. Estes poderão constituir tanto sinal como fundo para vários processos de física, pelo que é essencial que o sistema de *trigger* tenha a capacidade de identificar e reconstruir jactos num evento. Para além disso, um evento rejeitado pelo *trigger* é eliminado permanentemente, pelo que este sistema têm que ser robusto e apresentar um elevado desempenho.

O sistema funciona em três níveis, sendo que cada nível melhora a decisão do anterior. No final, a taxa de informação de $\approx$ 40MHz é reduzida para $\approx$ 200Hz. O primeiro nível, denominado Level-1 ou LVL1, funciona

a nível de *hardware* e começa por procurar a informação contida nos subsistemas do detector ATLAS. Em particular, procura deposições de energia nos calorímetros que possam ser candidatas a jactos. A partir dessa informação, o LVL1 define regiões de interesse (RoI's), i.e., coordenadas do detector onde foram identificados candidatos a jactos. Depois de tomar uma decisão e eliminar eventos até uma taxa de $\approx$ 75kHz, o LVL1 passa a informação dessas RoI's para o nível seguinte do *trigger*. O segundo nível do *trigger* (Level-2 ou LVL2), em conjunto com o último nível (Event Filter ou EF), formam o HLT (High Level Trigger), que faz a identificação e reconstrução de jactos a nível de *software*. O LVL2 usa as informações contidas nas RoI's como ponto de partida para iniciar a reconstrução dos jactos, utilizando um algoritmo de cone com 0.4 de raio no espaço (η, ϕ) do detector. A reconstrução é melhorada pela aplicação de uma calibração à energia dos jactos e a taxa é reduzida até $\approx$ 1kHz. O EF, por sua vez, utiliza um algoritmo de reconstrução de cone com 0.7 de raio, mais complexo e semelhante àquele que pode ser utilizado na reconstrução *offline*, para fornecer o último passo de rejeição *online*, reduzindo a taxa para $\approx$ 200Hz passíveis de armazenamento.

Os estudos apresentados nesta tese foram motivados pela necessidade de o *trigger* de jactos de ATLAS se apresentar robusto, eficaz e fiável. O objectivo era simples: tentar avaliar e melhorar o desempenho deste sistema de *trigger*. Dado que o LHC ainda não está a produzir colisões *pp*, usaram-se dados de muões cósmicos e dados simulados de MonteCarlo na análise, que se desenvolveu em duas fases.

Numa primeira fase avaliou-se o desempenho dos três níveis do *trigger* de jactos de ATLAS, sendo que o estudo também permitu um bom teste à qualidade dos dados de muões cósmicos, que foram usados para imitar as deposições de energia que os jactos hadrónicos deixam nas células dos calorímetros. Em particular, apresenta-se a análise efectuada para o *run* de muões cósmicos 90272. A avaliação do desempenho do *trigger* de jactos foi feita comparando a reconstrução dos jactos feita pelo *trigger* com a reconstrução realizada *offline*, considerada a melhor disponível. Apesar de a análise ser simples, revelou-se bastante poderosa na identificação de problemas que podem influenciar o desempenho do *trigger* de jactos, como se mostra de seguida.

A primeira análise consistiu numa avaliação da reconstrução de cada nível do *trigger* de jactos e *offline* separadamente. Por um lado, esta análise permitiu a confirmação do modo de funcionamento do *trigger* e de vários aspectos relacionados com jactos. Em particular, verificou-se que o número eventos diminui à medida que o número de jactos por evento aumenta, que o número de jactos diminui à medida que a energia dos jactos aumenta, que os jactos são reconstruidos maioritariamente em posições centrais de η no detector e que se distribuem uniformemente em ϕ. Por outro lado, a análise conduziu à identificação de alguns problemas. Por exemplo, o HLT não incluía a zona forward do detector ATLAS, a energia dos jactos reconstruídos *offline* não se encontrava calibrada e o LVL2 só estava a calibrar jactos com $E_t > 20$GeV. Quanto ao último assunto, foi corrigido posteriormente a esta análise, pelo que *runs* de muões cósmicos recentes já não apresentam este problema. No entanto, o aspecto mais importante da análise foi, provavelmente, ter levado à identificação de células ruidosas dos calorímetros de ATLAS. Jactos reconstruídos a partir desta células ruidosas foram encontrados em todos os níveis do *trigger* e também na reconstrução *offline* e foram removidos para que a análise subsequente não fosse influenciada.

A análise continuou com uma comparação mais directa entre as reconstruções efectuadas pelo *trigger* e *offline*, que foi feita emparelhando jactos do *trigger* e jactos *offline*. Este emparelhamento permitiu, por exemplo, a avaliação da precisão espacial na reconstrução da posição dos jactos feita pelo *trigger*. Em particular, confirmou-se que cada nível do *trigger* melhorava a reconstrução da posição do jacto efectuada pelo nível anterior. Também se verificou que a granularidade disponível para a reconstrução no LVL1 afecta a precisão espacial na reconstrução. Depois analisou-se a reconstrução da energia, o que permitiu a identificação de um problema na reconstrução *offline*. De facto, a energia dos jactos *offline* identificados na zona do TileCal com $|\eta| > 1.0$ estava sobrestimada, um problema que foi resolvido posteriormente. Apesar deste problema, a escala de energia do *trigger* mostrou-se estável na zona mais central do detector, sendo que o LVL2, por exemplo, estava a reconstruir $\approx 95\%$ da energia *offline*.

A análise final foi motivada pelo que acontece durante a monitorização *online* dos *runs* e da aquisição de dados, quando a reconstrução *offline*

ainda não se encontra disponível. Assim, jactos do LVL1 e LVL2 do *trigger* foram emparelhados com jactos do EF. A avaliação feita com estes pares foi semelhante à avaliação feita com os pares *trigger-offline* e os resultados observados foram também similares. Em particular, a comparação entre as energias reconstruidas pelo LVL2 e pelo EF indicaram que ou a calibração aplicada aos jactos no LVL2 está a sobrestimar a energia real dos jactos ou o EF está a subestimá-la.

Numa segunda fase, desenvolveram-se estudos utilizando um método de calibração *in-situ* designado por "intercalibração em η". O método permite a validação e ajuste da calibração hadrónica aplicada à energia dos jactos através da avaliação e correcção da estabilidade em η da escala de energia hadrónica. É um método relativo, dado que jactos de prova são comparados a jactos de referência e corrigidos em função destes. A variável assimetria, A, foi usada como um indicador da estabilidade da escala de energia. O método foi usado em eventos de dois jactos simulados em PYTHIA, com o objectivo de avaliar se podia ser usado com dados reais de colisões para validar e afinar a calibração aplicada aos jactos do *trigger* no LVL2. De notar que esta calibração foi criada com base em eventos simulados, pelo que, certamente, não será perfeita para dados reais, no sentido em que não calibrará a escala de energia do LVL2 ao nível de partículas.

Os estudos iniciaram-se com a aplicação do método a jactos *truth*, i.e. jactos simulados reconstruídos directamente a nível de partículas, que constituem a referência para a calibração dos jactos do LVL2. Por outras palavras, se a calibração aplicada aos jactos do LVL2 for "perfeita", espera-se que as assimetrias destes jactos estejam contidas no mesmo intervalo que as assimetrias dos jactos *truth*. Os resultados mostraram que as assimetrias variam de acordo com o momento transverso dos jactos e são, normalmente, menores para alto p_t. Os resultados também sugeriram um ligeiro desvio para valores positivos de A nas zonas menos centrais do detector. Tal foi interpretado como uma consequência do facto de os algoritmos de cone não recolherem todas a partículas de jactos de baixo momento transverso, dado de estes tendem a ser mais largos e não tão colimados.

O passo seguinte consistiu em aplicar o método a jactos simulados do LVL2. As assimetrias observadas para estes jactos levaram à conclusão de que a calibração aplicada no LVL2 não era apropriada, dado que não pro-

duzia uma escala de energia estável e uniforme em η. Assim, o método de intercalibração em η foi, de seguida, usado para calcular as constantes de correcção à calibração do LVL2, com o objectivo de tentar reduzir as assimetrias observadas. Os resultados obtidos sugerem que, de facto, este método de calibração *in-situ* tem capacidade para melhorar a escala de energia do LVL2, dado que as assimetrias observadas nos jactos corrigidos estavam bastante reduzidas, particularmente em jactos de elevado momento transverso. Dado que estavam a ser usados dados simulados, o teste final consistiu em verificar, de facto, que a escala de energia do LVL2 era mais estável e uniforme em η depois de aplicadas as correcções calculadas através do método intercalibração em η. O teste confirmou que, de facto, a escala de energia melhora significativamente, especialmente para jactos de alto p_t, onde foi possível obter uma incerteza melhor que 1%.

Por fim, realizou-se um estudo para tentar determinar se o método pode, de facto, ser aplicado com dados reais de colisões no inicio da aquisição de dados do LHC e produzir os mesmos resultados. Para tal, avaliaram-se as eficiências dos cortes de selecção necessários à aplicação do método, bem como a variação da incerteza estatística com a luminosidade integrada no LHC. Observou-se que para jactos num intervalo de momento transverso de $[90, 120]$GeV é possível atingir uma incerteza estatística comparável com a incerteza obtida para escala de energia com $\approx 50\text{pb}^{-1}$ de luminosidade integrada. Para além disso, o *trigger* de jactos fará a selecção de eventos de forma a que a taxa de jactos identificados seja constante em função do momento transverso, o que leva a crêr que se podem esperar resultados e incertezas semelhantes para jactos noutros intervalos de p_t.

Acknowledgements

First and foremost, I want to thank Professor Amélia Maio, Team Leader of the portuguese ATLAS group, for taking me in at Laboratório de Intrumentação e Física Experimental de Partículas and introducing me to the world of Experimental Particle Physics, but mostly for the dedicated supervision of my work and genuine concern for my learning and my future.

I sincerely thank Patricia Conde Muíño for the way she guided my work during the last year. For everything she taught me, for the patience she always had to answer my naive questions, for being so available... Thank you.

I take this opportunity to thank my ATLAS colleagues at LIP - Mara, Pedro, Alberto, Agostinho, João Gentil, João Pina, Zé e Nuno Anjos - they were always ready to help me. I especially thank António and Nuno, who were working on their Master's thesis as I was working on mine, for the laughs that destroyed many brain cells. I would also like to thank Sandra, for always having a smile ready.

Thank you, Kaggy, for being who you are and knowing me so well.

I thank Sushi, for the moveable feast (and its aftermath) and for the comfortable silences.

I thank Kelly, Luís, Manel, Simon, Tiago, Sandra and Marta, for all the coffees, for all the dinners, for all the nights at Bairro, for all the talks... for all the friendship.

To Simão, merci.

I would also like to thank Aninhas, Jo and Carlota, for the friendship and company when the journey through Physics was just starting.

I wish to thank all my friends who kept asking me "how's the work going?" and encouraging me, especially Sofs, Flor, Carlinha, Dori, Janeka,

Pipa, Ricardo, Txinha, Guida, Marta, Sílvia, Catarina, Sofia, António and les amis Erasmus.

Thank you Pipas, for receiving me so well. Your company during the last year has been priceless.

I thank Paula, Manel and Tê, for they were also a part of this.

I thank my brother Gué and my sister Titi, because I need them and they are always with me.

And last, but certainly not least, I deeply thank my Parents, who always encouraged my to make my own decisions and support me unconditionally. Thank you Dad, you were always there, indeed. Thank you Mom, for every, every, every, every single thing and more, but mostly for enduring me this past year.

Thank you all, I know I could not have done it without you.

Contents

List of Figures

List of Tables

Introduction

A new accelerator at CERN, the LHC, will collide beams of protons with unprecedented conditions of energy and luminosity, extending the frontiers of high-energy physics. ATLAS is a general-purpose detector designed to cover the widest range of physics possible at the LHC. The LHC will deliver collision data at a rate of 40MHz. Thus, one fundamental system in ATLAS is the trigger, that reduces the data flow to a manageable storage rate of 200Hz.

At the LHC jets will be the most commonly produced objects. Properly identifying, calibrating and reconstructing hadronic jets in an event is a fundamental task of the ATLAS jet trigger. This, however, represents a great challenge for ATLAS, particularly because jets may constitute signatures or background, depending on the physics process.

The need for an extremely efficient jet trigger in ATLAS motivated the work presented in this thesis, which is divided in two parts. The goal is simple: to assess and develop methods to improve the performance of the ATLAS jet trigger. Because the LHC is not yet producing pp collisions, cosmic muon data and MonteCarlo simulations were used for the analysis.

First, cosmic muon runs were used to evaluate the performance of the three levels of the ATLAS trigger system in reconstructing the energy and position of the jets. The evaluation was done by comparison between the trigger reconstruction and the offline reconstruction.

In the second study a *in-situ* calibration method, called intercalibration in η, was applied to MonteCarlo simulated data. The plan was to try to determine if the method could be used with real collision data to validate and tune the calibration applied to trigger jets at Level-2. In particular, the ability for that calibration to produce a jet energy scale uniform in η was

evaluated.

The outline of this thesis is as follows. In Chapter 1, the Physics' aspects relevant to the work, mostly related to the subject of jets, are briefly presented. A more technical description of the ATLAS Experiment is presented in Chapter 2. Chapter 3 is devoted to explaining how jets are handled in ATLAS. Finally, Chapters 4 and 5 describe the studies done and the results obtained on the performance of the ATLAS jet trigger.

Chapter 1

Physics Motivation

1.1 Introduction to the Standard Model of Particle Physics

Particle physics deals with the study of the most fundamental constituents of matter and the nature of the interactions between them. However, which particles are regarded as fundamental has changed (and continues to change) with time, as physicists' knowledge increases. The current view, described by a theory referred to as the Standard Model (SM), is, nonetheless, very simplistic and encompasses two basic ideas. First, all matter is composed of fermions, i.e., $\frac{1}{2}$-spin particles[1]. Second, these fermions interact with each other by exchanging bosons, which are integral-spin particles[1] [1].

Addressing the fermionic sector first, particles can be divided into two families according to their physical properties: leptons (l), which have integral electric charges, and quarks (q), which carry fractional electric charges [2].

The most familiar example of a lepton is the electron e^-, but, in reality, six more leptons exist. They can be classified according to their physical properties (namely the electric charge Q and mass m) and quantum numbers - electron number (L_e), muon number (L_μ) and tau number (L_τ) - and fall naturally into three generations. This information is summarized in table 1.1. Actually, six more leptons exist, since each particle in table 1.1 has

[1] All particles in the Standard Model are assumed to be elementary, meaning they are treated as point particles, without internal structure or excited states.

an antiparticle pair. Thus, a similar table could be built for the antileptons, the only difference being that all the signs would be reversed. The positron e^+ for example, carries an electric charge of +1 and has $L_e = -1$. So, in summary, a total of 12 different leptons exist [3].

Leptons						
Generation	*Flavor*	*Mass*	Q	L_e	L_μ	L_τ
First	Electron, e	0.511MeV	-1	1	0	0
	Electron Neutrino, ν_e	< 2eV	0	1	0	0
Second	Muon, μ	105.658MeV	-1	0	1	0
	Muon Neutrino, ν_μ	< 2eV	0	0	1	0
Third	Tau, τ	1776.84MeV	-1	0	0	1
	Tau Neutrino, ν_τ	< 2eV	0	1	0	1

Table 1.1: Classification and properties of leptons [4].

As for the quarks, they can be organized similar to the leptons. In particular, six different flavors of quarks exist, they can be distinguished by their physical properties and quantum numbers and fall into three generations as well. For quarks, the quantum numbers are strangeness (S), charm (C), beauty (B), and truth (T). Table 1.2 summarizes the main properties of the quarks. Again, all signs in this table could be reversed to create a table for the antiquarks. Moreover, and this is a property that does not exist in leptons, each quark can carry one of three color charges - red, green and blue. The result is that a total of 36 different quarks exist [3].

Quarks							
Generation	*Flavor*	*Mass*	Q	C	S	T	B
First	Up, u	$1.5 - 3.3$MeV	$2/3$	0	0	0	0
	Down, d	$3.5 - 6.0$MeV	$-1/3$	0	0	0	0
Second	Charm, c	≈ 1.27GeV	$2/3$	1	0	0	0
	Strange, s	≈ 104MeV	$-1/3$	0	-1	0	0
Third	Top, t	≈ 171.2GeV	$2/3$	0	0	1	0
	Bottom, b	≈ 4.20GeV	$-1/3$	0	0	0	-1

Table 1.2: Classification and properties of quarks [4].

Let us move now into the bosonic sector, which includes the elementary particles referred to as force mediators. The basic idea is that only four forces exist in nature - strong, electromagnetic, weak and gravitational - and each one is described by a different theory. These are the forces by which the fermions interact with each other and they do so by exchanging a force mediator. In other words, the mediators carry/transmit the force from one interacting fermion to the other. Basically, mediators do so by coupling with the charges of the interacting fermions with a given coupling constant. Thus, the strength of a given interaction is determined by the value of its coupling constant. Table 1.3 summarizes the most relevant features of the Standard Model bosons. These will be developed next. [3]

Fundamental Forces				
Interactions	Strong	Electro-magnetic	Weak	Gravitational
Charge	Color	Electric Charge	Weak Charge	Mass
Relative Coupling	10	10^{-2}	10^{-13}	10^{-42}
Mediators	8 Gluons, g	Photon, γ	W^-, W^+ and Z	Graviton
Fermion Couplings	quarks	all except neutrinos	all	all

Table 1.3: Classification and properties of the fundamental forces [4].

The strong interaction, described by the theory of Quantum Chromodynamics (QCD) is, as suggested by the name, the strongest of the four interactions. It is mediated by the gluon (g), a spin-0, massless, neutral, elementary particle. At this point, it is important to say that gluons, as quarks, carry a color charge, which results in eight different gluons existing in nature. The color charge is, actually, the charge of the strong force, in the sense that only colored particles can interact strongly. Thus, the strong interaction is exclusive to quarks and gluons.

Quantum Electrodynamics (QED) is the oldest, simplest and most successful of the four theories and describes the electromagnetic interaction.

The electromagnetic mediator is the photon (γ), which, similarly to the gluon, has 0 spin, no mass and no electric charge. The photon can only couple to electrically charged particles, which means that neutrinos are excluded from these interactions [3].

Weak interactions are described by Flavordynamics. The weak coupling constant is smaller than the strong coupling constant and the fine-structure constant (electromagnetic coupling constant), making the weak force weaker than the strong and electromagnetic forces. All quarks and leptons carry the "weak charge"[2], which means that all of them can couple to the force mediators and interact weakly. There are three different weak mediators: W^+, W^- and Z. These bosons have spin-1, each one carries a different electric charge and, unlike the previous bosons, are very massive particles [3].

Gravity is the weakest of all four interactions. Classically it is described by Newton's law of universal gravitation and its relativistic generalization is Einstein's theory of relativity. However, a completely satisfactory quantum theory of gravity has not yet been worked out. Gravitons (gravity mediators) are hypothesized but, in reality, gravity is neglected in the field of elementary particles simply because it is too weak to play a significant role [3].

This short description of the SM would not be complete without mentioning the Higgs boson, a massive particle with no intrinsic spin. Basically this boson is necessary in the SM to account for the masses of all elementary particles. In other words, without the Higgs, all particles would be massless, which experiment has shown not to be true. It is the coupling between the Higgs boson and the particles (including the Higgs itself) that generates their masses [1].

Currently, the Standard Model is in full agreement with the available experimental data accumulated over the past three decades. Actually, the SM provides some of the best agreements between theory and experiment in physics[3]. Nonetheless, physicists know it is not a complete theory. For example, the masses of SM particles are empirical numbers taken from experiment. This and other examples add up and the result is the SM has

[2]Quotation marks are used because no particular name exists for this charge

[3]SM predicted the anomalous magnetic moment of the electron in agreement with the experimental measurement up to 9 decimal places.

over 20 arbitrary parameters. Then, there is the opposite situation, where theoretical predictions have not yet been experimentally observed, such as the existence of the Higgs boson. Consequently, and despite its success, the interest in possible extensions or alternatives to the Standard Model continues to grow [5].

1.2 Jet Physics

1.2.1 Jet Phenomenology

As mentioned in the previous section, Quantum Chromodynamics (QCD) is the theory that describes the strong interactions that occur between color-charged particles. These can be quarks (q) or gluons (g) and they will be referred to as partons [6].

It is hypothesized in QCD that every naturally occurring particle should be a color singlet. This is called color confinement and it has several consequences. For example, it explains why isolated quarks have never been observed and why they only exist in bound states forming colorless systems - the hadrons. Also, it is the reason why only two types of hadrons are known. To produce a composite particle with no color, quarks can only be confined in two ways. Thus, there are only mesons - a quark and anti-quark bound state - and the baryons, formed by three quarks or three anti-quarks [7].

Although never derived from the theoretical QCD background, the experimental observations mentioned in the previous paragraph support the idea of color confinement. Furthermore, some theoretical considerations indicate that the hypothesis is valid. In particular, the energy (or distance) dependence of the strong coupling constant, α_s (figure 1.1).

The increase of α_s for low energies, or equivalently the increase of the strong interaction strength for long distances, strongly suggests the idea of quarks being clumped together, since trying to separate them would greatly increase the energy of the system [7].

Another important feature of α_s is that it decreases at very high energies, which is why the strong interaction strength vanishes at very short distances. Thus, as two quarks come closer and closer together, the strong force binding them weakens. This is called asymptotic freedom and it also suggests that

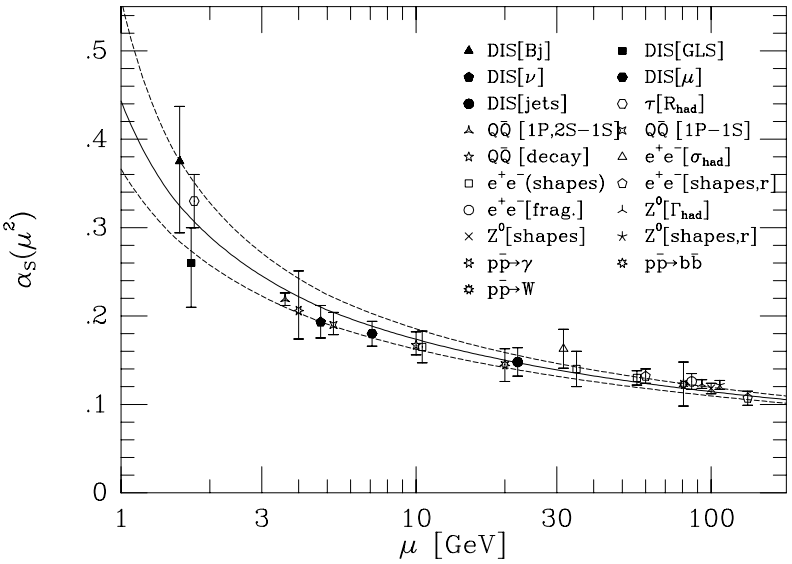

Figure 1.1: Energy dependence of the strong coupling constant α_s (combined results from several experiments) [8].

bound states of quarks are more stable than separated quarks, since they are almost "free" [7].

One way to explain asymptotic freedom in QCD is to compare color-charge to QED charge. Take, for example, an electron. Its observed charge becomes smaller at larger distances or, in other words, the electric field weakens with the increasing distance. This is because of the screening of the electric charge by vacuum polarization, which is depicted in figure 1.2. What happens in QED is that the vacuum constantly sprouts particle-antiparticle pairs, such as electron-positron pairs, behaving like a dielectric medium. As the electron is placed in this dielectric vacuum, the positrons of the pairs will be attracted, while the electrons will be repelled, causing the vacuum to polarize. The average effect of this behavior is to partially cancel the field created by the electron. Thus, as one moves closer and closer to the electron, the screening effect starts disappearing, increasing the effective charge of the electron [3].

Comparatively to QED screening, the color of a quark is also shielded by the creation of quark-antiquark pairs in the vacuum. Nevertheless, there

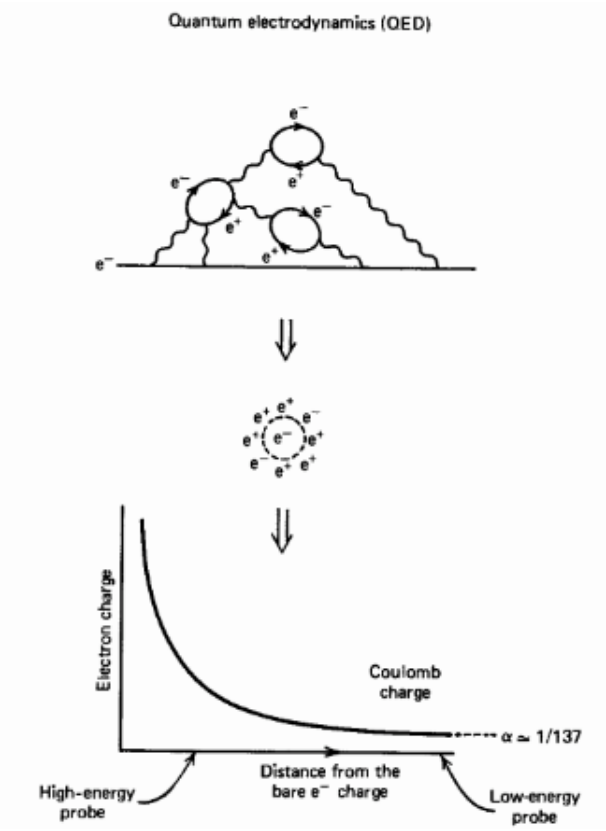

Figure 1.2: Screening of the electric charge in QED [9].

is a fundamental difference between QED and QCD. The mediators of an electric interaction, the photons, have no electric charge, whereas the mediators of the strong interaction, the gluons, carry themselves a color charge. This means, for example, that gluons can couple between them and photons cannot. In fact, the emission of virtual gluons in the vacuum suppresses the emission of quark-antiquark pairs. Also, because gluons actually carry two color charges, they end up not screening the color field but rather increasing it. This is often referred to as antiscreening and is portrayed in figure 1.3. QCD antiscreening dissipates as one moves closer to the quarks, just as the screening effect for an electric charge. However, in QCD, the effective charge of the quark decreases. In summary, as the distance is increased, the strong interaction is strengthened, whereas for short distances the strong interaction field is very weak and quarks are nearly "free" particles [3].

The properties of color confinement and asymptotic freedom have a very

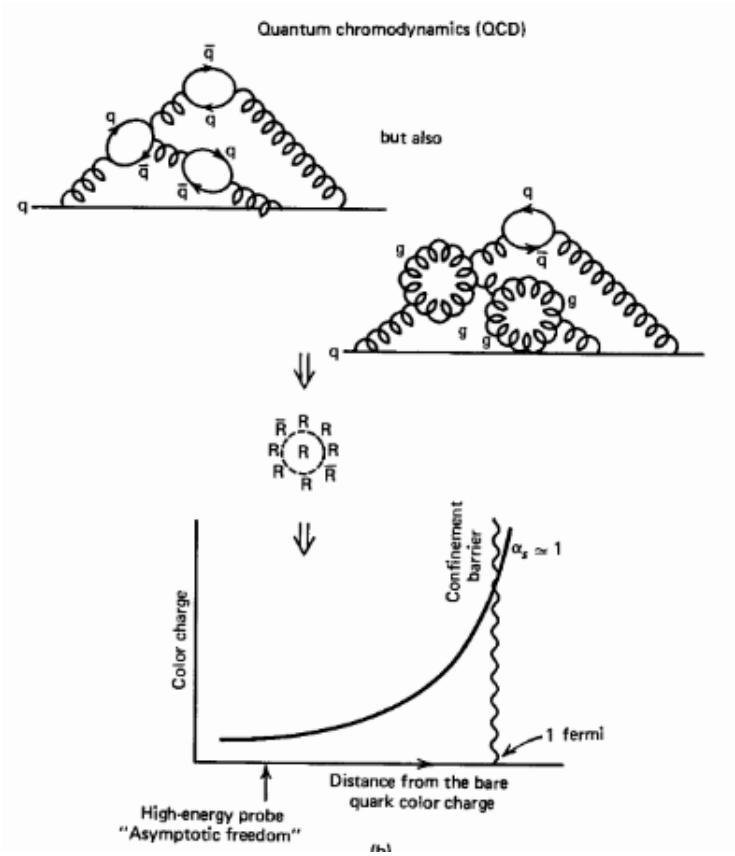

Figure 1.3: Screening of the color charge in QCD [9].

important consequence: the existence of jets. Suppose one has a baryon, such as the proton depicted in figure 1.4, and tries to separate one of the quarks from the other two. Due to asymptotic freedom the quarks are essentially free within the baryon. As one tries the separate them, i.e., increase the distance between the quarks, the interaction between them grows stronger, since color confinement does not allow the quarks to exist isolated. As the strong force tries to approximate the quarks back, it becomes, at some point, energetically more favorable to create a quark-antiquark pair from the vacuum than to separate the quarks from the baryon any further [9].

In summary, trying to break-up the hadron resulted in two new hadrons being created with no free quarks being obtained, as shown in figure 1.4. Thus, trying to observe isolated quarks (or gluons) results in several quark-

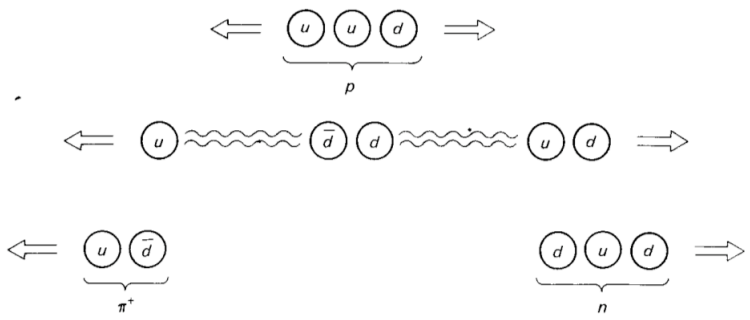

Figure 1.4: Possible scenario of color confinement of quarks. [3]

antiquark pairs being created. These join together in a myriad combinations resulting in the production of jets, through a process referred to as hadronization [3].

Basically, a jet is a collimated stream of colorless particles: mesons, baryons, leptons, photons. It emerges along the expected flight path of the primordial quark or gluon (since gluons carry color themselves they hadronize into jets just like quarks). Jets are, thus, the materialization or signatures of quarks and gluons [10].

The biggest challenge when it comes to jets is that hadronization is a non-perturbative process, since α_s increases for long distances. This means that it is not simple to understand jets on a theoretical point of view, since calculations are usually impossible. For example, one cannot calculate the content of photons in a particular jet. In fact, hadronization is explained mostly through models obtained from approximate treatments to QCD. Nonetheless, methods have been developed that allow the association of the visible jet to the non-visible quark or gluon that originated it. This will be developed in the following sections [8, 11].

1.2.2 Jet Production

As mentioned in the previous chapter, trying to obtain isolated partons originates jets. Jets were observed for the first time in the late 70's by the JADE experiment at PETRA. At PETRA, electron-positron collisions took place. Some of those collisions originated a quark-antiquark pair: $e^+ + e^- \rightarrow q + \bar{q}$. The pair eventually hadronized and the resulting particles were observed as two back-to-back jets by the JADE detector. Sometimes, three-

jet events were observed as well. The third jet was interpreted as the result of the hadronization of a gluon radiated by one of the produced quarks. Thus, the three jet configuration was regarded as the most direct evidence of the existence of gluons and of their hadronization into jets [10, 3].

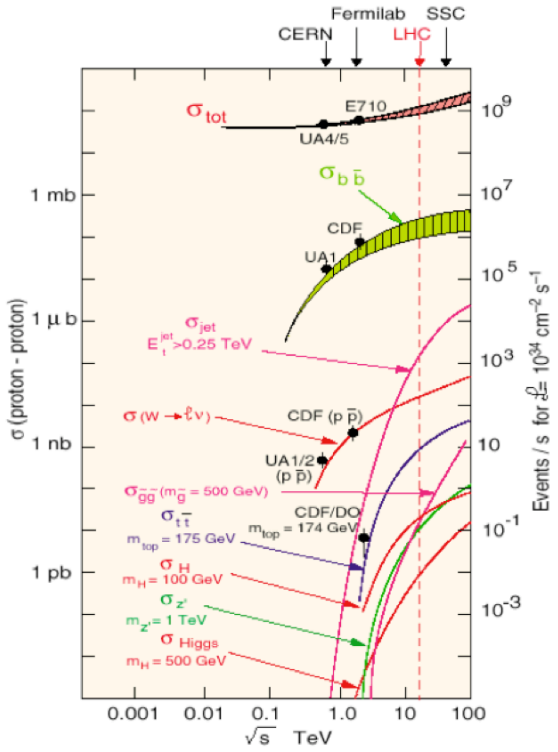

Figure 1.5: Cross sections for several processes as a function of $\sqrt{s}$ from pp collisions [12].

Jets are also commonly produced in hadron-hadron colliders. This is understandable, since this type of colliders aims at breaking-up the hadrons, and is shown in figure 1.5. It presents the cross sections (σ) for several processes, occuring through proton-proton (pp) collisions, as a function of the center of mass energy ($\sqrt{s}$) and at a luminosity ($\mathcal{L}$) of $10^{34}\text{cm}^{-2}\text{s}^{-1}$ [12]. Roughly, σ gives the probability at which a certain process occurs. This means that the higher the cross section of a certain process, the more likely it is that this process will come as a result of the collision. Thus, the rate ($\frac{dN}{dt}$) at which a certain process occurs depends on its cross section. In

particular, one has $\frac{dN}{dt} = \sigma \times \mathcal{L}$. Basically, $\mathcal{L}$ is the luminosity and measures the density of particles in the colliding beams. It can be integrated over time, to obtain the integrated luminosity - $L = \int \mathcal{L} dt$ - in which case, the number of events is given by $N = \sigma \times L$ [13].

Taking this into account and analyzing figure 1.5, one can see that for pp collisions and hadron-hadron collisions in general, jet production is by far the process with the largest cross section, meaning that jet events are, indeed, very common in hadron colliders. This evaluation can be done on a more quantitative level, by considering the LHC, a hadron collider whose working conditions are indicated by the dotted line in figure 1.5. The total cross section for pp colisions at the LHC is $\sigma_{total}^{LHC} \approx 100$mb [14]; for dijet production at the LHC one has $\sigma_{dijet}^{LHC} \approx 0.4$mb [15]; and the production of a 100GeV Higgs boson through gluon fusion has a cross section of $\sigma_{Higgs}^{LHC} \approx$ 44pb [16].

It is clear now that understanding hadronic collisions is necessary to do studies on jets. Those studies can go from building MonteCarlo programs that simulate jet production, allowing some predictions to be made, to interpreting experimental results on particle detectors. To analyze the main aspects involving hadronic interactions and the production of jets, let us consider an event where two jets are produced. The production process is defined by $p + p \rightarrow jet + jet + X$, where p are the colliding protons and X represents everything else produced in the collision. A schematic diagram of this scattering process is displayed in figure 1.6 [17].

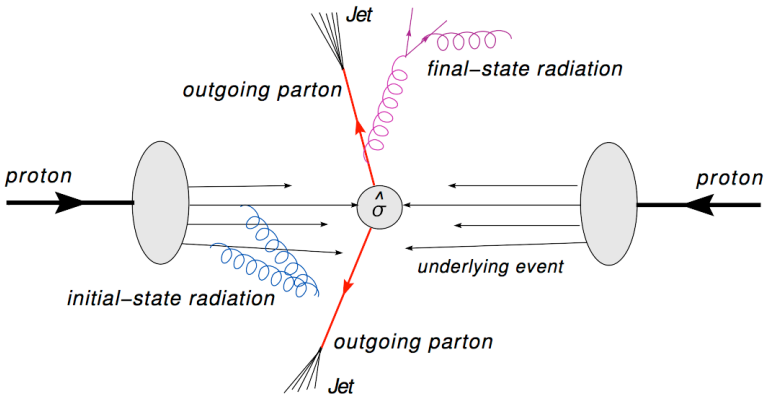

Figure 1.6: Schematics of a scattering process between two hadrons [13].

The scattering process in figure 1.6 can be divided into the hard scattering part and the soft scattering part. QCD is the underlying theory that describes both parts. It is, however, more easily applied to the hard scattering part of the process than to the soft part, where non-perturbative effects dominate. Thus, separating the full scattering process into several distinct steps is essential to understand it. These steps are presented in detail next [17].

The first step is the hard collision of two incoming partons, which can be represented by the diagram in figure 1.7. The two partons, one in each colliding hadron, are scattered at wide angles after passing very close to each other and, as a result, outgoing partons are produced. This is actually the process of particular interest, since the outgoing partons will eventually hadronize and be observed as jets of particles. This subject will be further developed in the section 1.2.3.

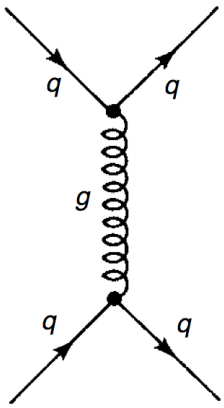

Figure 1.7: Feynman diagram for the scattering of two quarks [3].

The relative probability of finding the scattering partons at this step is provided by the parton distribution functions (pdfs). Roughly, the pdf of a certain parton reveals "how much" of that parton exists in the colliding hadron at a certain energy scale, defining the parton uniquely [17].

The other elements visible in figure 1.6 (X), besides the partons/jets produced by hard scattering, are the result of several soft processes, which will be described next.

The two partons that undergo hard scattering can, before scattering, emit radiation, producing showers that constitute the initial state radiation

(ISR). The same process can occur with the outgoing partons from the hard scattering, before they hadronize, creating final state radiation (FSR) [13].

As for the partons remaining from the original hadrons, i.e. the ones that did not suffer hard scattering, they will interact softly with each other, scattering at small angles and generating the underlying event (UE). The UE, together with the ISR, produce the so-called beam remnants, which can suffer soft multiple interactions between them as well.

Finally, it is also important to mention minimum bias events. In a scattering process between two hadrons, often the hard scattering part does not occur, which means that all partons interact softly. Thus, in a high-luminosity regime, where the number of interacting hadrons per unit of time is high, if a scattering process between two hadrons occurs with the hard part, it will be accompanied by additional and uncorrelated soft processes from the interaction of the other hadrons. The products from these additional soft interactions will pile-up with the products from main scattering processes [13].

1.2.3 Jet Reconstruction

In the previous section, the subject of jet production in hadron-colliders was addressed. In summary, when two protons collide, the process of interest is the hard scattering between two partons, that produces high momentum outgoing partons. These partons eventually hadronize into jets of particles. Those jets are observed in particle detectors as multi-particle signals. This is depicted in figure 1.8, if one reads it in the upward direction, following the "jet production" arrow.

The goal at this point is to interpret the observed jet signals in terms of the underlying partons, i.e., to reconstruct the jets. Jet reconstruction is, thus, equivalent to reading figure 1.8 in the downward direction. The basic idea behind it is that one should be able to perform jet reconstruction on different objects - partons resulting from the hard scattering ("parton jet"), particles resulting from the hadronization of those partons ("particle jet") and detector signals resulting from those particles ("calorimeter[4] jet") - and

[4]The expression "calorimeter jet" is employed because calorimeter signals are the most commonly used signals for jet reconstruction; nonetheless, other detector signals can be used, such as tracks.

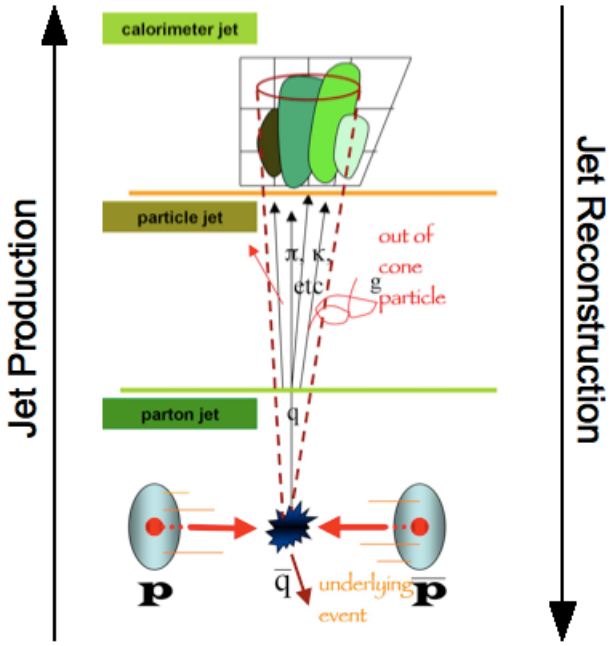

Figure 1.8: Representation of the stages of jet production / jet reconstruction.

obtain the same jet without ambiguities or biases [18, 17]. The main aspects concerning jet reconstruction are described in the following sections.

1.2.3.1 Jet Identification

The first step in jet reconstruction is to identify the jet by means of a jet algorithm. A jet algorithm is, basically, a set of rules that defines the jet [18].

First, the algorithm identifies and clusters the objects that belong to the jet, whether those objects are real and obtained experimentally or generated and simulated with MonteCarlo. They can be detector signals, particles resulting from the hadronization or partons resulting from the hard scattering.

Then, the jet algorithm provides a recombination scheme that determines the properties of the jet as a function of the properties of the objects that make it. Usually it is a four-momentum $(E, \overrightarrow{p})$. The jet algorithm works in such a way that the properties of the jets can be, ultimately, related to the properties of the partons resulting from the hard scattering. In other words, a jet algorithm allows us to see the fingerprints of the partons in the

observed final states [19].

An ideal jet algorithm should possess certain attributes, both theoretical and experimental. As elucidated in figure 1.8, where the dotted cone represents the jet algorithm, the attributes are meant to minimize the difference between reconstructed "calorimeter jets", "particle jets" and "parton jets". In other words, and taking into account what was said in the previous section, the attributes of an ideal jet algorithm ensure that the same jet is always identified, regardless of which object the algorithm is applied to [19].

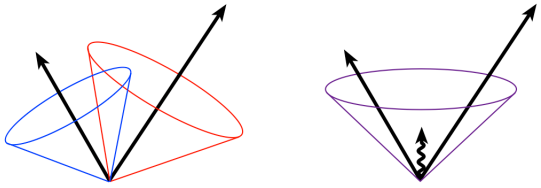

Figure 1.9: Representation of infrared sensitivity of a jet algorithm [19].

On the theoretical point of view, a jet algorithm should have the following attributes [19]:

- *Infrared safety* - This basically means that a jet algorithm should be insensitive to soft radiation. As shown in figure 1.9, if the algorithm is infrared safe, the two signals (represented by arrows in the right) would be reconstructed as two separate jets (represented by the cones). In an infrared sensitive algorithm, the two jets could be merged into one jet (cone on the right) due to the presence of soft radiation between them (wavy arrow).

- *Collinear safety* - If a particular signal is split into two equivalent and collinear signals, the reconstructed jet should remain unchanged. This is depicted in figure 1.10. Basically, if the algorithm is collinear safe, the jet (cone) would not change due to the splitting of the signal (long arrow on the left) into two (on the right).

- *Invariance under boosts* - This attribute ensures that the same solution is found independent of boosts in the longitudinal direction.

From the experimental standpoint, the attributes should minimize the effect of detector response, noise, pile-up, among others, on the jet identification process [19]:

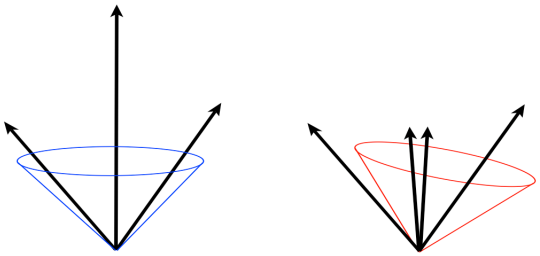

Figure 1.10: Representation of collinear sensitivity of a jet algorithm [19].

- *Detector independence* - The algorithm should perform independent from the detectors characteristics, such as noise, response, segmentation or resolution.
- *Stability* - The jet algorithm should show stability with luminosity, meaning that the size of the jet should not be affected if other parton hard scatterings occur at high luminosities.
- *Efficency* - A jet algorithm should be efficient and easy to implement, identifying all physically interesting jets with minimum computing time.
- *Ease of calibration* - A jet algorithm should present no obstacles to the calibration of the properties of the reconstructed jet; this subject will be developed in the following section.
- *Fully specified* - The jet identification process must be fully specified, which includes clear definition of all the procedures, namely clustering and determination of the kinematic variables.

Several jet algorithms exist and part of the challenge is determining which ones are optimal for each specific physics analysis. Historically, cone algorithms have been the choice for hadron-hadron colliders. These algorithms select objects close to each other and group them to form a cone-shaped jet in the (η, ϕ)-space (a two-dimensional space used commonly in hadron-hadron detectors). Though simple, fast and of easy implementation, cone algorithms presents some well known problems, such as the fact that the reconstructed jets can overlap and share energy and that they are not infrared safe. Thus, a second class of jet algorithms has been developed and

proved more well behaved: the k_T algorithms. With these algorithms, the combination of objects does not depend solely on the distance between them but also on their kinematic properties [19].

1.2.3.2 Jet Energy Measurement

As shown in figure 1.8 and mentioned in the previous section, jets have to be reconstructed from the signals their particles leave in the particle detectors. Ultimately, the goal of jet reconstruction is to determine the properties of the original parton. However, identifying the jet by running a jet algorithm on detector signals is not enough to achieve this goal and calibration of the jet energy is fundamental to properly reconstruct the jet. The need for calibration of the jet energy is explained next [20].

Although other detectors, such as tracking devices, can be used, calorimeters are, usually, the most relevant systems for jet reconstruction, hence the expression "calorimeter jet". Calorimeters have the role of determining the energy of the particles, which means jets are usually reconstructed from energy depositions left in the calorimeters' cells. Thus, understanding the way particles interact with calorimeters is necessary to understand the need for a calibration step in the process of jet reconstruction [17].

The basic mechanism that allows calorimeters to determine the energy of the particles is shower formation. Almost every particle[5] that crosses a calorimeter, or any detection device, starts interacting with the nuclei of the materials that constitute it. As a result, secondary particles are produced with less energy than the original particles. Those secondary particles will also interact with the dense matter that forms the calorimeters and generate other less energetic particles. The result is a cascade of particles that develops and grows until the only particles remaining are low energy ones that are stopped by the calorimeter and fully absorbed [21]. So, in summary, the energy of a particle is deposited gradually in the calorimeters, throughout the shower development. The calorimeters collect the energy and respond with a signal proportional to the amount of energy deposited.

Showers can be classified in two types. Electromagnetic showers are usually initiated by photons or electrons/positrons and develop primarily

[5]The exceptions are muons and neutrinos.

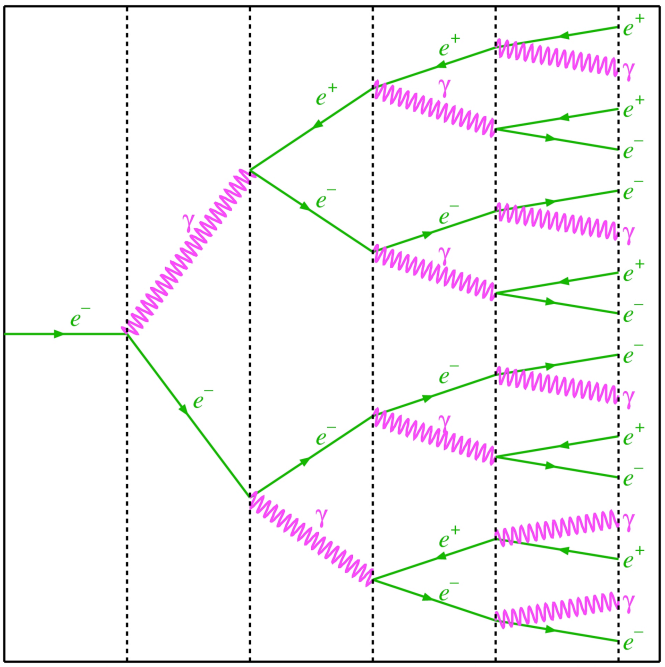

Figure 1.11: Simplified example of the development of an electromagnetic shower initiated by an electron.

through electromagnetic processes such as Bremsstrahlung or pair production (figure 1.11). Hadronic showers are, as the name indicates, initiated by hadrons, such as protons and neutrons. They develop mainly due to strong interactions between hadrons and the nuclei of the materials that compose the calorimeters [21].

The name "hadronic" might actually be misleading because hadronic showers also have an electromagnetic component, since some hadrons are charged particles. For that reason, and also because hadrons, unlike electrons and photons, are not elementary particles, hadronic showers are usually more complex and difficult to measure, treat, analyze or simulate than electromagnetic showers [22].

Figure 1.12 illustrates an important fact about hadronic showers, that is not observed in electromagnetic showers, called non-compensation. Essentially, calorimeters do not respond the same way to electromagnetic and

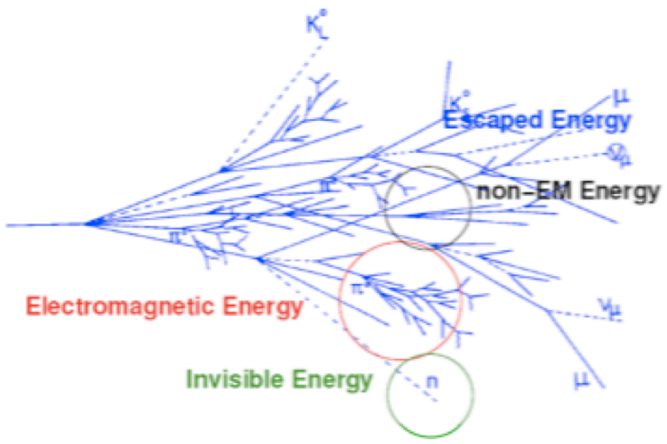

Figure 1.12: Example of the development of a hadronic shower [21].

hadronic showers[6]. The response of a calorimeter evaluates how much of the total energy of the particle is indeed collected by the calorimeter and one usually has $e/h > 1$, where e is the response of the calorimeter to the electromagnetic component of a shower and h is the response to the hadronic component of a shower. Moreover, while e is approximately linear with the energy of the interacting particles, h is not. The reason for this has to do with the distinct way the two types of showers develop, as will be shown next [22].

To begin with, from the first time the primary hadron interacts with the nuclei of the medium that forms the calorimeter, a significant fraction of the energy is removed from further hadronic interaction. For example, particles such as the π_0 marked in red in figure 1.12, decay into photons that then generate high energy electromagnetic cascades. This fraction of the energy ($\approx 50\%$), because it is of electromagnetic nature, is actually well determined by calorimeters [4, 22].

However, as charged secondary particles (such as $\pi^{\pm}$, p, ...) interact with nuclei, they can either ionize ("non-EM energy" shown in black in the figure), or generate nuclei in excited states, fragments of nuclei and particles like muons and neutrinos. The energy to excite a nuclei or break it

[6] In reality, there are calorimeters that do not exhibit this behavior, but for the calorimeters considered in this thesis this is a true statement.

up generates little or no detectable signal and neutrinos and muons can cross calorimeters undetected. Consequently, these phenomena originate energy that is not collected by the calorimeters. In the end, a significant fraction of the hadronic energy - $20\% - 30\%$ depending on the calorimeter and the energy of the incident particle - is "invisible" or has "escaped" (blue and green in figure 1.12) [4, 22].

Taking this into account and since jets are of hadronic nature, it is clear that non-compensation can greatly influence the reconstruction of calorimeter jets. In fact, other detector effects such as noise, dead material and detector signal efficiencies, or even physics effects, like pile-up, underlying event and jet identification algorithm efficiencies, will affect the reconstruction as well. Moreover, the goal of jet reconstruction is to obtain jets at parton level, since it is the originating parton that constitutes the reference. However, the energy of the parton is not influenced by the mentioned detector and physics effects. Thus, one expects the energy reconstructed for a calorimeter jet to be different (usually lower) than the real energy of that jet, i.e., the energy of that jet at parton level. Therefore, once calorimeter jets are identified, calibration of their energies is a fundamental step to their reconstruction [23].

The jet energy scale evaluates the difference between the energy of the reconstructed jets and the real energy of those jets. So in other words, the goal of calibration is to obtain a uniform and stable jet energy scale, as a function of the energy of the jets and the positions where they were identified in the detectors, minimizing the difference between the reconstructed and real energies [23].

Several calibration schemes exist but the basic concept behind the most commonly used consists of applying calibration weights to detector signals according to the type of signals, i.e., hadronic-like or electromagnetic-like [23]. This subject will be further discussed in another chapter.

Chapter 2

The ATLAS Experiment

2.1 The Large Hadron Collider

Located in the French-Swiss border, the European Organization for Nuclear Research [24] (CERN) is a scientific research facility created in 1954. Having 20 European Member States, employing around 2500 people (physicists, engineers, technicians, designers) and receiving over 8000 visiting scientists, CERN is, nowadays, the world's largest particle physics center.

To achieve its main goal of providing *"...for collaboration among European States in nuclear research of a pure scientific and fundamental character..."*, CERN makes use of instruments like particle accelerators, which boost beams of particles to high energies before they are made to collide, and detectors, which are used to observe and record the results of these collisions. In particular, CERN holds the accelerator complex depicted in figure 2.1. It is a chain of machines, where particle beams are injected from one to the next and their energies are increased successively.

The latest addition to the complex is called the Large Hadron Collider [25, 26] (LHC). The LHC will accelerate and collide hadrons, protons and lead ions (which will not be addressed in this thesis), with unprecedented working conditions, that will change the world of particle physics. Not only it will allow the rediscovery of the Standard Model, permitting high precision tests of QCD, electroweak interactions and flavor physics, but also, hopefully, enable the search for new physics phenomena: Higgs boson, Supersymmetry (SUSY), dark energy and dark matter...

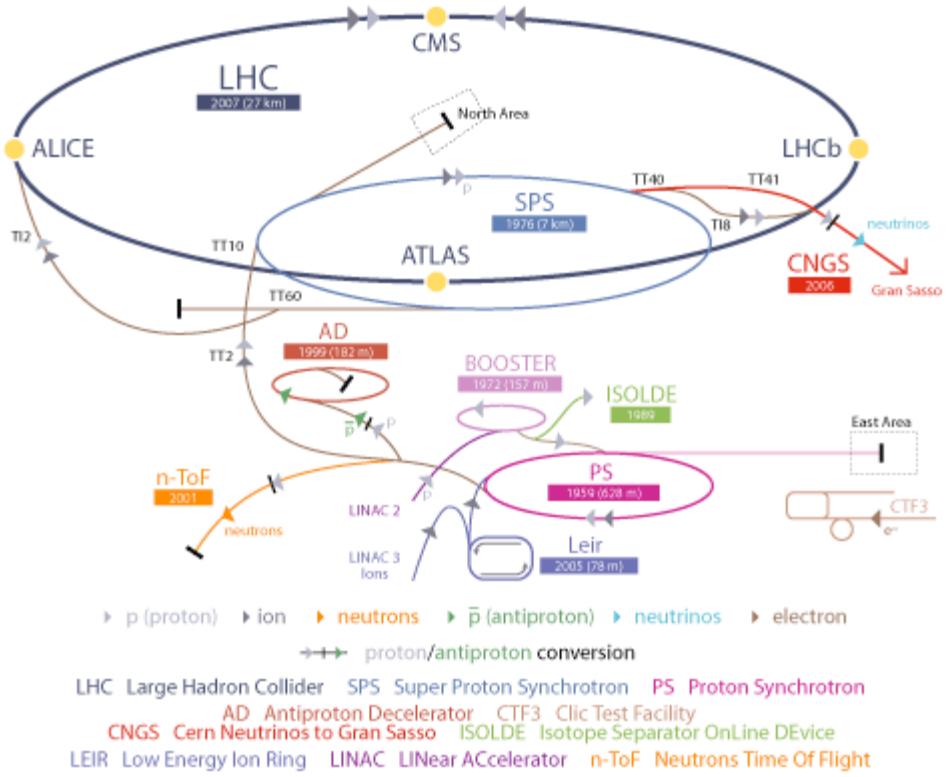

Figure 2.1: Schematics of the accelerator complex at CERN.

On September 10^{th} 2008 proton beams circulated successfully in the LHC for the first time. On September 19^{th}, however, a helium leak caused damage to the accelerator and the operations were stopped for repair. At this point, it is scheduled that the LHC will be again ready for beam injection by mid-November 2009 [27].

The LHC [28, 26] is installed in the Large Electron-Positron (LEP, a previous collider at CERN) tunnel, 50-175 meters underground, spanning the boarder between Switzerland and France. It consists of two rings (beam pipes) with a circumference of 26660m, where the beams will circulate in opposite directions. To avoid collision between the beam and gas molecules, the beam pipes are kept at a ultrahigh vacuum reaching 10^{-13}atm. The rings cross at four points - the interaction points - where the hadrons are made to collide and four detectors are placed. Figure 2.2 shows a diagram of the underground placement of the LHC and the four detectors at the interaction points.

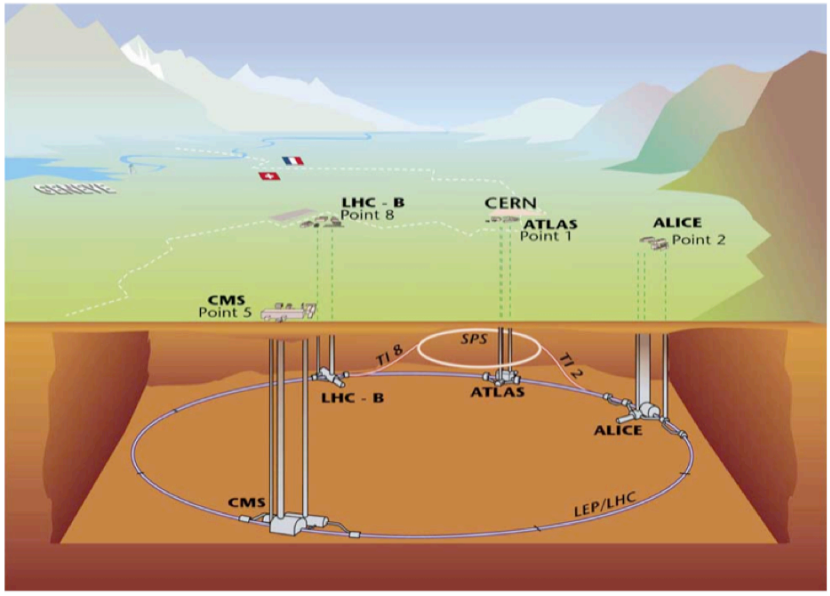

Figure 2.2: Diagram of the LHC and its four associated detectors.

A total of 1232 dipole magnets (figure 2.3) create a 8.33T magnetic field that bends the beams so they follow circular paths inside the pipes and 392 quadrupole magnets are used to focus the beams, i.e., bring the protons closer together. These are superconducting magnets that operate at 1.9K. To keep this low temperature, the cryogenic system of the LHC uses superfluid helium. Eight superconducting radiofrequency cavities per beam, operating at 4.5K, will accelerate the beams and keep them at constant energy.

The protons are injected in the LHC with an energy of 450GeV. Inside the LHC they will achieve 99.999% of the speed of light ($\gamma = 7461$), circling the LHC 11245 times per second. The beams will have a maximum energy of 7TeV. This means the center of mass energy for pp collisions in the LHC is $\sqrt{s} = 14$TeV.

The proton beams are made of 2808 cylinder-like bunches of protons 7.5m apart. This means a new bunch will reach an interaction point every 25ns or, in other words, 40 million bunch crossings (what one calls "events") will occur per second at an interaction point. The length and width of the bunches varies along the beam pipes: they are 7.55cm long and 1mm wide when far from the interaction points but get squeezed to 16μm$\times 16\mu$m near the interaction points in order increase the probabilities of collisions.

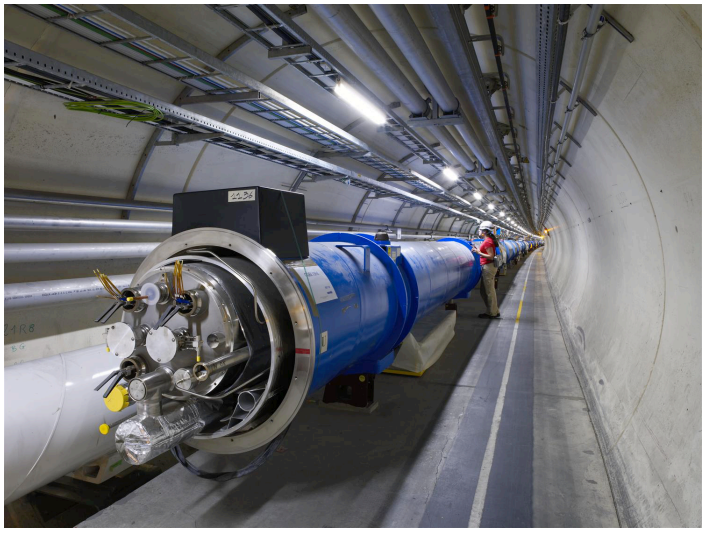

Figure 2.3: Picture of a LHC dipole in the tunnel.

Each bunch will be filled with 1.15×10^{11} protons. Near the interaction points, the LHC is designed to reach a peak luminosity of $\mathcal{L} = 10^{34}\text{cm}^{-2}\text{s}^{-1}$, which has a lifetime of about 15hours. With these conditions pile-up will occur in the LHC, as up to 23 *pp* collisions can occur per bunch crossing. Also, the LHC is expected to operate about 10^7s per year, which means an integrated luminosity of $L = \int \mathcal{L}dt = 100\text{fb}^{-1}$ can be reached per year.

One final note to mention that this section describes the nominal conditions of the LHC, which are not expected at startup, especially after the incident on September 19^{th} 2008. At the moment, the LHC is expected to begin operating in mid-November 2009, with $\sqrt{s} = 7\text{TeV}$ and a luminosity ranging from $\mathcal{L} = 5 \times 10^{31}\text{cm}^{-2}\text{s}^{-1}$ to $\mathcal{L} = 2 \times 10^{32}\text{cm}^{-2}\text{s}^{-1}$. An average of 1.8 interactions per bunch crossing will occur in these conditions and about 200pb^{-1} are expected in the first year.

2.2 A Toroidal LHC Apparatus

As mentioned in the previous section, the LHC beam pipes intersect at four points (figure 2.2) where collision between the two hadron beams occur. At each of those points, a detector is placed to observe the results of the collisions. The four detectors at the LHC are ATLAS [29] (A Toroidal LHC ApparatuS), CMS [30] (Compact Muon Solenoid), ALICE [31] (A Large

Ion Collider Experiment) and LHCb [32] (Large Hadron Collider beauty). ALICE and LHCb are specialized detectors whereas ATLAS and CMS are general-purpose detectors. Only the ATLAS detector will be addressed in this thesis.

2.2.1 The Detector

Located at Point 1 of the LHC, in Meyrin, Switzerland, ATLAS [33] is a general-purpose detector, designed to exploit the full potential of the LHC by analyzing the myriad of particles produced by the pp collisions. Being 46m long, 25m wide, 25m high and weighing 7000 tonnes, the cylindrical detector is the largest volume collider detector ever built. The ATLAS Collaboration consist of more than 2500 members (including 700 students) from 169 institutes in 37 countries.

Figure 2.4 shows the layout of the detector and its coordinate system. It is essentially a cylindrical coordinate system, with the origin placed at the interaction point. The beam direction defines the z-axis. The plane defined by the x and y axis is called the transverse plane. Quantities such as transverse momentum (p_t) and transverse energy (E_t) are often used. The positive x-axis points to the center of the LHC ring and the positive y-axis points upwards. The azimuthal ϕ angle is measured around the beam axis, it ranges $[-\pi, \pi]$ and $\phi = 0$ is on the positive x-axis. The polar angle θ is measured around the x-axis and $\theta = 0$ is on the positive z-axis.

In ATLAS the variable pseudorapidity is very commonly used. Defined as

$$\eta = -\ln \tan(\frac{\theta}{2})$$

it ranges approximately $[-5, 5]$. Table 2.1 presents the values of η for several θ angles. Having this new coordinate, one usually defines a new coordinate-space using (η, ϕ). A radius in this space is

$$R = \sqrt{\eta^2 + \phi^2}$$

and

$$\Delta R = \sqrt{(\Delta\eta)^2 + (\Delta\phi)^2}$$

gives a distance. η is also particularly useful to define the quantities in the transverse plane:

$$p = p_t \times \cosh \eta$$

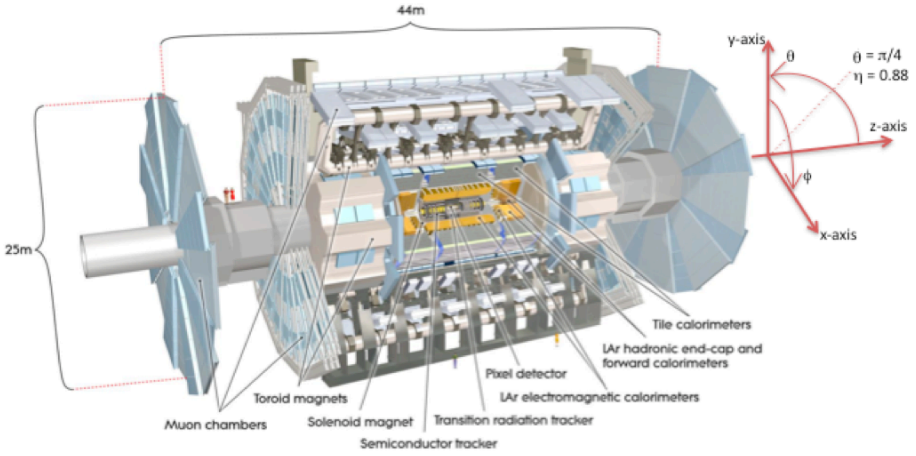

Figure 2.4: Overall layout of ATLAS, with its main components labelled and the indication of the coordinate system.

and

$$E = E_t \times \cosh \eta$$

Finally, it is also usual to divide the detector according to the η position. For example, when one refers the central or barrel region of the detector that means $|\eta|$ close to zero, whereas the forward regions have large $|\eta|$.

To support the LHC's physics' program [33], a number of requirements have been set for ATLAS:

- Because of the experimental conditions at the LHC, ATLAS is required to have fast, radiation-hard electronics and sensor elements.
- High detector granularity is needed to handle the high flux of particles and reduce the influence of overlapping events.
- Large η acceptance and almost full ϕ coverage is required.
- Good charged particle momentum resolution and reconstruction efficiency are essential.
- Very good electromagnetic calorimetry, for electron and photon identification and measurements.

$\eta = -\ln\tan(\frac{\theta}{2})$			
θ *(degrees)*	η	θ *(degrees)*	η
0	$+\infty$	180	$-\infty$
5	3.13	175	-3.13
10	2.44	170	-2.44
20	1.74	160	-1.74
30	1.31	150	-1.31
45	0.88	135	-0.88
60	0.55	120	-0.55
80	0.18	100	-0.18
90	0	90	0

Table 2.1: Some representative values of η and the corresponding polar angle.

- Full hadronic calorimetry, needed for accurate jet and missing transverse energy measurements.
- Good muon identification and momentum resolution over a wide range of momentum and the ability to determine unambiguously the charge of high p_t muons are fundamental requirements.
- Highly efficient triggering on low p_t objects with enough background rejection is crucial.

As for the design of the detector itself (schematized in figure 2.4), it was constrained by several factors, such as the high interaction rates at the LHC, the elevated radiation doses, the multiplicity of particles produced and their energies and the requirements for precision measurements. In the end, ATLAS is a detector formed by several subdetectors and a magnet system. The performance goals for each subdetector are summarized in table 2.2. Those subdetectors are the inner detector, the electromagnetic and hadronic calorimeters and the muon spectrometer (the first and the last are tracking devices). In the barrel region of ATLAS, the subdetectors are placed in cylindrical layers around the beam pipe. This is clearly shown in figure 2.5. On each side of the barrel, two endcaps of the subdetectors are placed, in order to cover more forward regions in pseudorapidity. A more

detailed description of the ATLAS detector systems is presented in the next sections.

ATLAS Performance		
Subdetector	*Required Resolution*	η *Coverage*
inner detector	$\frac{\sigma_{p_t}}{p_t} = 0.05\% p_t \oplus 1\%$	$\lvert\eta\rvert < 2.5$
EM calorimeter	$\frac{\sigma_E}{E} = 10\%/\sqrt{E} \oplus 0.7\%$	$\lvert\eta\rvert < 3.2$
hadronic calorimeter	$\frac{\sigma_E}{E} = 50\%/\sqrt{E} \oplus 3\%$	$\lvert\eta\rvert < 3.2$
forward calorimeter	$\frac{\sigma_E}{E} = 100\%/\sqrt{E} \oplus 10\%$	$3.1 < \lvert\eta\rvert < 4.9$
muon spectrometer	$\frac{\sigma_{p_t}}{p_t} = 10\% p_t$ (at $p_t = 10$TeV)	$\lvert\eta\rvert < 2.7$

Table 2.2: General performance goals of the ATLAS detector (p_t and E in GeV).

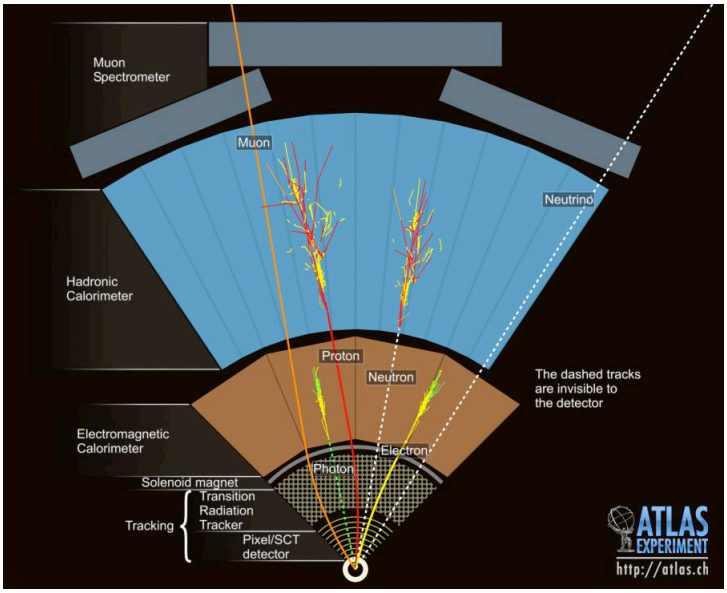

Figure 2.5: Diagram of a transversal cut of the ATLAS barrel, showing the layers of subdetectors and the way particles interact with them.

2.2.1.1 The Magnet System

The magnet system in ATLAS [33] creates a magnetic field over a volume of approximately 12000m^3. This is essential to deflect the paths of charged particles, allowing the determination of their momenta. The choice for ATLAS was a unique system of four large superconducting magnets (figure 2.6),

one solenoid and three toroids (one barrel and two endcaps), that provide a coverage of $|\eta| < 2.7$.

(a) Solenoid magnet (on the left).

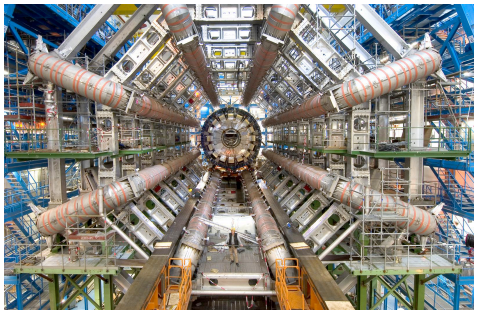

(b) Toroid barrel magnets.

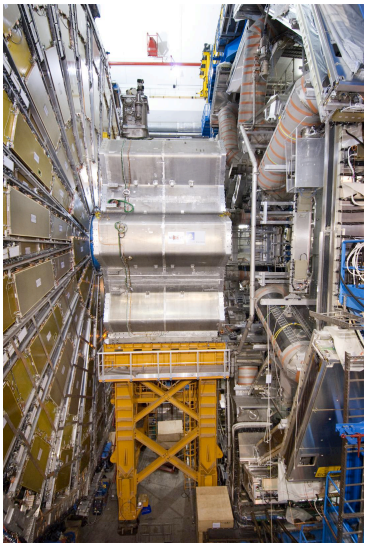

(c) Toroid endcap magnet.

Figure 2.6: Pictures of the several components of the ATLAS magnet system.

The solenoid magnet (figure 2.6(a)) surrounds the inner part of ATLAS, extending over a length of 5.3m, with a diameter of 2.5m. It provides a 2T magnetic field for the inner detector, parallel to the beam axis. The magnetic field is nearly uniform and strong enough to bend high energy particles. This, however, prevents measurements of the momenta of low energy particles. Since this magnet sits between the inner detector and the electromagnetic calorimeter, as shown in figure 2.5, the biggest challenge was to reduce the thickness of the material as much as possible, allowing

particles not to lose much energy before reaching the calorimeter. The result was a 45mm thick magnet, the equivalent of 0.66 radiation lengths[1].

Three large toroid magnets (one barrel and two endcaps), each consisting of eight coils, are assembled with azimuthal symmetry around the detector. The barrel toroid has a length of 25.3m, an inner radius of 9.4m, an outer radius of 20.1m and produces an average magnetic field of 0.5T. The endcap toroids are inserted at each end of the barrel toroid and are lined up with the solenoid magnet, producing a 1T magnetic field (in average). The toroids' magnetic field serves the muon spectrometer providing bending power to the muons and, contrary to the solenoid magnetic field, it is not uniform.

2.2.1.2 The Inner Detector

The Inner Detector [33] (ID) constitutes the first layer of the ATLAS detector (figure 2.5) and has a coverage of $|\eta| < 2.5$. It is essentially a tracking device, i.e., it identifies and reconstructs the trajectories of charged particles. Its layout is presented in figure 2.7.

As mentioned before, bunches of protons will cross the interaction point every 25ns, meaning that approximately 1000 particles will originate from collisions every 25ns. This environment creates a high track density in ATLAS. However, the ID has the capacity to achieve robust pattern recognition, excellent momentum resolution and precision vertex measurements for charged particles.

The ID is embedded in a 2T magnetic field created by the solenoid magnet that surrounds it, bending the path of charged particles and allowing the determination of their momenta. It consists of three independent, but complementary, subdetectors: the Pixel Tracker, the Semiconductor Tracker (SCT) and the Transition Radiation Tracker (TRT).

Close to the interaction point, the silicon pixel layers from the pixel tracker and the silicon microstrip layers from the SCT make discrete measurements to achieve high resolution pattern recognition. The SCT also allows impact parameter and primary vertex measurements. The secondary vertex measurements are achieved by the pixel tracker with high precision.

[1] An electron loses $1/e$ of its energy by Bremsstrahlung after one radiation length. A radiation length is also 7/9 of the mean free path for pair production by a high energy photon.

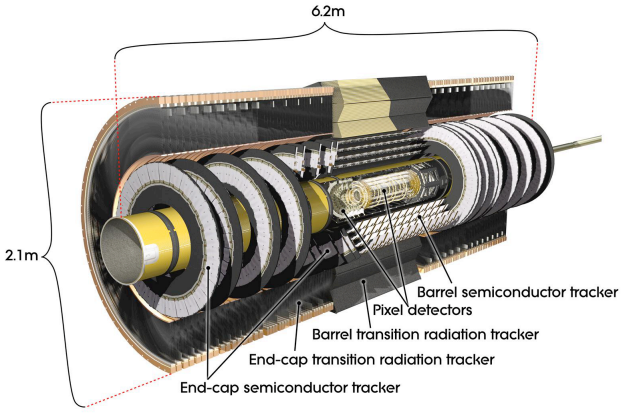

Figure 2.7: Cut-away view of the ATLAS inner detector, with its main components labelled.

At larger radii, layers of gaseous straw tubes form the TRT provide continuous measurements. The straw hits provide less precise pattern recognition than the silicon hits but contribute significantly to high resolution momentum measurement. The TRT is also particularly important as it has the ability to identify electrons by the detection of transition-radiation photons in the gaseous straw tubes.

2.2.1.3 The Calorimeters

The Electromagnetic Calorimeter The electromagnetic (EM) calorimeters [33] in ATLAS can be divided in two types: EM barrel plus two endcaps (EMEC). Both the EM barrel and EMEC use the same liquid argon (LAr) technology and are, therefore, often referred to as the LAr calorimeters. They are presented in figure 2.8.

The EM barrel surrounds the solenoid magnet and has a coverage of $|\eta| < 1.475$. It actually consists of two identical half-barrels, separated by a 4mm gap at $z = 0$ (transverse plane). Each half-barrel extends over a length of 3.2m and has an inner and outer diameters of 2.8m and 4m, respectively. Depending on the η coordinate, the EM barrel can have from 22 to 33 radiation lengths X_0. The EM barrel calorimeter is greatly segmented in η and ϕ forming high granularity cells of 0.025×0.025 in $\Delta\eta \times \Delta\phi$.

The two EM endcaps are placed on each side of the barrel to achieve larger coverage in pseudorapidity: $1.375 < |\eta| < 3.2$. Each endcap can

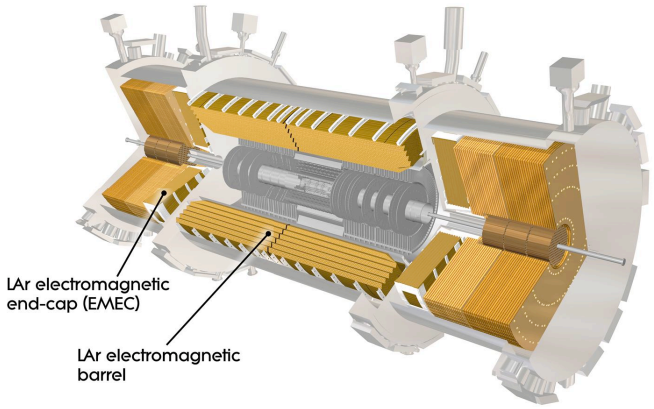

Figure 2.8: The electromagnetic calorimeters in ATLAS.

actually be divided into two wheels, each wheel covering a different region in pseudorapidity. The EMEC's are 63cm thick, with external and internal radii of 2098mm and 330mm, respectively. The total active thickness of an EMEC is around 24 X_0, but can reach 38 X_0 for larger pseudorapidities. The EMEC are also segmented but with coarser granularity in $\Delta\phi$ than the EM barrel.

The ATLAS EM calorimeters are sampling calorimeters, since they are made of layers of two different materials: a passive material that has the role of absorbing the energy of the particles and an active material that is in charge of measuring that energy. The passive absorber is lead whereas the active material is liquid argon. The layers are placed with an accordion geometry (figure 2.9) that provides a full ϕ coverage with no cracks or gaps and fast extraction of the signal.

The Hadronic Calorimeter Similar to what was seen for the electromagnetic calorimeter the ATLAS hadronic calorimeter [33] also has two components: the hadronic barrel and the hadronic endcaps (HEC). However, the technology involved in each one is very different. The HEC is a LAr calorimeter similar to the electromagnetic calorimeters presented before. The hadronic barrel is a tile calorimeter and is referred to as TileCal. Figure 2.10 presents the hadronic calorimeters.

Figure 2.9: The accordion geometry of the LAr calorimeters.

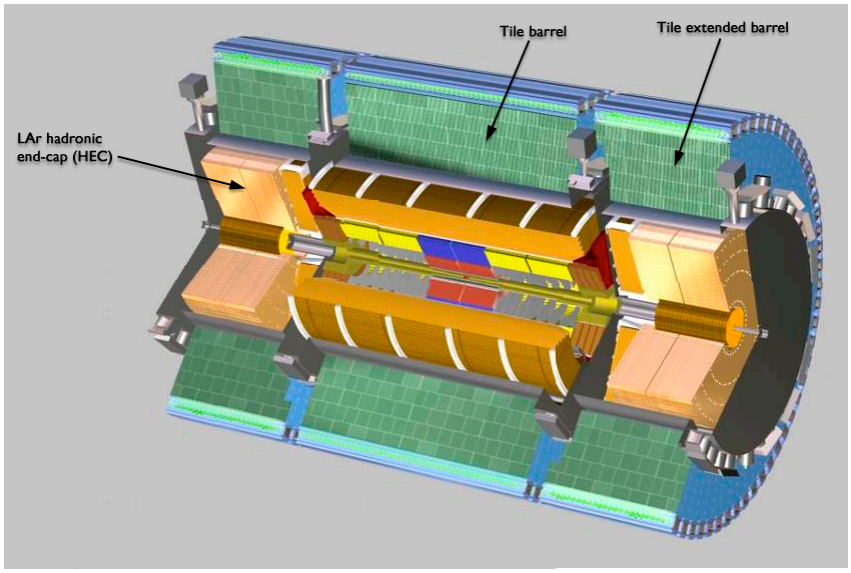

Figure 2.10: The hadronic calorimeters in ATLAS.

With a inner radius of 2.28m and an outer radius of 4.25m, the TileCal is placed around the EM calorimeter. It is divided in two parts: a barrel that covers $|\eta| < 1.0$ and two extended barrels, on each side of the central barrel, that cover $0.8 < |\eta| < 1.7$. The central barrel is 5.8m in length and each extended barrel is 2.6m. This is equivalent to approximately 7.4 λ. The TileCal is also segmented azimuthally into 64 modules with $\Delta\phi \approx 0.1$. It is also segmented into 0.1×0.1 cells in $\Delta\eta \times \Delta\phi$.

The TileCal is a sampling calorimeter as well, where alternate layers of steel and scintillating tiles (figure 2.11) act as the passive absorber and the active medium, respectively. When particles interact with the scintillating

tiles, light is produced. At the edge of each tile, wavelength-shifting fibers collect the light and pass it to photomultipliers (PMT's) that produce an electric signal proportional to the energy deposited by the interacting particle. The orientation of the scintillating tiles, combined with the wavelength-shifting fibers, give the TileCal a near uniform coverage in ϕ.

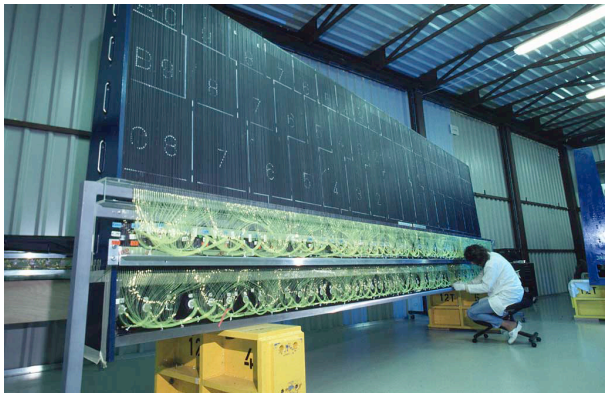

Figure 2.11: Picture of the scintillating tiles in a module of the TileCal.

Each HEC consists of two independent wheels placed next to the EMEC. The wheels have an approximate outer radius of 2m and they extend the pseudorapidity coverage of the hadronic calorimeter to $1.5 < |\eta| < 3.2$. The HEC uses LAr technology, similar to the electromagnetic calorimeter, with copper serving as the absorber instead of lead. The HEC cells have a granularity of 0.1×0.1 for $|\eta| < 2.5$ and 0.2×0.2 for larger pseudorapidities.

The Forward Calorimeter To extend the pseudorapidity coverage of the calorimeters, two forward calorimeters [33] (FCal) exist in ATLAS, on each side of the barrel. They are placed around the beam pipe, on each side of the ID and this is shown in figure 2.12. They are approximately 10 interaction lengths deep and cover the region $3.1 < |\eta| < 4.9$.

LAr technology is used in these calorimeters, as layers of liquid argon alternate with layers of an absorber. The FCal is segmented into three modules in z. One of the modules (the closest to the ID) is optimized for electromagnetic measurements and the passive material used is copper. The other two modules use tungsten absorbers to make, predominantly, hadronic measurements.

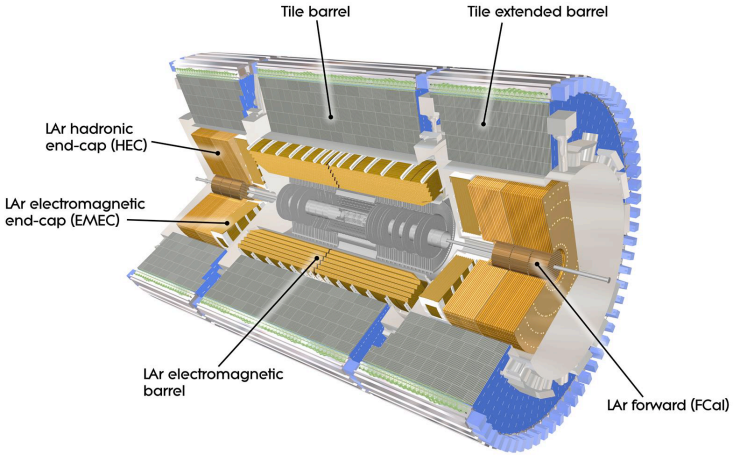

Figure 2.12: The full calorimeter system in ATLAS, including the forward calorimeters.

2.2.1.4 The Muon Spectrometer

The muon spectrometer [33] occupies the outermost part of the ATLAS detector. The schematics of the muon spectrometer, as well as of the toroid magnets that provide the magnetic field for this system, are presented in figure 2.13. Essentially, in the barrel region the muon chambers are placed in cylindrical layers around the beam axis, whereas in the endcap regions the muon chambers are placed perpendicular to the beam axis.

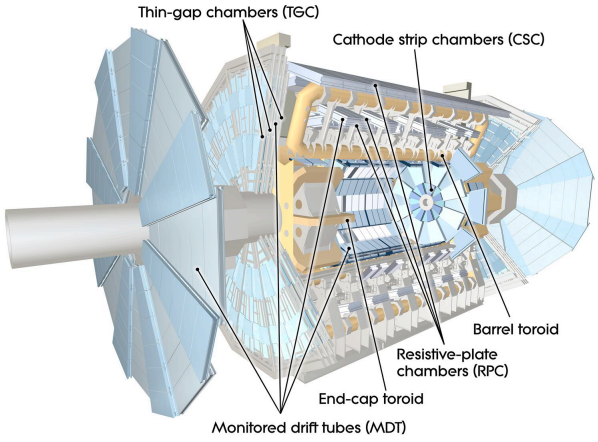

Figure 2.13: Diagram of the ATLAS muon system, including the components of the muon spectrometer and the toroid magnets.

The system was designed to detect charged particles that leave the barrel and endcap calorimeters, which will be mostly muons. Since it is embedded in a magnetic field generated by the toroid magnets, it can also measure the momenta of those particles. Finally, the muon spectrometer system also has the ability to trigger on the particles that reach the muon chambers. The total coverage of the chambers is $|\eta| < 2.7$ (2.4 for triggering).

Because the muon spectrometer cannot simultaneously offer spatial resolution for precision physics measurements and time resolution for triggering, two types of chambers were developed: the precision-tracking chambers and the trigger chambers. The Monitored Drift Tubes (MDT's) provide the reconstruction of the tracks in most of the η range. For larger pseudorapidities, the Cathode Strip Chambers (CSC's) make higher granularity measurements. Resistive Plate Chambers (RPC's) in the barrel region and Thin Gaps Chambers (TGC's) in the endcaps provide bunch crossing identification, well defined p_t thresholds and particles coordinates for trigger purposes.

2.2.2 The Trigger System

As said before, bunches of protons from the LHC beams will cross in the interaction points 40 million times per second. Since up to 23 pp collisions can result from a bunch crossing, the LHC will generate collision data at a rate of $\approx$ 1GHz. A very robust trigger system is, thus, needed, so that ATLAS can handle this challenging environment.

The role of the trigger system [33, 34, 35] is to decide whether an event is important for ATLAS or not. The decision is made *online*, i.e., in real time, as the collisions happen. "Uninteresting" events are permanently discarded by the trigger in order to reduce the input rate by more than five orders of magnitude (200Hz) and ensure data can be stored for further *offline* analysis. Since events are permanently eliminated, the trigger has to be highly unbiased and efficient, otherwise important and rare signals will be lost.

The ATLAS physics program is ambitious and requires the identification of several different signatures. The variety of signatures translate into the trigger being able to identify and make a decision on final states with objects such as: charged leptons (at low and high p_t), high-p_t jets (from quarks and

gluons), electroweak gauge bosons (W, Z, γ) and missing transverse energy (E_t^{miss}, from weakly interacting neutral particles like neutrinos).

The ATLAS trigger uses data from the various ATLAS subdetectors - inner detector ("tracking"), calorimeters ("calo") and muon spectrometer ("muon") - and works in three distinct levels: level-1 (LVL1 or L1), level-2 (LVL2 or L2) and event filter (EF). Each level refines the decision made by the previous one and applies additional selection criteria if necessary. LVL1 is hardware-based, whereas LVL2 and EF, together know as High Level Trigger (HLT), are implemented in software. Figure 2.14 shows the ATLAS trigger architecture. In the following sections, the behavior of the trigger will be presented, but given its relevance to the work presented here, only the calorimeter (Calo) trigger will be explored.

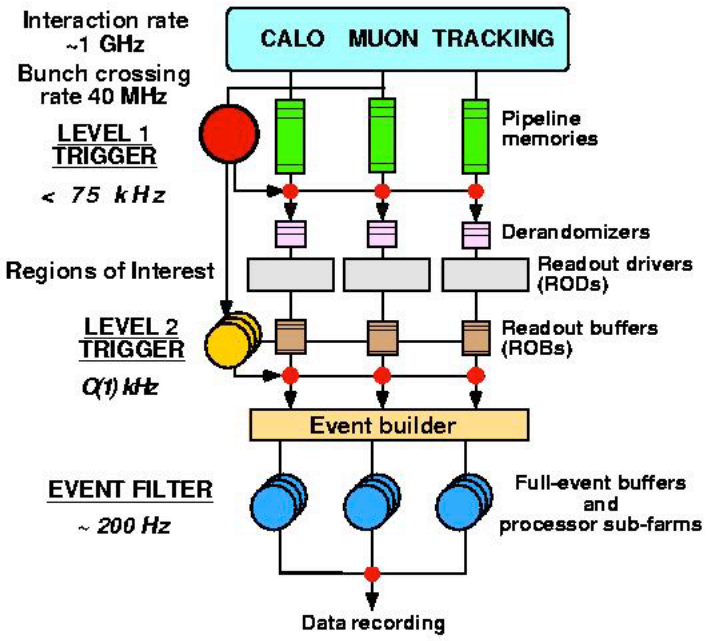

Figure 2.14: Schematic view of the ATLAS trigger system [36].

2.2.2.1 Level-1 Calorimeter

From the calorimeter trigger [33, 34, 35, 36] point of view, the ATLAS calorimeters (both LAr and TileCal) are segmented into 7200 trigger towers. A tower is a summation of calorimeter cells across η. The summation of cells

is done separately, meaning that there are EM and hadronic towers. Trigger towers have a reduced granularity of approximately 0.1×0.1 in $\Delta\eta \times \Delta\phi$ in most parts except at higher η, as depicted in figure 2.15.

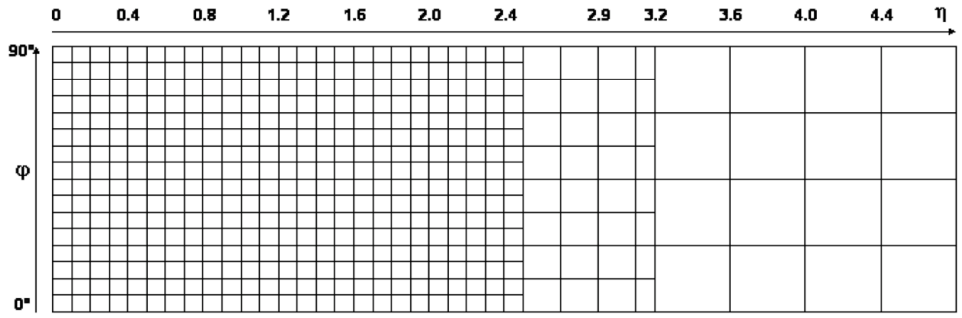

Figure 2.15: Trigger tower granularity for $\eta > 0$ and one quadrant in ϕ [36].

L1Calo trigger starts by accessing the coarse-grained calorimeter information for each bunch-crossing. This means looking at energy depositions in the calorimeter cells produced in each event. Then, LVL1 evaluates the pattern of those depositions and identifies them as candidates of basic objects, such as high-E_t electrons, photons, taus and jets. From the depositions, LVL1 can also produce global sums of transverse energy, like total E_t, total E_t^{miss} and total transverse energy deposited by jet candidates. Finally, isolation can be required for electrons, photons and τ, meaning LVL1 will only identify these high E_t objects if they have a minimum angular separation between them.

After the identification, LVL1 makes the trigger decision using a trigger menu, i.e., a set of multiplicities, energy thresholds and prescales. In other words, LVL1 is given a set of parameters - the multiplicities set the minimum number of candidate objects per event; the energy thresholds require that at least one object in the event is above a given value of transverse energy; and a prescale of x tells LVL1 to only accept 1 in every x events - and decides which events to eliminate and which ones to keep based on this.

While LVL1 algorithms process the information and a decision is made, the full event information is held in pipeline memories as shown figure 2.14. LVL1 algorithms are kept simple, to make fast decisions, and are executed by custom electronics. In fact, LVL1 receives data from the LHC at a rate of 40MHz and makes a decision within 2.5μs to reduce the output rate to

$\approx$ 75kHz.

Once the decision is made and an event is accepted by LVL1, the data held in the pipelines memories referring to that event, is read by the Readout Drivers (ROD's) and stored in the Readout Buffers (ROB's). If the event does not actually pass LVL1 selection criteria, it is permanently deleted.

2.2.2.2 Level-2

As mentioned in the previous section, LVL1 makes a decision based on the multiplicity of the identified objects and on whether or not they pass the E_t thresholds. Information about the geometric location of the objects is actually kept in Regions of Interest (RoI's). An RoI is, thus, a small amount of information (the type of object and its η and ϕ coordinates) produced by LVL1 for every identified object. Once LVL1 makes a decision and accepts an event, the selection criteria that led to the event being accepted is attached to the RoI's of the objects identified in that event. Finally, the RoI's are passed to LVL2. This means that, in essence, an RoI flags a calorimeter region that requires further analysis.

LVL2 trigger [33, 34, 35] starts from the RoI's delivered by LVL1. LVL2 feature extraction algorithms request calorimeter information stored in the ROB's, around the center of the RoI. Then, the hypothesis algorithm determines whether the identified object is a valid object, by analyzing, for example, the shape of the energy deposition. If none of the objects in the event are considered valid, the event is rejected by LVL2. These algorithms are simple algorithms so that LVL2 performs fast but are, nonetheless, very robust.

After this confirmation process, additional information about the objects is searched for in other subdetectors, such as the inner detector. The full information available is, then, combined and more refined and specialized trigger objects are created. These LVL2 objects serve as input for LVL2 decision. LVL2 processes information and makes a decision on an average of 40ms, reducing the event rate from an input of 75kHz to an output of $\approx$ 1kHz.

2.2.2.3 Event Filter

The final online selection step is performed by the EF [33, 34, 35]. At this point, all the data is collected from the ROB's and the full event is built. Contrarily to the previous trigger levels EF operates on complete events. Furthermore, unlike LVL1 but similarly to LVL2, EF uses the full granularity of the detector. Thus, EF runs a set of offline-like algorithms over the events in order to refine the reconstruction. These algorithms are more complex than the ones used by the previous trigger levels, since the processing time available at this stage is larger. In particular, EF takes $\approx$ 2s to run them and make a decision.

After improving event reconstruction, EF makes a decision that reduces the amount of data to a final storage rate of 200Hz. For those events accepted by EF, the information related to EF selection criteria that led to the event being accepted is appended to the information of the refined event and the full event information is recorded in the ATLAS database. This way, subsequent offline analysis can be seeded by the results from EF. As done in the previous trigger levels, if an event is not accepted by EF, it is permanently deleted.

EF still performs one final operation before the data is recorded, that is to classify each event according to the ATLAS physics streams: electrons, muons, jets photons, missing transverse energy, taus, and B-physics. A subset of events can also be classified as calibration stream, in which case, the events will be used for detector calibration purposes.

2.2.3 The Computing Model

The ATLAS Collaboration has developed a computing model [37, 5, 38], i.e. a set of software and middleware tools that allow scientists all over the world to produce, access, reconstruct and analyze ATLAS data. This data could be either simulated data or real data collected in the ATLAS detector from real collisions at the LHC. The software framework is called ATHENA and it operates on a hierarchical model of computing - the GRID.

The process of simulating and reconstructing events in ATLAS is very CPU intensive. Moreover, it is expected that the amount of data produced will be too large for individual scientists to have local access to the whole

data set. Thus, the idea behind the GRID is to have a distributed computing framework throughout several facilities in remote locations, each one being able to communicate and share tasks. These facilities are called tiers. Tier-0 is located at CERN and handles the most unrefined data. Ten worldwide facilities constitute tier-1, that deals primarily with reconstruction of events. Approximately 35 more facilities form tier-2, that provides the analysis capacity for the ATLAS Collaboration.

As for the ATHENA software framework it allows, for example, the simulation of the collisions at the LHC. The first step for this is the generation of events, which is done using a MonteCarlo event generator, such as PYTHIA. These MonteCarlo generators simulate the *pp* collision and generate the output of that collision. After generation, GEANT, a simulator of the ATLAS detector (material, geometry and subsystems) can be used. In other words, the generated output can be passed through GEANT to simulate the way real particles produced at the LHC will cross the ATLAS detector. Digitization is the final step of the simulation process. At this point, the ATLAS subsystems' response to the generated particles is simulated. The trigger is included in these subsystems as well. Nevertheless, the simulated trigger performs only the identification and reconstruction of objects, without actually selecting or discarding events. After digitization RAW Data files are produced. It is, now, important to note that RAW Data is, also, what comes as output of the EF trigger in real data coming from real collisions at the LHC.

In summary, whether ATLAS data is simulated or real, its most primary form is called RAW Data. Once collected, the RAW Data is transferred to Tier-0, where the offline reconstruction is performed, both in simulated and experimental events. The output of these reconstruction algorithms is typically ESD (Event Summary Data) or AOD (Analysis Object Data) files that are exported to the various tier-1 and tier-2 locations. They are smaller than RAW Data and more analysis-oriented. From these, DPD's (Derived Physics Data) can also be obtained. These are light, n-tuple-like files, that contain only a small amount of information on the events, to be used for direct analysis by the individual scientists. The offline reconstruction process is expected to have a latency of approximately 8 hours for the calibration streams. As for the physics streams, it is expected that their reconstruction

is done within 48 hours after the data acquisition.

Chapter 3

Jets in ATLAS

3.1 Jet Reconstruction

As seen in section 1.2.2 the production of jets in the LHC will be very significant. On the one hand they will represent signatures for many physics processes, such as the ones depicted in figure 3.1. On the other hand, being among the most commonly observed objects in ATLAS, jets will constitute background for nearly every physics analysis as well. In the end, whether jets are signal or background (or both) for a given physics analysis, highly efficient jet reconstruction is fundamental. In fact, for precise physics measurements, ATLAS requires at least 1% precision in the jet energy scale. Therefore, high quality reconstruction involves accurate jet identification and precise determination of the jet energy, which is only achieved through calibration [39, 23].

Take, for example, the top quark, shown in figure 3.1(a). Being a very unstable particle, t always decays into a W boson and a bottom quark before it hadronizes. The bottom quark, being a quark, will hadronize into a jet. As for the W boson it can decay via two channels: through the leptonic channel (branching ration of $\approx 11\%$ [4]), generating a lepton and a neutrino, or through the hadronic channel (branching ratio of $\approx 68\%$ [4]), decaying into two quarks that will hadronize and form jets. Regardless of the decay mode of the W boson, it is clear that doing precision studies on the properties of the top quark requires efficient jet reconstruction.

Another example is the production of the Higgs boson through vector

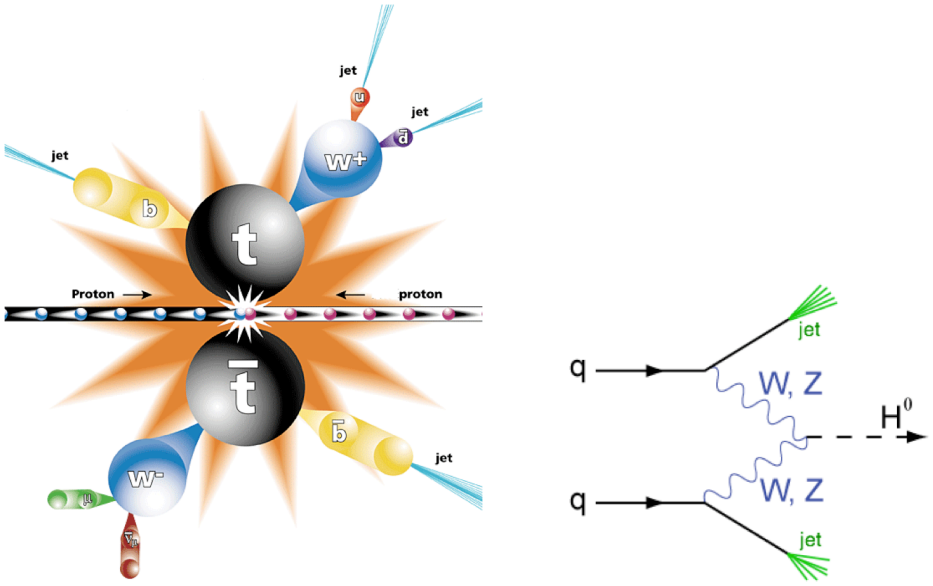

(a) Top quark decay modes.

(b) Higgs production through vector boson fusion.

Figure 3.1: Some physics processes that will be observed in ATLAS having jets as final states.

boson fusion, a process depicted in figure 3.1(b). The figure shows that this process will produce final states with two jets. Thus, once again, the precision of the analysis on the Higgs boson depends highly on the efficiency of the jet reconstruction.

The subject of jet reconstruction was first introduced in section 1.2.3. The way ATLAS handles jet reconstruction is presented in the following sections. In reality, three reconstruction sequences are used in ATLAS. They are depicted in figure 3.2 and differ mostly on the input for jet identification (towers or clusters) and energy calibration scheme (global or local). Given the relevance to the work developed in this thesis, only the first two sequences, which use a global calibration scheme, will be addressed in the following sections [23].

3.1.1 Jet Identification

The calorimeters (section 2.2.1.3) are the most important system for jet reconstruction in ATLAS. It is in the calorimeter cells that jets produced

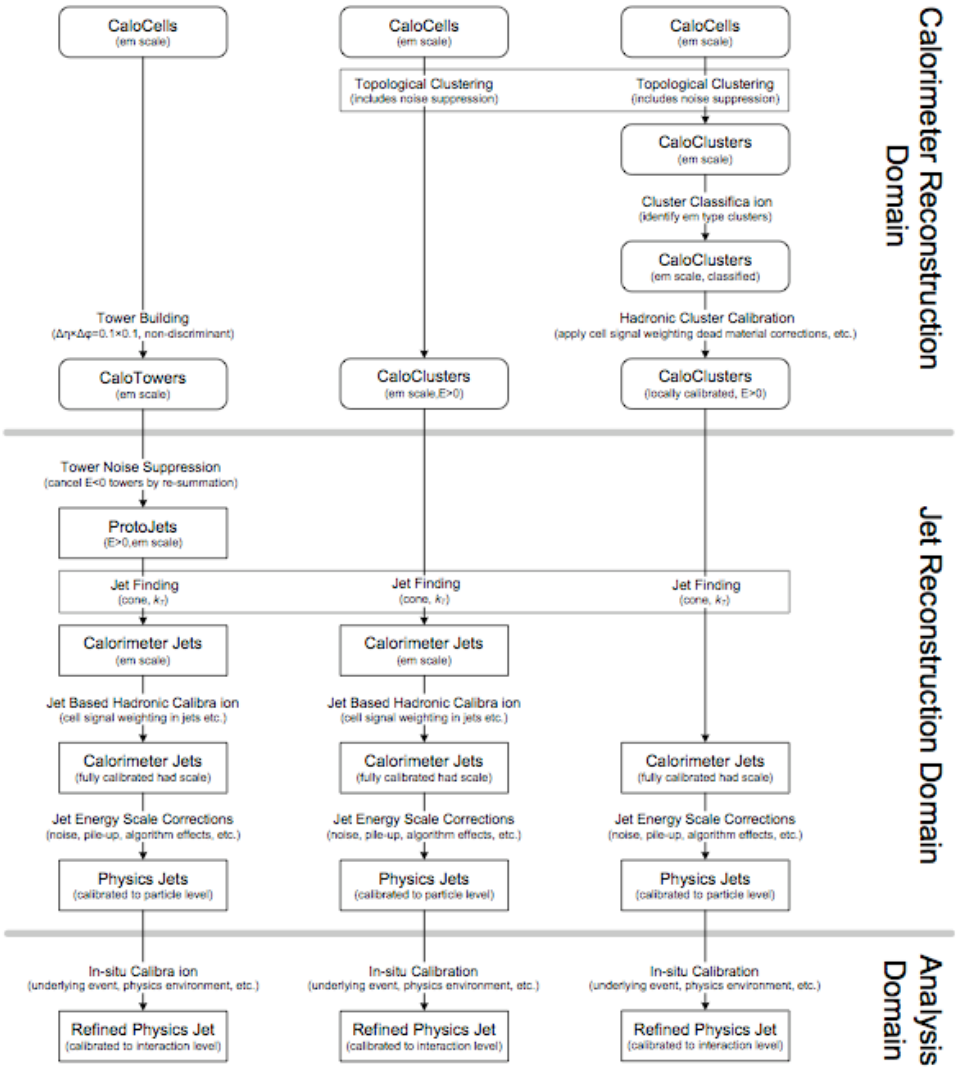

Figure 3.2: Schematic view of the reconstruction sequences for ATLAS calorimeter jets [23].

in the LHC collisions leave their signals, in the form of energy depositions. Thus, calorimeter cells provide the first input for the jet reconstruction, which can come in two forms: tower signals and topological cell clusters [23].

The difference between the two is related to the way the individual cells are combined into meaningful signals to be used by the jet algorithms (section 1.2.3.1). Also, because of the differences, determining which of the two calorimeter signals will lead to a better jet reconstruction is dependent on

the type of jets produced, including their energies and shapes, on which calorimeter region they are located (central or more forward) and on the jet algorithm applied to the signals. The sequence to identify calorimeter jets from these two types of calorimeter signals is presented next [23, 20, 22]. Figure 3.2 depicts the process.

A tower is, basically, a summation of cells. All cells belonging to a tower have the same (η, ϕ) coordinates, corresponding to the center of the tower, and the towers' size is $\Delta\eta \times \Delta\phi = 0.1 \times 0.1$. Each tower is considered a massless pseudo-particle and is attributed a four-momentum $(E, \overrightarrow{p})$, that results from the summation of the signals of each cell that belongs to the tower. In particular, the following relations apply to the four-momenta of the towers:

$$E = |\overrightarrow{p}| = p = \sqrt{p_x^2 + p_y^2 + p_z^2}$$

$$p_x = p\frac{\cos\phi}{\cosh\eta}$$

$$p_y = p\frac{\sin\phi}{\cosh\eta}$$

and

$$p_z = p\tanh\eta$$

ATLAS has a pseudorapidity coverage of $|\eta| < 5$ and ϕ ranges $[-\pi, \pi]$, which means there are $1000 \times 64 = 6400$ towers in total.

Jet identification from towers begins with a re-summation step that has the purpose of suppressing noise. This is done because the signals produced by the cells fluctuate due to electronic noise. Since a tower is a summation of cells, it can happen that the four-momentum of the tower is physically meaningless, i.e., the tower has $E < 0$. These towers cannot just be ignored, since such a procedure would enhance the contribution of positive noise fluctuation, producing a bias. Instead, they are combined with nearby towers that have positive and valid signals, in such a way that the resulting energy is positive. If no nearby towers with positive signals exist, the negative-signal tower is discarded.

After this step, one has a set of "protojets", that are formed by one or a few towers, all with physically valid signals, and that will constitute the actual input for the jet algorithm. After the jet algorithm is applied, the

outputs are calorimeter jets whose constituents are the original calorimeter towers.

As for topological cell clusters, they are the attempt to gather cells into three-dimensional "energy blobs" that represent the energy depositions left by the particles that form the jets. Just like for towers, a four-momentum is calculated for each cluster and the relations presented for towers also apply. Concerning the (η, ϕ) coordinates of the clusters, they are reconstructed from the energy-weighted coordinates of the cells.

The jet identification sequence for topological clusters is similar to the one applied to towers, the main difference being the treatment of noise. The clustering procedure applied to the calorimeter cells includes noise suppression. This means that clusters, just like towers, can have a net negative signal, but unlike towers, they can be ignored without biasing the reconstruction, due to the way they were built. Thus, the topological clusters serve directly as input for the jet algorithm.

Concerning, now, the jet algorithms, several are used in ATLAS, but the most common are the cone and k_T algorithms [23]. Given its importance to this work, the cone algorithm [19] will be presented here:

1. It begins by searching through all the objects (towers or topological clusters) in order the find the one with the higher transverse energy (E_t), usually required to be above a certain threshold (1 or 2GeV). This object will serve as a seed for the algorithm.

2. A cone with a predefined radius, R_{cone}, is centered in the position of the seed, (η_0, ϕ_0) forming cone-0. In ATLAS, cones of 0.4 and 0.7 are usually used.

3. Every object i whose coordinates (η_i, ϕ_i) fall inside the cone is selected. In other words, if for an object i,

$$\Delta R_i = \sqrt{(\eta_i - \eta_0)^2 + (\phi_i - \phi_0)^2} \leqslant R_{cone}$$

   then i is selected.

4. Let us say that a total of n objects fall inside the cone. Those are used to determine a new position (η_1, ϕ_1) for a new cone - cone-1:

$$\eta_1 = \frac{\sum_{i=0}^{n} E_i \eta_i}{\sum_{i=0}^{n} E_i}$$

and

$$\phi_1 = \frac{\sum_{i=0}^{n} E_i \phi_i}{\sum_{i=0}^{n} E_i}$$

5. If the distance between cone-0 and cone-1 is

$$\sqrt{(\eta_0 - \eta_1)^2 + (\phi_0 - \phi_1)^2} < 0.05$$

then a jet is built from cone-1. This means that the jet is a cone with a radius R_{cone}, centered at (η_1, ϕ_1) and four-momentum that is the sum of the four-momenta of all the objects falling inside cone-1.

6. If cone-0 and cone-1 are too far apart, the objects falling inside cone-1 are used to create cone-2, in the same way cone-1 was created from objects inside cone-0. This iteration process goes on N times, until the distance between cone-N and cone-(N-1) is smaller than 0.05. At this point, a stable jet is created from cone-N, as described before.

7. Finally, a new object is picked as a seed and the process is repeated until all stable jets in the event are identified.

3.1.2 Jet Energy Measurement

The ATLAS calorimeters are calibrated to correctly reproduce the energy of an electron, i.e., they are set to what is called electromagnetic energy scale (EM-scale). Thus, the calorimeter signals mentioned in the previous section, used as input for the jet reconstruction, are also at EM-scale, as are the calorimeter jets obtained from them (figure 3.2). However, because of non-compensation, EM-scale underestimates the actual energy of the calorimeter jet. Also, when the particles resulting from the parton hadronization interact with ATLAS detector, part of their energies are lost in the dead material, cracks and gaps of the detector. The magnetic field of the ATLAS detector may also cause the energy of the particles to be lost, since it bends them outside the jet. Finally, physics effects caused by pile-up, the underlying event, hadronization, ISR and FSR can greatly influence energy measurements in ATLAS [20, 22].

These subjects had already been addressed in section 1.2.3.2 and, basically, constitute the reason why calibration of the jet energy is performed in

ATLAS. Energy calibration in ATLAS is done in two major steps, as indicated by figure 3.2. The first step corrects the energy of the reconstructed jet to particle level, whereas the second step brings the jet energy scale to the desired parton level. The approach used by ATLAS to perform the first calibration step is discussed next. As for the second step, which is used to correct for the mentioned physics effects, it will not be discussed here in detail, since it is very dependent on the type of analysis that one wishes to do [23].

The default calibration procedure [23] used in ATLAS was first developed for the CDHS experiment [40] and later refined for the H1 experiment [41]. It takes the identified calorimeter jets at EM-scale (uncalibrated), corrects for non-compensation and produces calorimeter jets at hadronic-scale (calibrated). In fact, the procedure also corrects for noise, dead material, cracks and particle deflection in the magnetic field. Thus, once calibration is applied to the identified calorimeter jets at EM-scale, one obtains jets calibrated at particle level, as shown in figure 3.2. The ATLAS calibration procedure is described next.

Ultimately, the energy of a reconstructed calorimeter jet, regardless of the type of signal input or jet algorithm used, can be written as

$$E_{uncalibrated} = \sum_{i=cells} E_i$$

where E_i is the energy, at EM-scale, deposited in cell i, that is a constituent of the jet. The calibration of this energy is done by multiplying the energy in each cell by a weight w_i, i.e.,

$$E_{calibrated} = \sum_{i=cells} w_i E_i$$

The weights are a function of the location of the cell ($\overrightarrow{x}_i$) and the energy density of the cell itself - $\rho_i = E_i/V_i$, with V_i being the volume of the cell.

The use of these energy density-dependent weights is related to the fact that electromagnetic showers are denser and more compact than hadronic showers. Consequently, a high density signal in a calorimeter cell indicates an electromagnetic signal, whereas low density signals are, more likely, hadronic signals. Thus, the weighting factor is ≈ 1 for high density signals and can rise up to 1.5 with decreasing densities.

Also, it is important to note that these weights are universal, in the sense that they are independent of the jet algorithm or calorimeter input used to reconstruct the jet. In summary, the calibrated four-momentum of a jet is:

$$(E_{calibrated}, \overrightarrow{p}_{calibrated}) = \left(\sum_{i=cells} w_i(\rho_i, \overrightarrow{x}_i) E_i, \sum_{i=cells} w_i(\rho_i, \overrightarrow{x}_i) \overrightarrow{p}_i \right)$$

The calibration weights $w_i(\rho_i, \overrightarrow{x}_i)$ are calculated using MonteCarlo simulated QCD dijet events. To begin with, the simulated calorimeter signals are reconstructed into simulated calorimeter jets using a cone algorithm. Then, the corresponding particle jets are built, by applying the same jet reconstruction algorithm directly to the stable[1] particles produced by the hadronization model in the MonteCarlo generator. Since the calibration weights are meant to calibrate calorimeter jets to particle level, these particle jets constitute the reference and are, for that reason, referred to as truth jets. Thus, the four-momenta of the calorimeter jets is compared to the four-momenta of the corresponding truth jet and the weight is determined is such a way that the quantity

$$\chi^2 = \sum_{i=jets} \left(\frac{E_i^{calibrated} - E_i^{truth}}{E_i^{truth}} \right)^2$$

is minimized. Here, $E_i^{calibrated}$ is the calibrated energy of the simulated calorimeter jet i and E_{truth} is the energy of the truth jet corresponding to the i^{th} calorimeter jet. The weights are parametrized as having a logarithmic dependence:

$$w_i(\rho_i, \overrightarrow{x}_i) = a(\overrightarrow{x}_i) \log(\rho_i)$$

3.2 Jet Trigger

The importance of a trigger system in ATLAS, to handle the high rate environment created by the LHC, was discussed in section 2.2.2. Figure 3.3 shows the cross sections and equivalent rates at which several objects will be produced at the LHC, as a function their masses/transverse energies,

[1] "Stable" meaning those particles with a laboratory frame lifetime of about 10ps, such as electrons, muons, photons, charged pions, kaons, protons, neutrons and neutrinos and their corresponding antiparticles

as well as the input and output rate for the ATLAS trigger system. It is clear from this figure that jets are the objects which will be most commonly produced at the LHC. In other words, the high rate environment of the LHC will be severely dominated by jet events. Thus, it is essential that part of the ATLAS trigger system - the jet trigger - is dedicated to identifying, calibrating and rejecting jets in events [35].

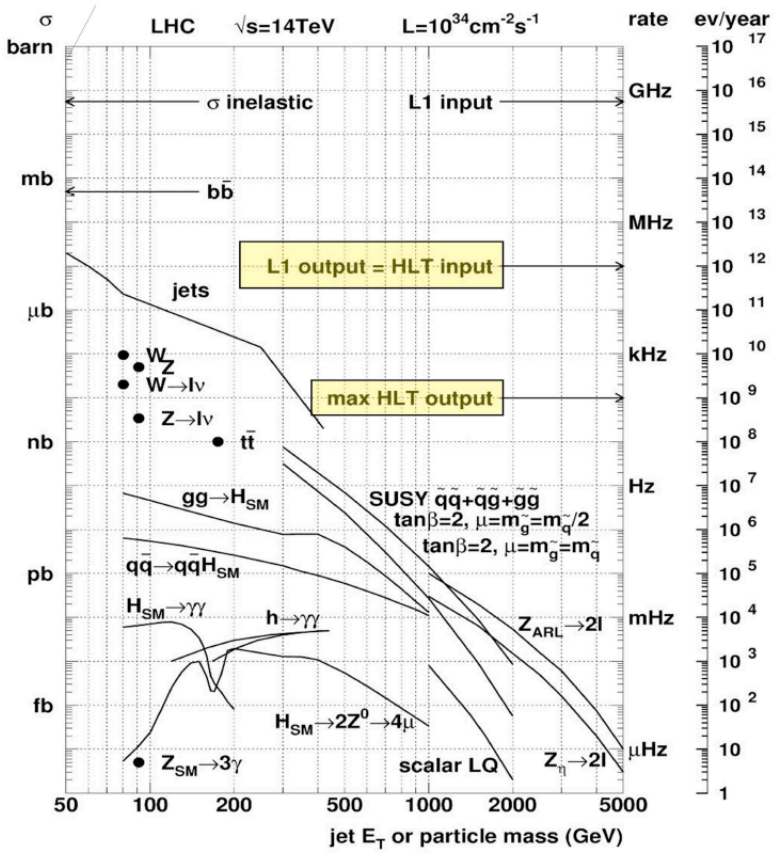

Figure 3.3: Cross sections for several processes as a function of the mass / transverse energy of the particle / jet produced from *pp* collisions at the LHC nominal operating conditions; the trigger input and output rates are also indicated.

As discussed previously in the beginning of this chapter, jets are necessary for a wide variety of physics analysis. Nevertheless, they are produced at the LHC at a higher rate than the one ATLAS can handle. The approach of the ATLAS jet trigger is to use prescales to reduce the jet rate and still

obtain a jet p_t spectrum large enough to cover all the physics topics. However, the main challenge for the ATLAS jet trigger is that, at the LHC, the background for jets are also jets. Thus, the jet trigger has to be able to efficiently reconstruct jets and accurately determine their energies, so that high-p_t jets can be distinguished from low-p_t ones [39].

In summary (section 2.2.2), the ATLAS jet trigger [35, 34] first identifies jets at LVL1 using a dedicated trigger menu and accessing calorimeter information. Then, LVL1 information is passed on to the HLT, which refines the jet reconstruction and provides the final necessary event rejection. This is further developed in the following sections.

3.2.1 Level-1

In section 2.2.2.1, it was mentioned that the L1Calo trigger evaluates energy depositions in the ATLAS calorimeters and identifies basic objects, one of these being jet candidates. In summary, the goal of the jet trigger at LVL1 [35, 34, 36] is, thus, to identify hadronic jets using calorimeter data, classify them according to E_t and multiplicity and provide their RoI's and classification to the HLT.

At LVL1 jet candidates are made of jet elements, which are the sum of 2×2 trigger towers. Thus, LVL1 jet candidates have a granularity in their positions of 0.2×0.2 in $\Delta\eta \times \Delta\phi$. They are identified using a sliding window of programmable size, that can be 2×2, 3×3 or 4×4 jet elements. In this thesis, only the 4×4 window size will be considered. The sliding window searches the trigger towers for energy depositions. The step size for the sliding window is the size of a jet element, i.e. 0.2 for both η and ϕ.

A jet candidate is identified if its transverse energy is above the threshold defined by the jet trigger menu. The transverse energy of a jet candidate is calculated by summing the E_t of all the calorimeter cells within the sliding window. Furthermore, to avoid overlapping between the identified jets, the transverse energy within a cluster is required to be a local maximum, a cluster being the sum of 2×2 jet elements within the window. For each jet candidate identified at LVL1 an RoI is generated containing the (η, ϕ) coordinates of the center of the sliding window and the energy threshold passed by the jet candidate. The RoI's are passed on to the HLT, which continues the jet identification process, refining the reconstruction. The

processes of jet identification by LVL1 is schematized in figure 3.4.

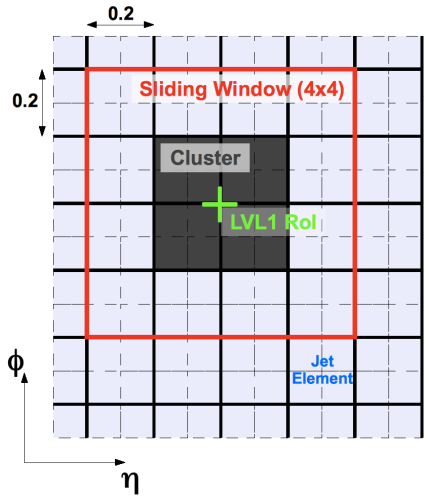

Figure 3.4: Representation of the calorimeter cells in the (η, ϕ)-space and the LVL1 jet trigger identification algorithm.

It is also important to refer the behavior of the jet trigger in the forward calorimeters ($|\eta| > 3.2$). Contrary to the other calorimeters, trigger towers in the FCal have a granularity of 0.4×0.4 in $\Delta\eta \times \Delta\phi$. Consequently, jet elements in the forward region have a $\Delta\phi$ granularity of 0.4 and only one or two η bins, depending if the "backward" or "forward" region is considered.

As mentioned, the energy of LVL1 jets is determined directly from calorimeter cells. An intermediate simple calibration step is applied by weighting the signals in the hadronic calorimeter cells [42]. Nonetheless, the energy scale remains very close to EM-scale. Thus, the LVL1 jet energy scale shows variations, both with E_t and η, ranging from 70% to 90%.

3.2.2 Level-2

The ATLAS calorimeter system has more than 10^5 individual readout channels. In order for LVL2 algorithms to achieve the required execution time of 40ms, the amount of data analyzed must be kept to a minimum (section 2.2.2.2). Consequently, the LVL2 jet trigger [34, 35, 43] accesses only calorimeter data that lies within a rectangular window of 1×1 in $\eta \times \phi$, centered around the LVL1 RoI. Nevertheless, LVL2 algorithms perform with full granularity of the calorimeters. Thus, the position and transverse energy

associated to each calorimeter cell falling into the LVL2 window is extracted and used for LVL2 jet reconstruction.

LVL2 jets are reconstructed with a simplified version of the cone algorithm described in section 3.1.1. The radius of the cone is chosen to be 0.4 and the seed for the algorithm, i.e. cone-0, is defined by the LVL1 RoI. Because of time constraints, the iteration process is executed a fixed number of times, usually $N = 3$. This process is depicted in figure 3.5. Equivalently to

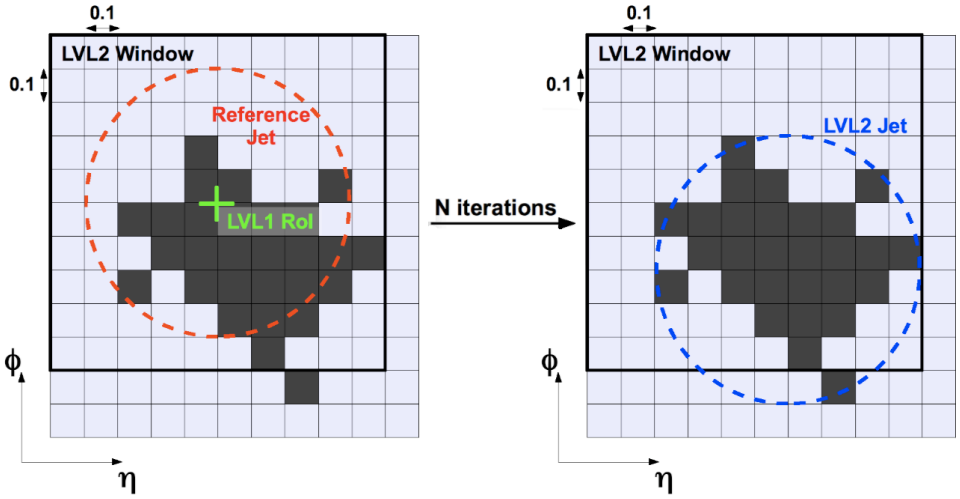

Figure 3.5: Representation of the calorimeter cells in the (η, ϕ)-space and the LVL2 jet trigger identification algorithm, seeded by the LVL1 RoI; the darker cells indicate energy depositions.

LVL1, the output of the LVL2 jet identification algorithm is a uncalibrated jet. However, at LVL2, a calibration step is applied, in order to improve the jet energy scale, setting it to hadronic. This means that LVL2 transverse energy thresholds are applied to calibrated jets.

The LVL2 calibration procedure [43, 44] is a simplified version of the sampling calibration method [45] and applies two weights to the signals of the calorimeter cells. One of the weights is applied to the energy of the jet measured in the hadronic calorimeter and the other to the energy collected by the electromagnetic calorimeter. So basically, the calibrated energy of the i^{th} jet is given by

$$E_i^{calibrated} = w_i^{EM} E_i^{EM} + w_i^{Had} E_i^{Had}$$

The weights w_i were calculated using MonteCarlo simuated QCD dijet

events, in a similar way to the one described in section 1.2.3.2. In summary, LVL2 simulated jets are compared to their corresponding jets at particle level, i.e., to the corresponding truth jets. The minimization function is, however, slightly different:

$$S = \sum_{i=jets} \left(\frac{E_i^{truth} - E_i^{calibrated}}{\sigma_i} \right)^2$$

where σ_i is the resolution of the jet. Also, the weigths have a logarithmic dependence on the truth energy of the jet E_i:

$$w_i = a + b \log E_i^{truth}$$

with a and b being different constants for the hadronic and electromagnetic weights, calculated in bins of η.

After calibration, the LVL2 jet energy scale is severely improved, being close to 100% in the whole η range of the detector, with fluctuations within 2%. As for the energy resolution, it is slightly improved by the LVL2 calibration method, varying between 12% for low E_t jets and 4% for transverse energies above 1000GeV.

3.2.3 Event Filter

The last step of online rejection is performed by Event Filter [35]. EF algorithms are offline-like algorithms (section 3.1) that were adapted to perform in the online trigger environment (figure 3.2), i.e., basically adopted to work in seeded mode.

More specifically, calorimeter cell information is extracted within a predefined window around the position of the jet found at LVL2. This is similar to the way the LVL1 RoI seeds the LVL2 algorithms. Then, towers are built from the selected cells, with a granularity of 0.1×0.1 in $\Delta\eta \times \Delta\phi$. Noise suppression is applied to these towers and, as a consequence, proto-jets are formed. Proto-jets serve as input to a 0.7-cone algorithm that identifies jets as described in section 3.1.1. Finally, the offline energy calibration (section 3.1.2) is applied to the identified jets. Jets whose calibrated energies are below the EF trigger thresholds are permanently discarded.

3.2.4 Jet Trigger Menu at the LHC Restart

A menu for the jet trigger is foreseen to be used when the LHC restarts its operations in mid-November 2009. The menu was designed to identify events with both single and multi-jet signatures, in the central and forward regions of the detector, in an environment with a luminosity of $\mathcal{L} = 10^{31}\text{cm}^{-2}\text{s}^{-1}$ [46].

Also, it is expected that, in the beginning of data taking and given the low-luminosity regime, the HLT will be running in pass-through mode, i.e., executing the full algorithms but accepting the events regardless of the algorithms' decisions, allowing the commissioning of the HLT. Thus, the proposed jet trigger menu [47] only includes LVL1 E_t thresholds and prescales and is presented in table 3.1.

Figure 3.3 shows how the jet production rate falls steeply with the increasing jet transverse energy. The jet trigger menu in table 3.1 was built so that the output LVL1 rate for jets would be approximately flat across the E_t spectrum. In other words, take the single jet signatures: the lowest E_t threshold of 5GeV and highest of 120GeV with a prescale of 1 guarantees that the jet production rate is constant for jets with E_t ranging from 5 to 120GeV. For jets with transverse energies above 120GeV, the production rate falls rapidly as determined by the cross-sections for the production of these jets. Nonetheless, this strategy provides large enough jet p_t spectrum and sufficient statistics for the first analysis.

Jet Trigger Menu			
Trigger	*Signature*	*Threshold [GeV]*	*Prescale*
Single Jets	J150	150	1
	J130	130	1
	J100	100	10
	J70	70	50
	J40	40	300
	J20	20	5000
	J10	10	100000
	J5	5	200000
Multi Jets	4J20	20	1
	4J10	10	20
	3J20	20	10
	3J10	10	20000
Single Forward Jets	FJ120	120	1
	FJ70	70	20
	FJ35	35	700
	FJ18	18	7000
Multi Forward Jets	2FJ70	70	1
	2FJ35	35	1
	2FJ18	18	100

Table 3.1: Jet trigger menu foreseen for the beginning of data taking at the LHC with a luminosity of $10^{31}\text{cm}^{-2}\text{s}^{-1}$.

Chapter 4

Performance of the Jet Trigger with Cosmic Events

4.1 Objectives and Motivation

Until the restart of the LHC, cosmic muons will be the only particles interacting with the ATLAS detector. Thus, they are currently being used to commission all the ATLAS subsystems, including the ATLAS trigger system. Given the enormous data flow that will be generated by the LHC, most of that data being produced by jet events, high performance of the jet trigger system is essential, as discussed in section 3.2.

In the present chapter, cosmic muons will be presented as a mean to assess the performance of the ATLAS jet trigger. In particular, the performance of the three trigger levels in identifying and reconstructing jets will be evaluated by comparison with the offline reconstruction. Furthermore, cosmic muons will help identify problems in the ATLAS detector that might influence the trigger behavior.

It is important to note that the studies presented here are limited. Cosmic muons constitute only a start point to monitor the quality of the data delivered by the jet trigger. Moreover, firm conclusions about the performance of the ATLAS jet trigger can only be taken once collision data is available.

4.2 Cosmic Muon Data Taking

The analysis of cosmic muon runs as a part of the ATLAS detector commissioning began in June 2005, during detector assembly. The runs were useful for studies of alignment, calorimeter energy and time response, cell quality control, etc., but because the detector was still not fully installed, not all systems participated in the runs and the detector was not exercised as a whole [48].

The short single-beam run at the LHC startup in September 10^{th} 2008 provided a "stress test" of the ATLAS detector. However, because the priorities for ATLAS at the LHC startup were stability and reliability, not all of the detector's subsystems participated in the run (the HLT, for example, was run offline). Although much useful experience was obtained, only limited work could be accomplished with this single-beam data [49].

After the LHC incident and starting September 13^{th} 2008, data taking was, once again, reverted to cosmics for detector commissioning purposes. Even though they cannot replace collisions, these cosmic runs presented the first opportunity to fully exercise the detector. Combined runs, where all ATLAS subsystems are involved and different detector operation modes and configurations are tested, are being taken in order to understand the detector performance, towards achieving the physics requirements, gain experience on the detector operation (from TDAQ to offline analysis), exercise the full data acquisition and trigger systems, process data in a more realistic scenarios, obtain first alignment, calibration constants and list of noisy cells, etc. In summary, to prepare the first LHC collisions later in 2009 [49, 50].

It is important to state that the use of cosmic muon runs for commissioning purposes requires that the differences between cosmic events and events originating from LHC collisions are taken into account. On the one hand, cosmic events are not synchronized with the readout clock since they occur randomly. On the other hand, tracks do not originate from the interaction point. On the jet trigger point of view, cosmics can be used despite the difference between a cosmic muon and a jet.

Most cosmic muons cross ATLAS undetected and deposit little or no energy in the calorimeters. Some, however, may interact with the materials via Bremsstrahlung and produce particle showers, leaving low energy depo-

sitions in the calorimeter cells. This can be seen in figure 4.1. Since the calorimeters are one of the systems providing input for the ATLAS trigger, those energy depositions can be identified by the jet trigger if the E_t thresholds are of the trigger menu are lowered. In this case, cosmic muons will be reconstructed as jets, even though no jets were created by the cosmic muons.

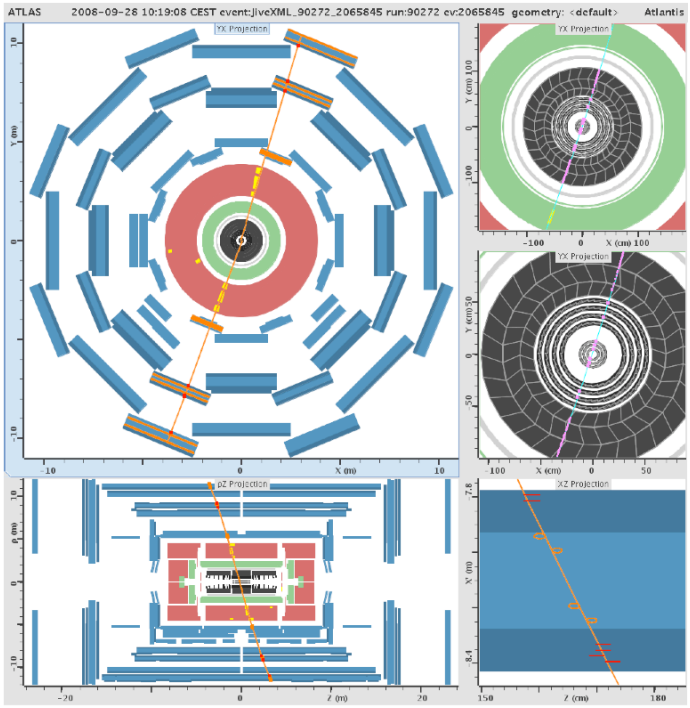

Figure 4.1: Display of a cosmic muon from run 90272 crossing the ATLAS detector and depositing energy in the TileCal cells [51].

To perform the studies described before, trigger jets (LVL1, LVL2 and EF) and offline reconstructed jets were evaluated using several cosmic muon runs. For the offline reconstruction, in particular, jets reconstructed using a 0.4 Cone algorithm were chosen, since those are the closest, in size, to LVL1 and LVL2 jets. Since the results obtained were similar for all the analyzed runs, only information referring to the analysis of the reprocessed data from cosmic run 90272 are presented here. Approximately 1/15 of the total number of events recorded were triggered by L1Calo and, from the latter, approximately 1/6 were used in these studies. Table 4.1 summarizes the relevant information about run 90272.

Run 90272	
Number of events recorded	5065168
Start date	28/09/2008
End date	28/09/2008
Duration [s]	57436 (aprox. 16 hours)
Number of events triggered at L1Calo	326996
Type	Physics
Prescale	1
Number of events analyzed	55438

Table 4.1: Information from cosmic muon run 90272 [52, 53].

4.3 Overall Data Quality Control

4.3.1 Preliminary Analysis

One of the first analysis that was done with cosmic muon runs consisted of evaluating the number of jets reconstructed in each event of the run and the distribution of those jets in transverse energy (E_t) and across the detector (η and ϕ distributions). For run 90272, the results obtained are presented in figures 4.2, 4.4, 4.5 and 4.6.

Looking at figure 4.2, one can see that most of the reconstructed events, by both the trigger and offline, have either one or no jets. Figures 4.2(a) and 4.2(b), in particular, indicate that LVL1 and LVL2 identify approximately the same number of jets. This was expected, since, as mentioned previously, LVL1 produces one RoI per jet candidate identified and LVL2 receives the RoI information from LVL1, reconstructing one jet per RoI. The exception occurs in the forward region of the detector ($|\eta| > 3.2$), as shown in figure 4.3, where the (η, ϕ) coordinates of LVL1 jets that were not identified by LVL2 are plotted. The reason for this is that, when this cosmic muon run was taken, the HLT was not running in the forward region of the detector.

Finally, figure 4.2 also shows that as one moves to EF and offline reconstruction, more events with none, two and three jets appear, whereas the number of single-jet events decreases. Because the logarithmic scale might be misleading, it is important to note that offline and EF actually recon-

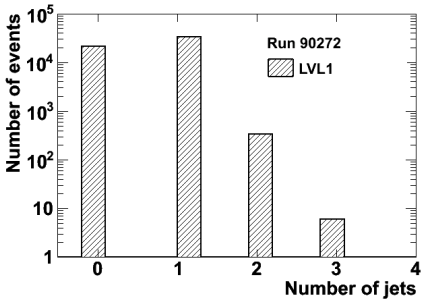

(a) Level 1 jets.

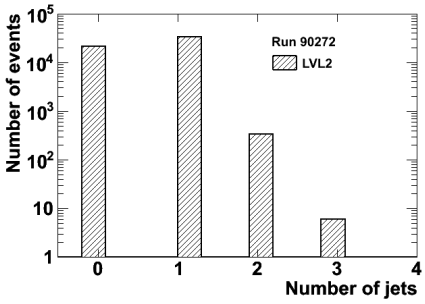

(b) Level 2 jets.

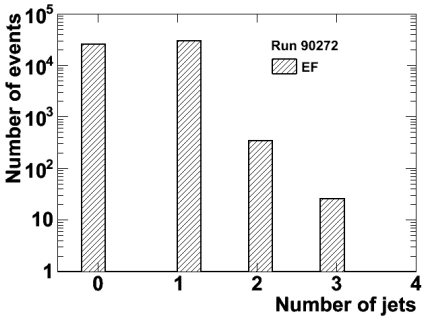

(c) Event Filter jets.

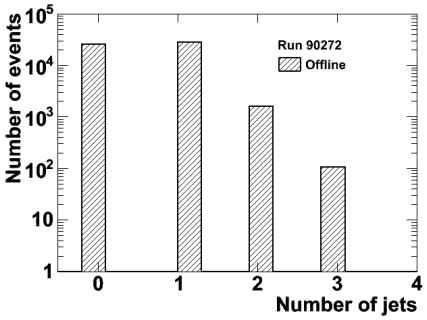

(d) Offline reconstructed jets.

Figure 4.2: Number of jets distribution of events from cosmic muon run 90272.

struct, on average, less jets per event than LVL1 and LVL2, EF being the one that reconstructs, on average, less jets. Also, it was verified that this behavior is not specific of this particular run but rather common to all the reprocessed runs analyzed. Most likely, this is the case of low E_t jets, that passed the LVL1 and LVL2 thresholds and were reconstructed in these levels, but did not pass the EF thresholds and were not seen by this trigger level.

Looking now at the transverse energy distributions (figure 4.4), they show the expected exponential shape. This shape is related to the way the cross-section for jet production decreases as the transverse energy increases, indicating that it is much more likely that low-E_t jets are produced when compared to high-E_t jets. The distributions also show that the energy deposited by cosmic muons in the ATLAS calorimeters during this run ranges

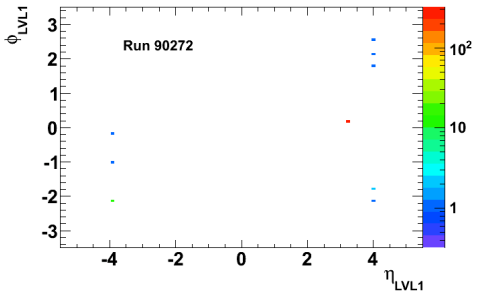

Figure 4.3: (η, ϕ) map of LVL1 jets in events from cosmic muon run 90272 where the number of LVL1 jets is different from the number of LVL2 jets.

from $\approx$ 0GeV to $\approx$ 300GeV.

Some information about the calibration of jet energy can be taken from this set of distributions as well. Starting with figure 4.4(b), one can see that calibration at LVL2 is only done for jets with $E_t > 20$GeV, a behavior that was corrected for subsequent runs. Furthermore, this distribution shows that the effect of the calibration applied is the displacement of the distribution towards higher E_t. This happens because, as explained in section 1.2.3.2, the uncalibrated (EM-scale) jet energy is underestimated due to non-compensation and other detector effects, and can be seen by looking at the displaced peak at low E_t. Taking this into account and looking at figure 4.4(c), one can see that the transverse energy plotted for EF is already calibrated, since the peak is slightly displaced to the right when compared to the peaks in LVL1 or LVL2 before calibration. Similarly, figure 4.4(d) seems to indicate that the offline reconstructed E_t of the jets was not calibrated.

The η distribution of the jets (figure 4.5) shows they are mostly found in the central region of the detector, mimicking the expected distribution for QCD events (section 5.2). Comparing figures 4.5(a), 4.5(b) and 4.5(c), one can see that, indeed, the HLT was not running in the forward region of the detector, since no LVL2 or EF jets appear for $|\eta| > 3.2$. LVL1, on the contrary, shows counts on the forward region. However (see section 3.2.1), for negative values of η, jets appear only at $\eta \approx -4$, whereas for positive η one has LVL1 jets at $\eta \approx 3.3$ and $\eta \approx 4$. It is important to state that this behavior is a reflex of the fact that the trigger towers in the forward calorimeters have only one η bin in the backward region and two in the

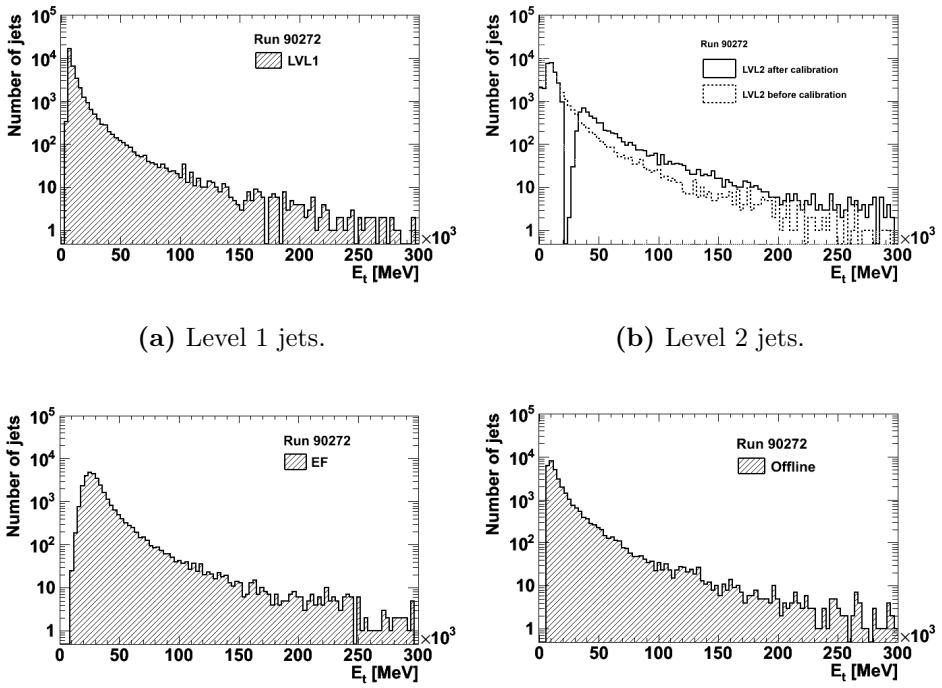

(a) Level 1 jets.

(b) Level 2 jets.

(c) Event Filter jets.

(d) Offline reconstructed jets.

Figure 4.4: Transverse energy distribution of the jets from cosmic muon run 90272.

forward region. This means that all LVL1 jets in the forward region, whose η coordinates can span $3.2 < |\eta| < 5$, will always have the coordinates of the forward bins.

Still concerning LVL1 jets, the distribution in figure 4.5(a) clearly shows that LVL1 algorithms use a calorimeter granularity of 0.2×0.2 in $\Delta\eta \times \Delta\phi$, as previously explained in section 3.2.1, whereas the other trigger levels, as well as offline, use the full calorimeter granularity. This is why the η distribution for LVL1 (figure 4.5(a)) is discrete, each bin having a width of 0.2, a feature also visible in the ϕ distribution for LVL1 (figure 4.6(a)).

One final remark on the η distributions in figure 4.5: there are some η positions where the jet count spikes. For now, those positions will only be registered in table 4.2, since a separate chapter is devoted to explaining their reason and importance. Moreover, and taking into account the behavior of the LVL1 trigger in the forward calorimeters, it is very likely that the peaks

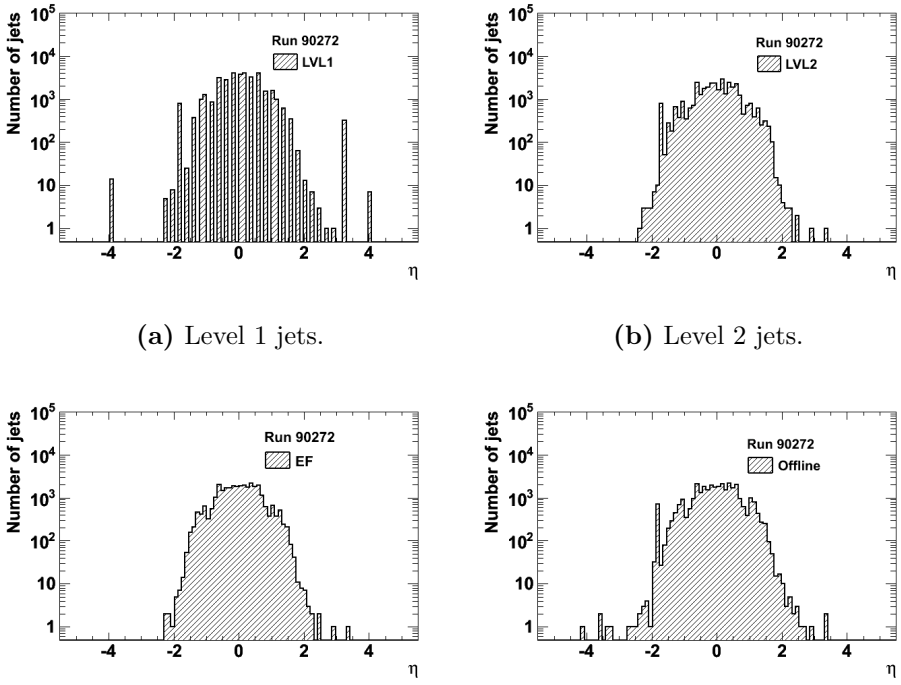

(a) Level 1 jets.

(b) Level 2 jets.

(c) Event Filter jets.

(d) Offline reconstructed jets.

Figure 4.5: η distribution of the jets from cosmic muon run 90272.

in the forward region visible in figure 4.5(a) are due to the reduced amount of bins, rather than to an actual spike in the jet count at those particular η positions. The idea is reenforced by looking at figure 4.5(d), where offline forward jets do not have a fixed position and there are no visible peaks in the forward region. Nevertheless, these LVL1 coordinates were still registered as peaks.

Finally, the flatness in the ϕ distributions (figure 4.6) indicates that, as it is already known, the calorimeters have azimuthal uniformity (section 2.2.1.3). Nonetheless, similarly to what was seen in the η distributions (figure 4.5), some of the ϕ distributions present peaks. Their positions are registered in Table 4.2 and an explanation will be presented in a different chapter ahead.

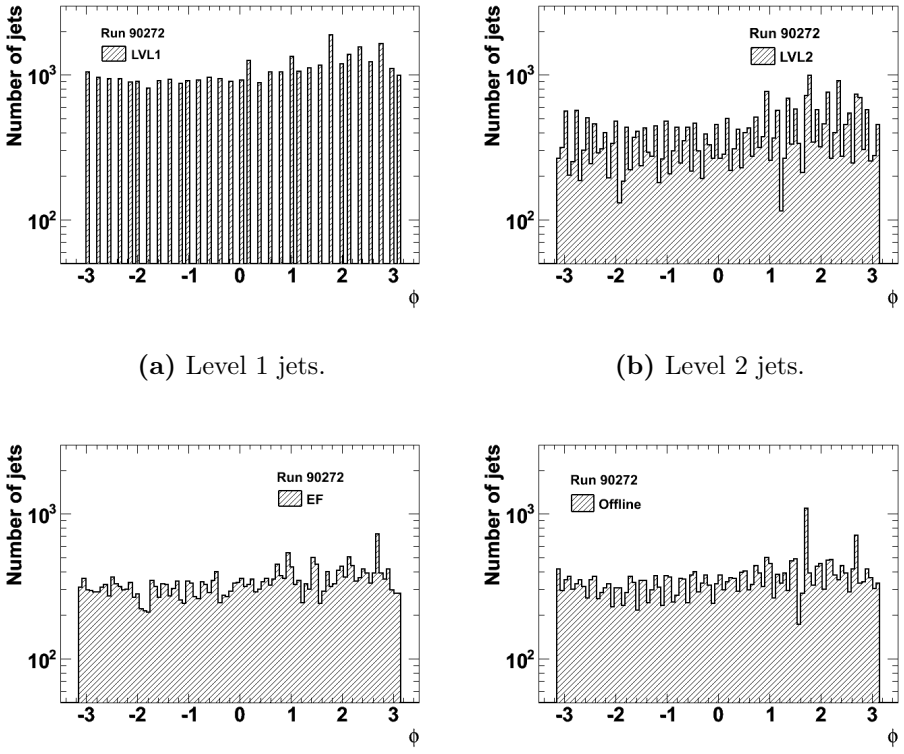

(a) Level 1 jets.

(b) Level 2 jets.

(c) Event Filter jets.

(d) Offline reconstructed jets.

Figure 4.6: ϕ distribution of the jets from cosmic muon run 90272.

4.3.2 Noisy Cell Identification

After the initial assembly of the ATLAS calorimeters, less than one per mill cells presented elevated noise level [54, 55], i.e., presented high rates, well above the average signal level of all the calorimeter cells, even when no particles interacted with them. These high rates can fire any of the trigger levels or offline reconstruction algorithms, blocking the real physics search [56]. In other words, when the trigger and offline reconstruction algorithms search for jet candidates in the detector, the search can be highly biased by these noisy cells with a large number of events, leading to a poor reconstruction of the jet position and energy. Thus, noisy calorimeter cells can greatly affect the performance of the jet trigger and offline reconstruction, even in such a small number.

Run 90272				
	LVL1	*LVL2*	*EF*	*Offline*
η	-3.9 -1.8 3.2 4.0	-1.8	none	-1.8
ϕ	none	none	2.7	2.7 1.8

Table 4.2: Approximate position of the peaks seen in the η and ϕ distributions of jets from cosmic muon run 90272.

The problem presented by noisy cells can be remedied with masking. When calorimeter cells are masked their signal is set to zero. This way, no energy is reconstructed from these cells and they do not interfere with the ATLAS reconstruction algorithms. Masking, however, must be done carefully, since when applied to cells that are signaling properly, it can lead to loss of important data. Cosmic muon runs become useful, once again, as they can help identify noisy cells and apply proper masking.

Basically, figure 4.7 maps the positions of jets in the detector (according to their η and ϕ coordinates). The figure seems to indicate that the jets identified by the trigger and offline analysis are distributed evenly throughout the detector, except for a few positions where the jet count spikes. The coordinates of those positions are registered in Table 4.3 and one can see that some of them appear in all three trigger maps (figures 4.7(a), 4.7(b) and 4.7(c)) and also in the offline map (figure 4.7(d)) These positions are noisy cells, as they signal a much higher number of jets than the surrounding ones.

Some of these noisy cells have already been identified before. Looking at Table 4.2, one can verify that the positions of the peaks seen in the η and ϕ distributions of the jets (figures 4.5 and 4.6) match some of the coordinates of the noisy cells identified with the (η, ϕ) maps of the jets (figure 4.7). This means that noisy cells can also be identified by looking for peaks in η and ϕ distributions. However, this kind of analysis was done with several cosmic muon runs and it was found that (η, ϕ) maps are the best way to identify

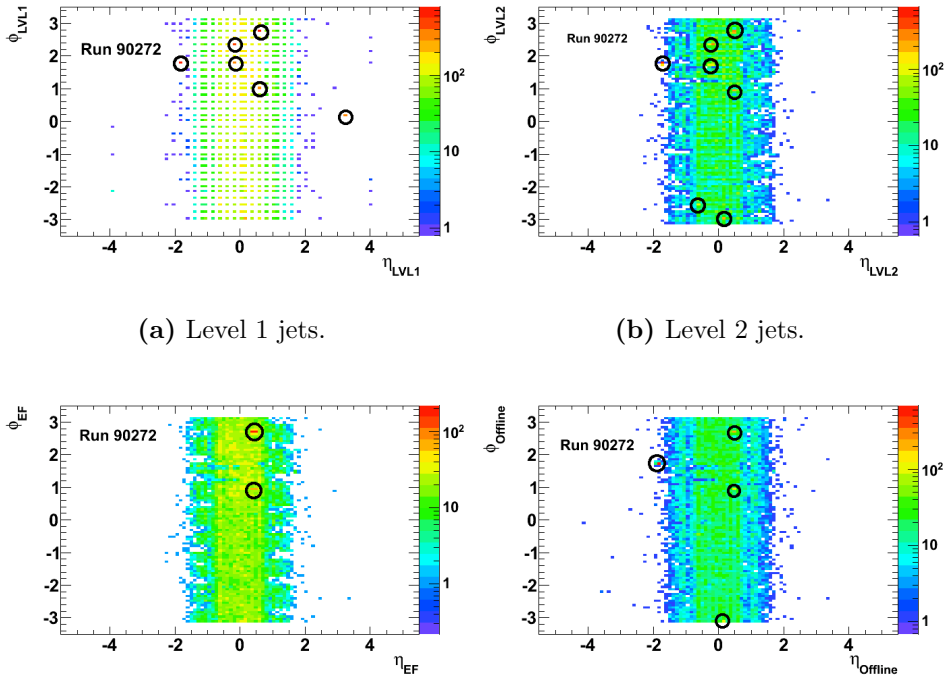

(a) Level 1 jets. **(b)** Level 2 jets.

(c) Event Filter jets. **(d)** Offline reconstructed jets.

Figure 4.7: (η, ϕ) map of jets from cosmic muon run 90272.

noisy cells. Because they are a conjugation of both η and ϕ distributions, not only do they flag more noisy cells than the separate distributions, but they also give the whole coordinate of the noisy cell (using the η and ϕ distributions separately one cannot know which η position corresponds to a given ϕ position).

At this point, it is important to note that the (η, ϕ) maps do not flag every noisy cell in the ATLAS calorimeters. This method allows the identification of the clearest noisy cells, meaning there might be cells with low noise levels that are not tagged and require other analysis procedures. Nonetheless, calorimeter cells with high noise levels are the ones that affect the trigger performance the most.

The analysis of several cosmic muon runs also revealed that the pattern of noisy cells is, at times, repetitive, meaning that some cells were identified as noisy not just in a particular run but in several. This kind of information is important to ensure an even more effective masking, as it guarantees that

Run 90272				
	LVL1	*LVL2*	*EF*	*Offline*
(η, ϕ)	$(0.5, 2.7)$ $(-0.2, 2.3)$ $(-1.8, 1.8)$ $(-0.2, 1.8)$ $(0.5, 1.0)$ $(3.2, 0.2)$	$(0.5, 2.7)$ $(-0.2, 2.3)$ $(-1.8, 1.8)$ $(-0.2, 1.8)$ $(0.5, 1.0)$ $(-0.6, -2.5)$ $(0.1, -3.0)$	$(0.5, 2.7)$ $(0.5, 1.0)$	$(0.5, 2.7)$ $(-1.8, 1.8)$ $(0.5, 1.0)$ $(0.1, -3.0)$

Table 4.3: Approximate coordinates of the noisy cells seen in the (η, ϕ) maps of jets from cosmic muon run 90272.

cells identified as noisy are indeed malfunctioning cells and not just cells that did not signal properly during a particular run.

Looking, once again, at the (η, ϕ) maps (figure 4.7) one can verify that some cells have the η coordinate in common. Since the definition of a trigger tower is a set of cells summed along η, this kind of behavior could indicate that the entire tower is noisy and not just a few cells. Also, these distributions show the importance of an effective masking. Even though EF (figure 4.7(c)) reconstructs less jets from noisy cells than the previous trigger levels (figures 4.7(a) and 4.7(b)), these cells still affect the offline reconstruction as one can see from figure 4.7(d).

4.4 Evaluation of the Trigger Reconstruction

4.4.1 Noisy Cell Removal

It was seen in a previous section that cosmic muon runs allow the identification of noisy cells. It was also stated that these noisy cells could influence the trigger and offline reconstruction. Thus, to perform an accurate assessment of the trigger reconstruction, jets reconstructed from noisy cells cannot be considered. In other words, noisy cells have to be removed before the trigger is evaluated.

The removal of jets reconstructed by noisy cells was done using the (η, ϕ) maps in figure 4.7 and "rectangular" cuts in η and ϕ. Take, for example,

figure 4.7(a) and Table 4.3, which tells us that LVL1 identified a noisy cell at the position $(0.5, 2.7)$. To remove LVL1 jets reconstructed from that noisy cell, one eliminates all LVL1 jets whose position in the detector is $(0.5 \pm \delta, 2.7 \pm \delta)$ where δ is typically of the order of 0.1. The procedure is similar for the other trigger levels and for offline jets. Table 4.4 summarizes the effect of the cuts on the number of jets. Approximately, each cut removed 1% of initial number of jets.

Run 90272				
	LVL1	*LVL2*	*EF*	*Offline*
Total number of jets	34643	34304	30193	31842
Number of removed jets	2869	2653	647	1305
Number of remaining jets	31774	31651	29546	30537

Table 4.4: Change in number of trigger and offline jets from cosmic muon run 90272 after noisy cell removal.

Figure 4.8 is similar to figure 4.7, since it maps the position of trigger and offline jets in the detector once those originating from noisy cells (table 4.3) were removed. One can see that, after the removal of noisy cells, the distribution of jets in the detector is more uniform. Furthermore, no particular region seems to indicate a spike on the jet count that is inconsistent with the number of jets identified in the neighboring cells. So, in principle, all the remaining jets in the maps were built from functioning calorimeter cells and can be used to evaluate trigger performance.

To further investigate the subject of noisy cells, the transverse energy distributions of jets reconstructed from noisy cells were plotted and are shown in figure 4.9. The figure shows that most of the trigger jets reconstructed from noisy cells (figures 4.9(a), 4.9(b) and 4.9(c)) have low transverse energies (smaller than $\approx$ 20GeV). It is, thus, possible that, in case the HLT were actually eliminating events and not just running in pass-through mode, as it is here and will be during the first period of data taking, some of these jets would not reach the offline analysis. Nevertheless, since one does not have that information, figure 4.9 shows how jets from noisy cells are passed from the trigger to offline analysis and, in this case, reconstructed by offline with significant transverse energy: figure 4.9(d) shows a peak of offline jets

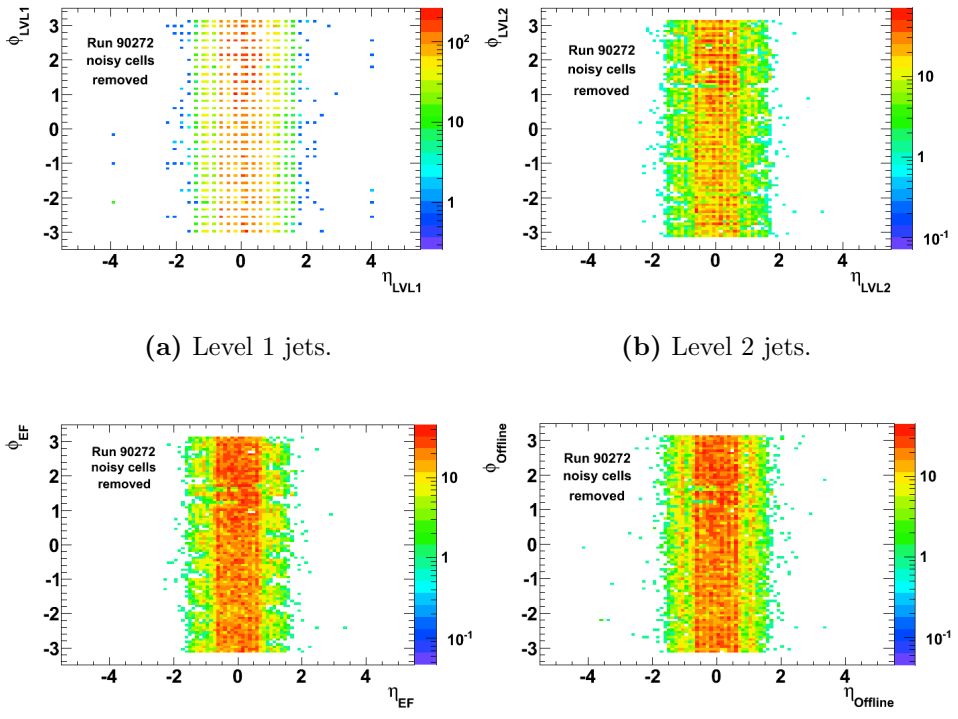

(a) Level 1 jets.

(b) Level 2 jets.

(c) Event Filter jets.

(d) Offline reconstructed jets.

Figure 4.8: (η, ϕ) map of jets from cosmic muon run 90272 after noisy cell removal.

reconstructed from noisy cells with $\approx$ 100GeV$< E_t <$ 140GeV.

4.4.2 Matching Trigger Jets Offline

The evaluation of the quality of a jet reconstruction is done by comparing the properties of the reconstructed jets to the properties of the reference to those jets, which is the primary partons that suffered hadronization. However, the properties of the parton can only be obtained directly with MonteCarlo simulated data. With real data, the jets are reconstructed and calibrations are applied to try to bring them to the parton level (sections 1.2.3.2 and 3.1.2). In other words, with real data, offline reconstructed jets are the closest to the parton reference. Thus, the evaluation of quality of the jet trigger reconstruction will be done by comparing trigger jets to offline jets.

The first step to do so is to match the trigger and offline reconstructed

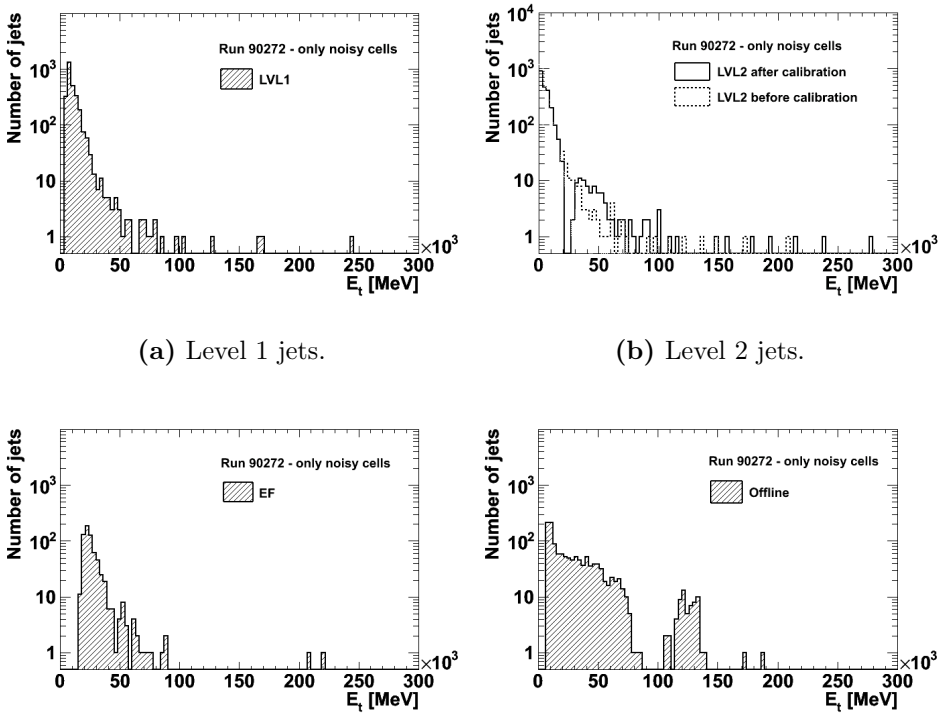

(a) Level 1 jets.

(b) Level 2 jets.

(c) Event Filter jets.

(d) Offline reconstructed jets.

Figure 4.9: Transverse energy distribution of the jets from cosmic muon run 90272 reconstructed from noisy cells.

jets in each event. This means making sure that one particular trigger jet is compared to the same jet reconstructed offline. In other words, making sure that the trigger and offline jet are the result of the reconstruction of the same object, which is, in this case, a muon and not a parton. The matching is done according to the position of the jets, i.e., in an event, a trigger jet is matched to a particular offline jet if, of all the trigger jets in that event, it is the closest to the offline jet, in the (η, ϕ)-space of the detector.

The process of matching trigger jets (trigger jets being LVL1 jets, LVL2 jets or EF jets) to offline jets is depicted in figure 4.10 and described next:

1. The process begins with taking an event and choosing one offline reconstructed jet from that event. The coordinates of that jet are $\eta_{Offline}$ and $\phi_{Offline}$.

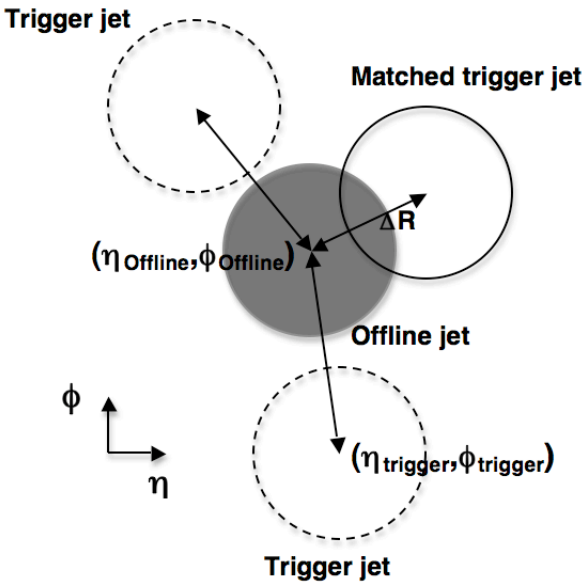

Figure 4.10: Scheme of the matching process between trigger and offline jets in one event.

2. The quantity
$$\Delta R = \sqrt{(\Delta\eta)^2 - (\Delta\phi)^2}$$
with
$$\Delta\eta = \eta_{trigger} - \eta_{Offline}$$
and
$$\Delta\phi = \phi_{trigger} - \phi_{Offline}$$
is calculated between the chosen offline jet and every trigger jet in the event.

3. The trigger jet with the smallest ΔR is matched to the offline jet as schemed in figure 4.10. Since ΔR represents a distance in the (η, ϕ)-space, choosing the smallest ΔR means choosing the closest jet.

4. Finally, another offline jet is chosen from that event and the process is repeated. This means that this second offline jet is compared to every trigger jet in the event, including the one that was previously matched, so another match can be done.

Given the way the matching process is done, the same trigger jet can be matched to several offline jets in the event. One can imagine a case where

LVL1 merged two close jets and identified them as only one RoI, whereas offline's more sophisticated algorithms were able to differentiate them. This matching process continues until all offline jets in the event are matched to one trigger jet. Afterwards, the process is repeated for another event until all events are analyzed.

Once the jets are matched, a first analysis can be done to evaluate the quality of the reconstruction of the jets positions, by looking at the ΔR distributions of the matched jets, which are presented in figure 4.11. Because jets were matched according to their positions, the distributions peak at zero as expected, indicating that most of the trigger jets are close (small ΔR) to the matched offline jets. In other words, trigger and offline reconstruct jets approximately in the same position.

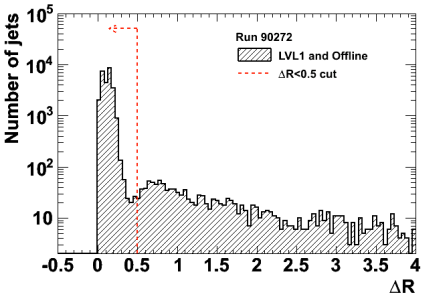

(a) Matched LVL1 and offline jets.

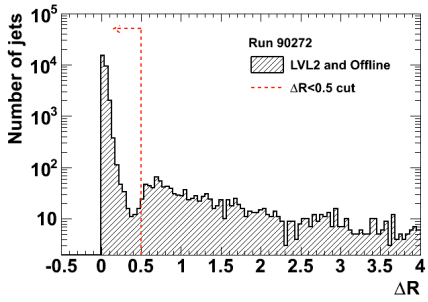

(b) Matched LVL2 and offline jets.

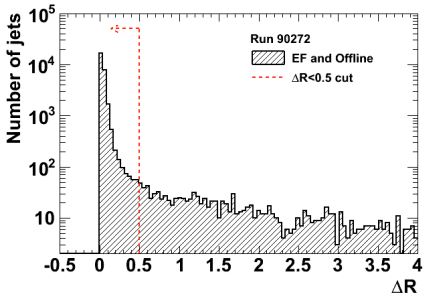

(c) Matched EF and offline jets.

Figure 4.11: ΔR distribution of matched trigger and offline jets from cosmic muon run 90272.

Nevertheless, figure 4.11 shows a large "tail" after the peak, suggest-

ing that some of the trigger jets are still very distanced from their offline matches. These actually correspond to offline jets that were not identified by the trigger. So this matching process pairs jets with $\Delta R > 0.8$ (or $\Delta R > 1.1$ is the case of EF and offline matched jets), which means they do not even overlap. To overcome this, a cut in ΔR is applied: only matched trigger and offline jets with $\Delta R < 0.5$ are used. This cut is represented in the distributions with a dotted line) and ensures that the maximum distance, in the (η, ϕ)-space, between the center of the matched jets is 0.5, which means that they always overlap. By doing this, one guarantees proper matching between jets which will be crucial to further evaluate trigger reconstruction.

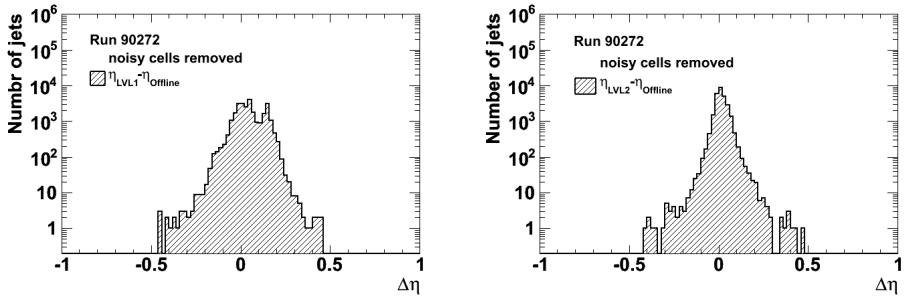

(a) Matched LVL1 and offline jets.

(b) Matched LVL2 and offline jets.

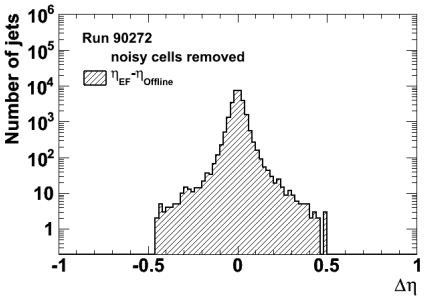

(c) Matched EF and offline jets.

Figure 4.12: $\Delta\eta$ distribution of matched trigger and offline jets from cosmic muon run 90272 after noisy cell removal.

After ensuring that matched jets overlap in the (η, ϕ)-space, another analysis can be done to evaluate the quality of the reconstruction of the jets' positions by looking at the $\Delta\eta$ and $\Delta\phi$ distributions of the matched

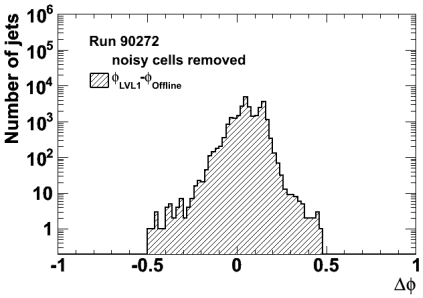

(a) Matched LVL1 and offline jets.

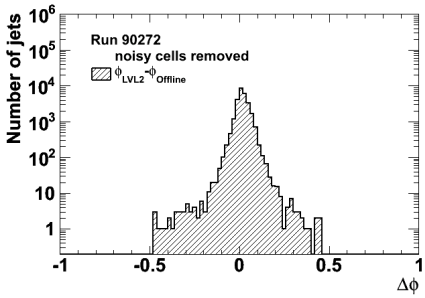

(b) Matched LVL2 and offline jets.

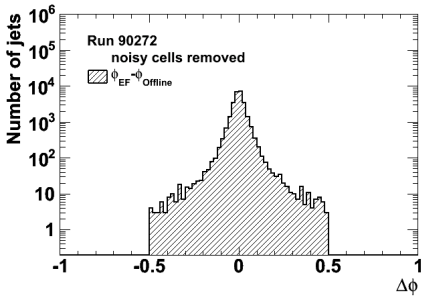

(c) Matched EF and offline jets.

Figure 4.13: $\Delta\phi$ distribution of matched trigger and offline jets from cosmic muon run 90272.

jets. Once again, because jets were matched according to their positions and given the cuts applied to ΔR, one would expect the distributions to peak at zero, as shown in figures 4.12 and 4.13.

Since LVL1 performs the first and simplest reconstruction, one also expects LVL1 reconstruction to differ the most from offline reconstruction. Indeed, LVL1 and offline matched jets (figures 4.12(a) and 4.13(a)) have broader distributions than LVL2 and offline (figures 4.12(b) and 4.13(b)) or EF and offline matched jets (figures 4.12(c) and 4.13(c)). LVL2 and EF, on the other hand, perform very similar reconstructions.

Another detail from these distributions, concerning LVL1 reconstruction, is the second peak visible in both $\Delta\eta$ and $\Delta\phi$ distributions (figures 4.12(a) and 4.13(a)), at ≈ 0.15. The reason for this second peak has not yet been confirmed, but the most probable explanation [57] is related to the differ-

ence in LVL1 and offline granularities. Let us assume that in a reasonable number of cases, because cosmic muons are being addressed, the energy is mostly deposited in only one calorimeter cell, with only a few small energy depositions around that most energetic cell with. As an example, suppose that cell has $\eta = 0.15$. Since most of the energy is deposited there it is likely that $\eta_{Offline} \approx 0.05$. As for the LVL1, one will most likely have $\eta_{LVL1} = 0.1$. Nonetheless, it can happen that a small asymmetry in the energy deposition (caused by the smaller depositions around the primary cell) might lead LVL1 to identify the next jet element, that has $\eta_{LVL1} = 0.3$, since LVL1 has a 0.2 granularity. In that case, one will have $\Delta\eta \approx 0.15$, hence the second peak in the distribution. The same reasoning can be applied to the $\Delta\phi$ distribution.

4.4.3 Matching Trigger Jets Online

Several distributions were presented in the previous sections of this chapter. The purpose was to evaluate the quality of the data and assess the trigger performance. This is was done mostly by comparing the trigger reconstruction with the offline reconstruction. Suppose, however, that the offline reconstruction of the jets is not available, like during the online monitoring of the runs. Even in this situation, one should be able to monitor the quality of the data delivered by the trigger system. Next to offline, EF performs the best reconstruction of jets. Thus, if no offline reconstructed jets are available, the comparison is done between LVL1 and EF jets and LVL2 and EF jets.

Once again, comparing jets requires matching first. Hence, matching LVL1 or LVL2 jets to EF jets is necessary. The process for doing so is different than the one described before for matching trigger to offline jets, because, when it comes to the jet trigger, each reconstruction is seeded by a reconstruction done in the previous level. Thus, matching simply consists of only selecting events that have one LVL1 jet, one LVL2 jet and one EF jet. This way, analyzing each event separately also means looking at the same jet reconstructed by the different trigger levels. Finally, the evaluation of the reconstruction quality is done similarly to what was done with offline matching, i.e., by looking at the $\Delta\eta$, $\Delta\phi$ and ΔR distributions.

The $\Delta\eta$ and $\Delta\phi$ distributions are shown in figures 4.14 and 4.15. As expected, these distributions peak at zero and are larger for LVL1 and EF

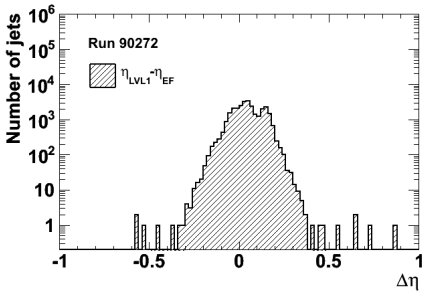

(a) Matched LVL1 and EF jets.

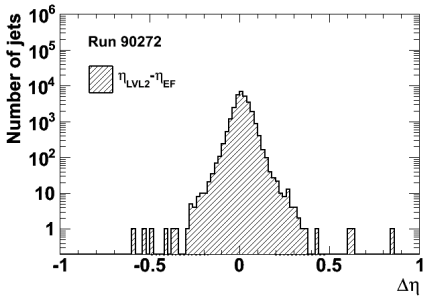

(b) Matched LVL2 and EF jets.

Figure 4.14: $\Delta\eta$ distribution of matched LVL1/LVL2 and EF jets from cosmic muon run 90272.

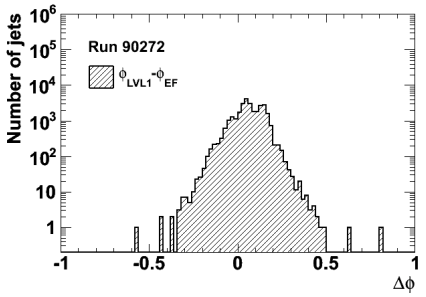

(a) Matched LVL1 and EF jets.

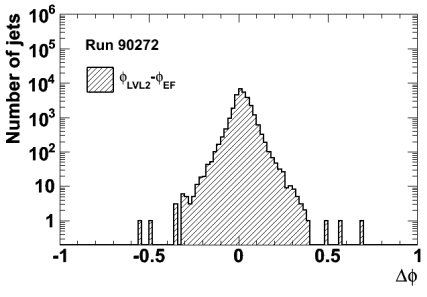

(b) Matched LVL2 and EF jets.

Figure 4.15: $\Delta\phi$ distribution of matched LVL1/LVL2 and EF jets from cosmic muon run 90272.

matched jet than for LVL2 and EF matched jets. Once again, LVL1's coarse identification algorithms lead to worst reconstruction when compared to LVL2, whose more sophisticated algorithms reconstruct jets more similar to EF.

Also, the "second peaks" previously seen in LVL1 and offline matched jets distributions (figures 4.12(a) and 4.13(a)) are also visible for these distributions of matched LVL1 and EF jets, although not as pronounced. Considering the possible explanation presented in the previous section and since LVL1 and EF have different granularities, this behavior is expected.

Finally, the ΔR distributions for LVL1 and LVL2 jets matched to EF

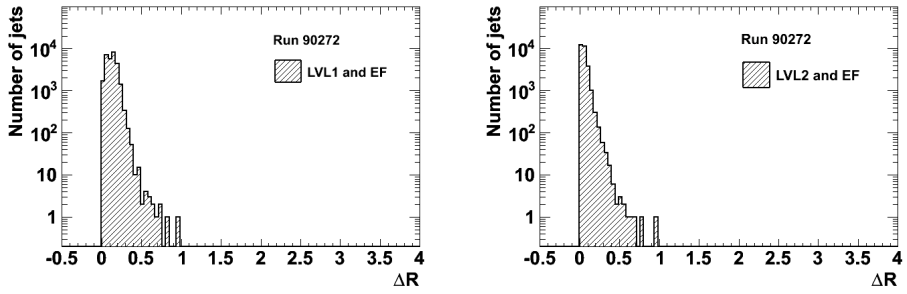

(a) Matched LVL1 and EF jets. **(b)** Matched LVL2 and EF jets.

Figure 4.16: ΔR distribution of matched LVL1/LVL2 and EF jets from cosmic muon run 90272.

jets, presented in figure 4.16 indicate that both LVL1 and LVL2 jets overlap with their paired EF jets, i.e., all pairs have $\Delta R < 1.1$. Thus, like before, one has properly matched jets which allows further analysis.

4.4.4 Energy Reconstruction - Comparison to Offline

After matching between trigger and offline jets is performed, one can analyze reconstruction on an energy level. One way to do so is to map the trigger and offline matched jets according to their transverse energies, $(E_t^{Offline}, E_t^{trigger})$. This kind of maps allow us to verify if there is a correlation between both energy reconstructions.

Looking first at figure 4.17(a), one can see that most matched LVL1 and offline jets fall within a "line" where $E_t^{LVL1} \approx E_t^{Offline}$. This is important, not only because it certifies that LVL1 and offline reconstruct similar transverse energies for jets, but also because it shows the correlation in the reconstruction.

Still, there are some jets whose transverse energy is reconstructed very differently by LVL1 and offline. In particular, most of them have $E_t^{LVL1} < E_t^{Offline}$, as they are below the "correlation line". This behavior is comparable to the broad $\Delta\eta$ and $\Delta\phi$ distributions seen before for LVL1 and offline matched jets and presented in figures 4.12(a) and 4.13(a). In other words, because LVL1 algorithms are so rudimentary, it can identify jets very different from offline, both in position and transverse energy.

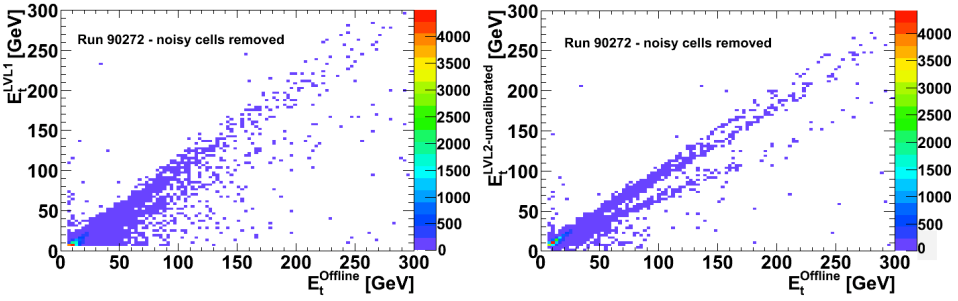

(a) Matched LVL1 and offline jets.

(b) Matched LVL2 and offline jets.

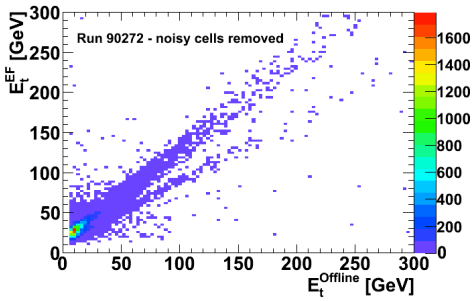

(c) Matched EF and offline jets.

Figure 4.17: $(E_t^{Offline}, E_t^{trigger})$ map of jets from cosmic muon run 90272 after noisy cell removal.

Following this train of thought and considering what was seen in the $\Delta\eta$ and $\Delta\phi$ distributions for LVL2 and EF jets matched to offline jets (figures 4.12(b), 4.13(b), 4.12(c) and 4.13(c)), one would expect LVL2 and EF to improve the reconstruction of E_t performed by LVL1, showing less jets outside the "line". This is exactly what figures 4.17(b) and 4.17(c) show. Both LVL2 and EF improve LVL1's reconstruction showing similar behavior to offline.

Now, looking at LVL2 and offline matched jets in particular (figure 4.17(b)), it is important to state that uncalibrated LVL2 jets were chosen to be compared to offline jets, because these are also not calibrated. Also, this plot shows a behavior that was not clear for LVL1 and offline matched jets. Although most matched jets fall in a "line" where $E_t^{LVL2} \approx E_t^{Offline}$, there is still a significant amount of them that form a second "line" below the

first one, where $E_t^{LVL2} \lesssim E_t^{Offline}$. The first "line" tells us that, in most cases, LVL2 and offline reconstruct very similar E_t values, but the second one indicates that LVL2 reconstruction is correlated to offline reconstruction in two different ways.

This was further investigated [57] and it was found that jets in the first "line" are located in the TileCal's barrel, while the ones in the second "line" are in TileCal's extended barrel. It was later understood that a calibration error in the TileCal was causing offline to reconstruct jets in the extended barrel with lower E_t than jets in the barrel. It is, however, important to note that the error was repaired and that this effect is no longer visible in more recent cosmic runs.

The distribution for EF and offline matched jets (figure 4.17(c)) confirms what was seen before, indicating that transverse energies reconstructed by the trigger are correlated to offline's reconstruction in two different ways (there are at least two clear diagonals in the distribution). As for the values of the reconstructed E_t, they will not be analyzed using this distribution, since jets are being compared at different scales: EF jets are calibrated and offline jets are not calibrated.

Another way to evaluate energy reconstruction is to evaluate the stability of the transverse energy ratio

$$E_t^{ratio} = \frac{E_t^{trigger}}{E_t^{Offline}}$$

as a function of $E_t^{Offline}$ and $\eta_{Offline}$. Basically, if one considers the "lines" seen in the previous plots (figure 4.17) have an "average slope", one will be looking at the value of that slope as a function of E_t and η. It is possible to evaluate, this way, how the reconstruction changes for different jet energies and different regions of the detector. Remember that the previous distributions showed that offline jets reconstructed in the extended barrel had lower energies than offline jets reconstructed in the barrel.

Figure 4.18 shows a profile plot of the E_t^{ratio} between trigger and offline matched jets as a function of the transverse energy of the offline jets. For each $E_t^{Offline}$ bin, whose width is indicated by the horizontal error bars, the mean value of the E_t^{ratio} distribution is plotted, with the vertical error bars indicating the RMS value of the E_t^{ratio} distribution for that bin. This is

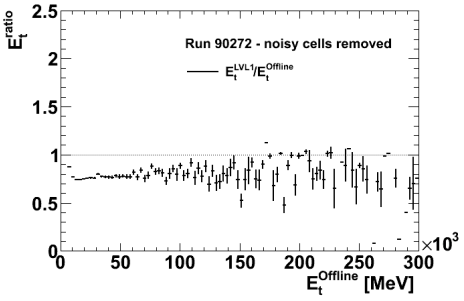

(a) Matched LVL1 and offline jets.

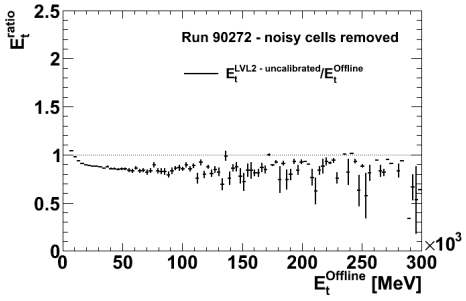

(b) Matched LVL2 and offline jets.

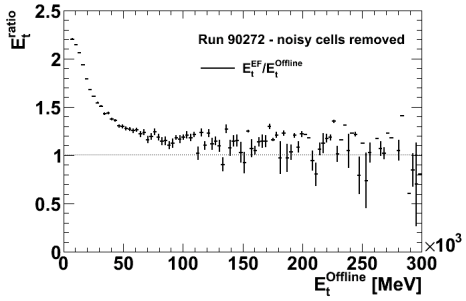

(c) Matched EF and offline jets.

Figure 4.18: E_t^{ratio} between trigger and offline matched jets as a function of $E_t^{Offline}$ for cosmic muon run 90272 after noisy cell removal.

similar for the profile plots show in figure 4.19, only $\eta_{Offline}$ bins are used instead.

Comparing both figures 4.18 and 4.19, one can see that the transverse energy ratio is approximately flat across the considered $E_t^{Offline}$ range but shows large variations across $\eta_{Offline}$. These variations are similar for all three trigger levels and confirm that offline does reconstruct transverse energies differently in the barrel and in the extended barrel.

In particular, E_t^{ratio} is flat and stable in the barrel ($|\eta| < 1$), but not in the extended barrel ($1 < |\eta| < 1.5$), where some fluctuations are visible. Also, one can see that the E_t^{ratio} in the extended barrel is smaller than in the barrel, which confirms the information taken from the E_t maps in figure 4.17, where the second "line" was below the first "line". Finally, the transverse energy ratio shows the largest fluctuations for jets in the endcaps

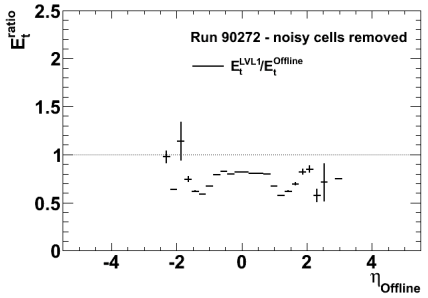

(a) Matched LVL1 and offline jets.

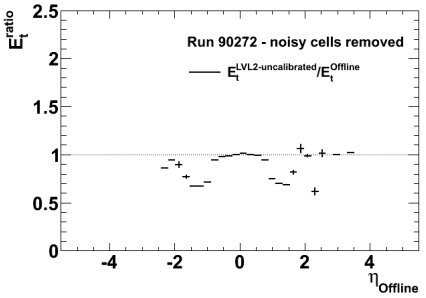

(b) Matched LVL2 and offline jets.

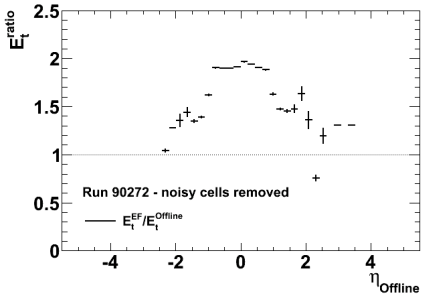

(c) Matched EF and offline jets.

Figure 4.19: E_t^{ratio} between trigger and offline matched jets as a function of $\eta_{Offline}$ for cosmic muon run 90272 after noisy cell removal.

and forward detectors ($|\eta| > 1.5$). It is, however, important to note that statistics are low in the endcap and forward regions of the detector, as one can see by the large error bars, which could account for the large fluctuations.

Looking more closely now at the profile plot in figure 4.18(a), one can see that LVL1 reconstructs energy at $\approx 75\%$ when compared to offline reconstruction. LVL2 (figure 4.18(b)), on the other hand, reconstructs energy closer to offline ($\approx 85\%$) and appears to have a more stable transverse energy ratio across the whole $E_t^{Offline}$ range. Finally, looking at EF reconstruction, and even though not many conclusions can be drawn since two different scales are being compared, one can still see that EF calibration overestimates offline energy reconstruction for jets with $E_t^{Offline} \lesssim 50$GeV.

Considering the two different calibrations in the TileCal, it is important to mention that the percentages given for the E_t^{ratio} actually represent an

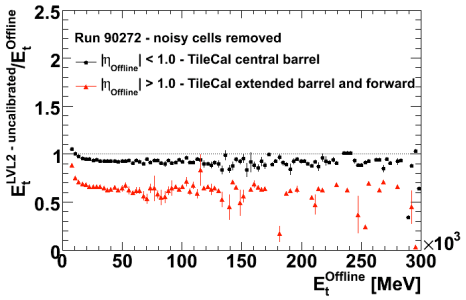

Figure 4.20: E_t^{ratio}, in two $\eta_{Offline}$ bins, between LVL2 and offline matched jets as a function of $E_t^{Offline}$ for cosmic muon run 90272 after noisy cell removal.

"average" of two different E_t^{ratio} in two different η regions. This fact becomes clearer by looking at figure 4.20, where the E_t^{ratio} between LVL2 and offline matched jets is evaluated in two different η regions as a function of $E_t^{Offline}$. The η regions chosen correspond to the TileCal's central barrel and TileCal's extended barrel and forward. The figure shows that, indeed, the TileCal's barrel was calibrated correctly, as figure 4.19(b) had already suggested. The transverse energy ratio is flat and stable across the full $E_t^{Offline}$ range and indicates that, in the central barrel, LVL2 reconstructs the transverse energy at $\approx 95\%$ when compared to offline. As for the rest of the calorimeter, E_t^{ratio} is at $\approx 65\%$ showing some fluctuations.

4.4.5 Energy Reconstruction - Comparison to EF

It was described in the previous section that the process of matching jets could also be done between LVL1 or LVL2 jets and EF jets. When this kind of matching is performed, the evaluation of the energy reconstruction is done as shown in the section 4.4.4, only offline jets are replaced by EF jets. Thus, the plots obtained from LVL1 or LVL2 and EF matched jets are presented next.

Starting with figure 4.21, the first thing worth mentioning is that, for both LVL1 (figure 4.21(a)) and LVL2 (figure 4.21(b)), jets fall in a single "line" and no other "correlation lines" are visible, contrary to what was seen when matching to offline jets was done. It was discussed that the multiple "lines" were a result of the offline reconstruction performing differently in different regions of the TileCal. In particular, this was due to an error in

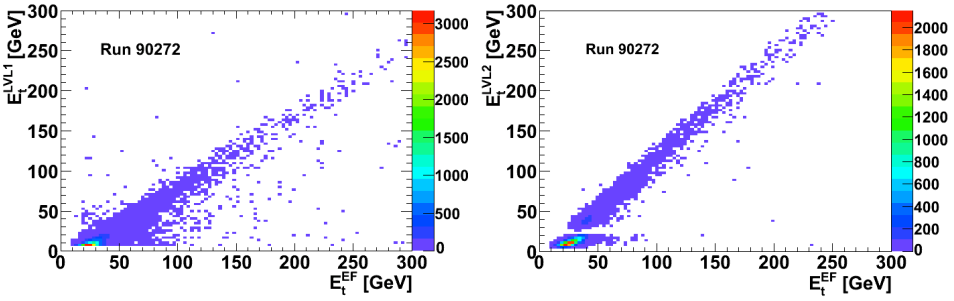

(a) Matched LVL1 and EF jets. **(b)** Matched LVL2 and EF jets.

Figure 4.21: $(E_t^{LVL1/LVL2}, E_t^{EF})$ map of jets from cosmic muon run 90272.

the calorimeter's calibration. This did not, however, affect the trigger reconstruction, which performed similarly (the small differences will be evaluated next) in the whole η range of the detector. Thus, comparing several trigger reconstructions (in this case where LVL1 and LVL2 jets are compared to EF jets) the miscalibration effect is not visible and only one "correlation line" appears.

In figure 4.21(a) in particular, one can see that there are still some jets that are outside the "line", indicating that the same jet can be reconstructed with very different transverse energies by LVL1 and EF. However, looking at figure 4.21(b) one can see that LVL2 clearly improves LVL1's reconstruction, as most outliers disappear and the great majority of jets falls in the "diagonal".

Still in figure 4.21(b), calibrated LVL2 transverse energy was used for the plot, so that LVL2 and EF energies could be compared at the same scale. Also, it is important to remember that LVL2 jets are only calibrated if $E_t > 20$GeV (figure 4.4(b)), which explains the gap in the "diagonal" and means that one should only look at jets with transverse energies higher than at least 50GeV. Nevertheless, the plot clearly shows that the calibration applied by LVL2 originates higher transverse energy jets than the one applied by EF.

The profile plots in figure 4.22 show stable transverse energy ratios for both LVL1 and LVL2 across the considered range of $E_t^{EF} > 50$GeV. Figure 4.22(b), in particular, shows a flatter distribution, indicating that trans-

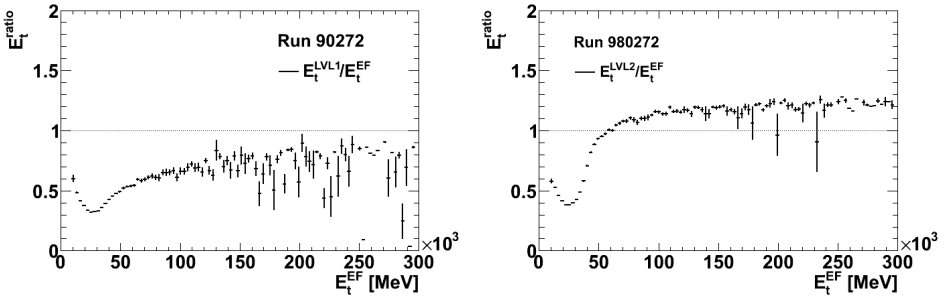

(a) Matched LVL1 and EF jets. **(b)** Matched LVL2 and EF jets.

Figure 4.22: E_t^{ratio} between LVL1/LVL2 and EF matched jets as a function of E_t^{EF} for cosmic muon run 90272.

verse energies reconstructed by LVL2 and EF have a stronger correlation than those reconstructed by LVL1 and EF.

Also, from figure 4.22(a), one can confirm what was seen previously in figure 4.18(c). Indeed, EF calibration overestimates the jet energy for low E_t. This can be seen in figure 4.22(b) as well, although it is important to note that the U-shape of the plot is accentuated, since LVL2 jets are not calibrated at low E_t.

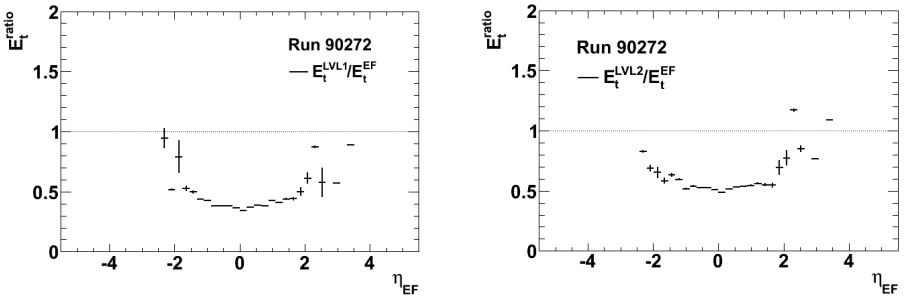

(a) Matched LVL1 and EF jets. **(b)** Matched LVL2 and EF jets.

Figure 4.23: E_t^{ratio} between LVL1/LVL2 and EF matched jets as a function of η_{EF} for cosmic muon run 90272.

Since the energy maps (figure 4.21) showed only one diagonal, one expects that the profile plots of E_t^{ratio} as a function of η_{EF} show flat distributions for the whole barrel and extended barrel range. Indeed, fig-

ure 4.23 shows flat distributions for both LVL1 (figure 4.23(a)) and LVL2 (figure 4.23(b)) jets for $|\eta| < 1.5$.

For $|\eta| > 1.5$, i.e. the encap and forward regions of the detector, the fluctuations are very large. The same behavior was seen for matching between trigger and offline jets (figure 4.19), at which point it was referred that the statistics is very low in this region of the detector, a fact that can be confirmed by looking at the (η, ϕ) maps in figure 4.7.

4.5 Summary and Conclusions

The studies presented in this chapter were intended to evaluate the performance of the three different levels of the ATLAS jet trigger, providing, as well, a good test of the quality of the data. Since collision data was not available at ATLAS, cosmic muons were used to mimic the energy depositions left by jets in the calorimeters. In particular, the results from the analysis of cosmic muon run 90272 were presented. The evaluation was done by comparing the reconstruction of jets performed by the trigger and the reconstruction performed offline, which is considered the best available. Although simple, the analysis showed great power, allowing, especially, the identification of problems that might influence the performance of the ATLAS jet trigger.

The first analysis consisted in a separate evaluation of the jet reconstruction performed by each trigger level and offline. On the one hand, this simple analysis allowed the confirmation of several mentioned aspects related to jets and the ATLAS jet trigger. In particular, concerning the jets, the decrease in the number of events as the number of jets per event increase, the decrease in the number of jets with the increasing transverse energy, the favored central distribution and the uniform azimuthal distribution were observed. As for the ATLAS jet trigger, the distributions validated the fact that trigger towers have only a few η bins in the forward calorimeters.

On the other hand, slight deviations from the expected results enabled the identification of some issues that had to be addressed in further analysis. For example, the HLT was not running in the forward region, the offline transverse energy was not calibrated and the LVL2 transverse energy was only calibrated for jets with $E_t > 20GeV$. Concerning the latter, this was

corrected and in present cosmic muon runs, LVL2 jets are calibrated in the full E_t range. Most importantly, nonetheless, was that several noisy calorimeter cells were identified. Jets reconstructed from these cells were found in every trigger level and offline as well. Thus, they were removed, so they would not bias the subsequent analysis.

The analysis continued with a more direct comparison between trigger and offline reconstructions, which was done by matching trigger and offline jets. Matching jets allowed, for example, the evaluation of the spatial precision and resolution of the jet reconstruction performed by the trigger. In particular, it was confirmed that each trigger level improved the reconstruction of the position performed by the previous level. Also, it was verified that LVL1's reduced granularity algorithms influenced the the spatial precision.

After examining the spatial reconstruction, the energy reconstruction was evaluated. This allowed the identification of a problem in the offline energy reconstruction in the extended barrel of the TileCal, which led offline to overestimate the energy of the jets identified in that region of the calorimeter. The problem was later solved, and present cosmic muon runs no longer reveal this behavior. Despite this problem, in the central region, the trigger energy scale was uniform and stable, both with η and E_t. LVL2, in particular, reconstructed $\approx 95\%$ of the offline jet energy in the central pseudorapidity region ATLAS.

Motivated by what happens during the online monitoring of the runs, when offline reconstruction is still not available, LVL1 and LVL2 jets were matched to EF jets. The analysis performed with these pairs was similar to the one performed with trigger and offline matched jets and similar observations were made. In particular, the comparison between LVL2 and EF reconstructed energies indicated that either the calibration applied at LVL2 overestimates the energy of the jets or EF underestimates that energy. Given the simplicity and potential of this analysis, the goal at this point is to try to include some of the presented histograms in the online monitoring of the data quality.

Chapter 5

Intercalibration in η of LVL2 Jets with Simulated QCD Dijet Events

5.1 Objectives and Motivation

In an environment where jets are both signal and background, the performance of the ATLAS jet trigger is highly dependent on accurate determination of the jet energy scale. This can only be achieved through calibration of the jet energy (sections 1.2.3.2 and 3.1.2). It was discussed in section 3.2.2 that the jet trigger applies a MonteCarlo-based calibration step at LVL2, to calibrate the jets at particle level, going from the EM/uncalibrated-scale to the hadronic/calibrated-scale.

The MonteCarlo generators and simulators used in ATLAS constitute a tool and do not reproduce the detector perfectly. Thus, when data taking begins, real data will surely differ from simulated data. Consequently, it is likely that the calibration derived for LVL2 does not suit real data. In reality, this statement is true for any type of calibration that relies on MonteCarlo, which is why MonteCarlo-idependent methods have to be developed, so that the calibration can be validated when applied to real data. In particular, "validated" means that the jet energy scale is tuned if necessary and its uncertainty is determined.

These methods are referred to as *in-situ* validation or *in-situ* calibration

methods. On the one hand, they represent a very important cross-check of the calibration steps. On the other hand, since, they allow tuning of the jet energy scale, the combination of several of these methods can actually constitute the second calibration step that brings the jet energy scale from particle to parton level (section 3.1.2). In this chapter a *in-situ* calibration method, called intercalibration in η, will be applied to MonteCarlo simulated dijet events. The goal is to determine whether it can be used to validate and correct the calibration of LVL2 trigger jets in the beginning of data taking.

It is important to note that the *in-situ* calibration method presented here is a relative method. It uses dijet events and aims at uniformizing the jet energy scale with respect to η. After the method is applied the jet energy scale will most likely not be set at 1 but will be flatter across η. In other words, intercalibration in η provides a relative jet energy scale. To achieve the absolute jet energy scale, i.e., the energy scale at parton level, other *in-situ* calibration methods have to be used, namely methods that use $\gamma + jet$ or $Z + jet$ events[1], but these subject will not be addressed here.

5.2 MonteCarlo Simulated Events

PYTHIA [58, 59] is a general purpose generator for hadronic events in pp, e^+e^- and e^+p colliders. PYTHIA provides an accurate representation of the event properties and together with GEANT [60], the simulator for the ATLAS detector, it is a very commonly used tool in ATLAS.

The generator contains around 240 different $2 \rightarrow n$ processes but it is mainly optimized for $2 \rightarrow 1$ and $2 \rightarrow 2$ processes. A common one is the QCD $2 \rightarrow 2$ partonic scattering, which is basically the generation of the event $p + p \rightarrow jet + jet + X$, described in section 1.2.2. For generating these events, PYTHIA uses a number of different physical parameters and a set of specific configurations for modeling the underlying event, hadronization, ISR, etc. [61].

The most basic parameter used by PYTHIA, which works as a regulating

[1] With dijet events only hadronic objects, whose energy scale is not well determined, are compared, which is why only a relative scale is obtained; with $\gamma + jet$ or $Z + jet$ events hadronic objects are compared to electromagnetic objects, whose energy scale is very well understood, allowing the absolute jet energy scale to be obtained.

parameter, is p_t^{min}. It is the lower limit of the transverse momentum used in the calculation of the cross section of the hard scattering between the two partons. Because the cross-section for jet production decreases exponentially with the increasing transverse energy, the p_t^{min} cut allows for jets to be generated in several p_t ranges (particularly high p_t) [61].

To perform the studies described before, a set of data samples containing PYTHIA generated dijet[2] events [52] was used. For these, the LHC's pp collisions were simulated with a center of mass energy of $\sqrt{s} = 10$TeV and at a luminosity of $\mathcal{L} = 10^{31}\text{cm}^{-2}\text{s}^{-1}$. The simulated geometry for the ATLAS detector was perfect, i.e., no misalignments. A total of eight samples were used, each one containing a different value for p_t^{min}. Table 5.1 summarizes the relevant information about the used samples.

PYTHIA QCD Dijet		
Sample	p_t *Range [GeV]*	σ *[pb]*
J1	$17 - 35$	8.67×10^8
J2	$35 - 70$	5.60×10^7
J3	$70 - 140$	3.28×10^6
J4	$140 - 280$	1.52×10^5
J5	$280 - 560$	5.12×10^3
J6	$560 - 1120$	1.12×10^2
J7	$1120 - 2240$	1.075
J8	> 2240	1.12×10^{-3}

Table 5.1: Information concerning the data samples containing dijet events generated with PYTHIA [52].

In particular, from the mentioned samples, only truth and LVL2 jets were used in the studies. Truth jets were obtained by applying a 0.4-Cone algorithm to the stable particles produced by PYTHIA's hadronization model. LVL2 simulated jets were identified and their energies were calibrated, as described in section 3.2.2. The calibration was not "perfect", in the sense that it did not produce a LVL2 hadronic energy scale calibrated to particle level. Nonetheless, we expect the calibration at the beginning of data taking

[2]"Dijet" does not mean only two jets exist in the event; this is the used expression for two outgoing partons that suffered hard scattering.

to be worst than the one used.

For completeness, the p_t, η and ϕ distributions of the truth jets are presented in figure 5.1. The distributions show the expected shapes: most jets are found in the central region of the detector (figure5.1(b)) and flat ϕ distribution (figure 5.1(c)). As for the p_t distribution (figure 5.1(a)), the shape is the expected exponential, only it is repeated eight times across the transverse momentum range. This is related to the eight data samples generated with eight different p_t^{min} cuts (notice the peaks of the distribution are located at p_t^{min}).

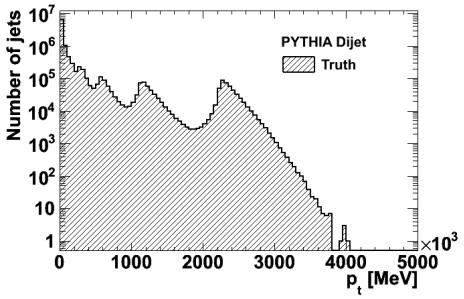

(a) p_t distribution.

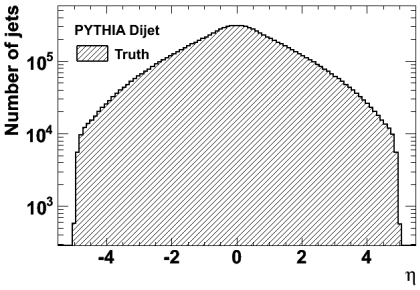

(b) η distribution.

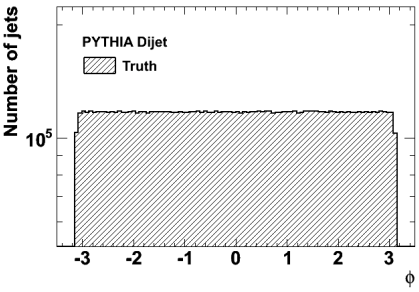

(c) ϕ distribution.

Figure 5.1: Distributions for truth jets from QCD dijet events generated by PYTHIA.

5.3 Intercalibration in η

5.3.1 Description of the Method

The calorimeter response for jets at EM-scale is highly dependent on the η coordinates of the jets, which is why the uncalibrated jet energy scale reveals significant variations with η. The calibration applied to correct the measured energy of the jets sets the jet energy scale to hadronic. The calibration weights are meant to correct for detector effects, such as calorimeter non-compensation, noise, losses in dead material and cracks, etc. It is, thus, expected that, after the calibration is applied, the effect of calorimeter response is corrected and the jet energy scale becomes uniform and flat throughout the detector. This can be not only verified but also corrected using intercalibration in η [23].

In summary intercalibration in η [13, 23] is a *in-situ* calibration method that uses p_t conservation in dijet events. It allows the validation and correction, if needed, of the uniformity in η of the hadronic energy scale. Consequently, one can say that intercalibration in η validates and corrects the calibration applied to jets at EM-scale. The result is a relative hadronic jet energy scale.

The method of intercalibration in η assumes that the calibration applied to the jets is stable, uniform and well understood in a small region in pseudorapidity, labelled as the reference region. Any region in pseudorapidity not included in the reference region is called the probe region. The goal of intercalibration in η is to evaluate and correct the energy of the jets in the probe region by comparing them with jets in the reference region. The comparison is based on transverse momentum conservation and uses p_t balance between two jets.

Given the basis of the method, it can only be applied to certain events that fulfill a set of conditions. In particular, since the method uses p_t conservation between jets, one has to select events where the p_t can be correctly balanced. To better understand which events the method can be applied to, let us consider figure 5.2, where a 4-jet event resulting from a pp collision is depicted and the selection criteria are summarized:

1. The first selection criterion is clear: only events that have at least two jets can be used. For those events, the two leading jets, i.e. the jets

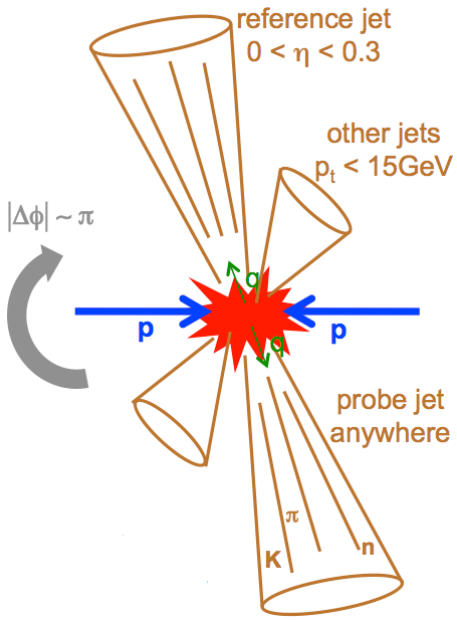

Figure 5.2: Representation of the intercalibration in η method.

with the highest p_t, are found. They will be referred to as the leading and subleading jets and they will be the ones whose p_t will be balanced against each other.

2. For events with more than two jets the third jet with the highest p_t is also found. To ensure p_t conservation between the leading jets in the events, any events with p_t^{third} above a certain energy threshold are eliminated. This threshold was chosen to be 15GeV, which means that if more than two jets exist in the event, their p_t are below 15GeV. This way, the calculations of p_t balance are not greatly influenced and the statistics are not severely cut on.

3. Only events whose leading jets are back-to-back are kept. This is equivalent to requiring $|\Delta\phi| \approx \pi$, where $\Delta\phi = \phi_{subleading} - \phi_{leading}$ and is also meant to ensure that p_t conservation can be applied to the leading jets. The actual condition used was $\pi - 0.15 < |\Delta\phi| < \pi + 0.15$, which was considered a good compromise between the necessary tightness of the condition and loss of statistics.

4. It was mentioned that, with intercalibration in η, jets in the probe

region are compared to jets in the reference region. Thus, the final selection condition demands that only events having at least one of the leading jets in the reference region are kept. In other words, if both leading jets in the event are in the probe region, the event is eliminated. The reference region chosen was $0 < \eta < 0.3$. This is a central region of the detector, far from the cracks, where we expected statistics to be high and the calibrations to be well known and not to suffer large variations.

After this last selection, the remaining events can be categorized in three types. There are events whose leading jet is in the reference region and whose subleading jet is in the probe region. For those, the leading jet was labelled reference jet and the subleading jet was labelled probe jet. There is also the opposite case, i.e., events where the subleading jet is in the reference region, becoming the reference jet, and the leading jet is outside the reference region, becoming the probe jet. Finally, there are events that have both the leading and subleading jets in the reference region of the detector. Even though they are both reference jets, for calculation purposes they still have to be labelled either as reference or as probe jets and the choice cannot introduce any biases. In the end, the choice of which one was the reference and which one was the probe jet was done randomly.

To summarize, after all the selection conditions were applied, there were one reference jet and one probe jet per event and they were the two jets with the highest p_t in the event. The reference jet always had $0 < \eta < 0.3$ and the probe jet was anywhere in the detector (in some cases it was also in the reference region). They were back-to-back jets and all other jets in the event had $p_t < 15$GeV.

Given the conditions created by the selection cuts, one can consider that p_t is conserved between the reference and the probe jet of each event. Thus, the next step of the method consists of balancing the transverse momentum of the reference and probe jets. The variable asymmetry, defined as

$$A = \frac{p_t^{probe} - p_t^{reference}}{p_t^{average}}$$

with

$$p_t^{average} = (p_t^{reference} + p_t^{probe})/2$$

was chosen for this purpose. The choice was related to the fact that, because of transverse momentum conservation, A has a symmetric distribution around zero, whereas for example the response

$$R = \frac{p_t^{probe}}{p_t^{reference}}$$

which could also have been used, is intrinsically asymmetric around 1.

Thus, A was calculated for each selected event. The distributions of A were evaluated in 32 η_{probe} bins, 0.3-wide and ranging from $[-4.8, 4.8]$, and five $p_t^{average}$ bins - $[50, 200]$GeV, $[200, 500]$GeV, $[500, 1000]$GeV, $[1000, 2000]$GeV and $p_t^{average} > 2000$GeV. "Evaluated" means that gaussian fits were applied to the distributions[3] and the mean values of those fits were extracted and plotted as a function of η_{probe} for each $p_{average}$ bin.

5.3.1.1 Validation of the Jet Energy Scale

Take a reference and a probe jet of an event that passed the selection criteria in some η_{probe} bin and $p_t^{average}$ bin. The selection criteria are applied so one can properly balance the p_t of the two jets. Thus, because of p_t conservation one should have $p_t^{reference} = p_t^{probe}$.

Most likely the response of the calorimeter in the reference region and in the considered probe region is different, so if the measured energy of the jets is not calibrated one will certainly have $p_t^{reference} \neq p_t^{probe}$. Calibration, however, is meant to correct for this effect, converting a non-uniform EM-scale in a uniform hadronic-scale.

Suppose, however, the calibration applied to these jets did not result in a uniform hadronic scale across η. In particular, suppose the energy scale is different in the reference region and in the considered probe region. Again, one will have $p_t^{reference} \neq p_t^{probe}$. Moreover, this will be true not only for the considered event but for all events in the same η_{probe} bin and $p_t^{average}$ bin. Consequently, the mean value of the gaussian fit applied to the asymmetry distribution for those bins will not be zero.

Thus, the deviations of the asymmetry from zero are a measure of the goodness of the calibration applied. Furthermore, if the calibration is good,

[3]The gaussian fits were applied in the A range of $[-0.35, 0.35]$ and distributions with less than 60 entries were discarded.

the mean value of A as a function of η_{probe} will be stable and uniform across the analyzed range.

5.3.1.2 Correction of the Jet Energy Scale

Summarizing what was said before, applying intercalibration in η to calibrated jets allows the evaluation of the uniformity of the hadronic energy scale and consequent validation of the calibration. However, if the results prove the calibration was not good enough to provide a uniform hadronic scale, the method also provides a way to tune the calibration improving the uniformity. The process to do so is described next.

As mentioned in the previous section, if the calibration is not good then $p_t^{reference} \neq p_t^{probe}$. Tuning the calibration is done by correcting the probe region of the calorimeter , which is almost its full η range, with respect to the reference region. In particular, p_t^{probe} is corrected in the following way:

$$p_t^{corrected} = k \times p_t^{probe} = p_t^{reference}$$

Thus, k is the correction constant we wish to determine.

Remembering that

$$A = \frac{p_t^{probe} - p_t^{reference}}{(p_t^{reference} + p_t^{probe})/2}$$

and since

$$k = \frac{p_t^{reference}}{p_t^{probe}}$$

the asymmetry can also be written as

$$A = \frac{2(1-k)}{k+1}$$

Inverting the variables, i.e., writing k as a function of A, one obtains

$$k = \frac{2-A}{2+A}$$

In the previous sections, it was explained that the asymmetry distribution was evaluated in 32 η_{probe} bins (i) and 5 $p_t^{average}$ ranges (j), which means a total of $i \times j = 32 \times 5 = 160$ distributions were evaluated. In particular, a gaussian fit was applied to all of the distributions and the mean value A_{ij} and correspondent uncertainty ΔA_{ij} of each fit were extracted. Therefore,

one can extract correction constants (and the associated uncertainties) for the 32 η_{probe} bins and 5 $p_t^{average}$ ranges in the following manner:

$$k_{ij} = \frac{2 - A_{ij}}{2 + A_{ij}}$$

and

$$\Delta k_{ij} = \frac{4}{(2 + A_{ij})^2} \Delta A_{ij}$$

It is important to note that for the η_{probe} bin of $[0, 0.3]$, that corresponds to the region of the detector taken as reference, k was set to one. Even though, in the description of the method, it was said that, when both leading jets were in the reference region, one was chosen as the reference and the other as the probe jet (the choice was random), the truth is that both of them are reference jets and need not be corrected. The choice was merely so that no bias was introduced when calculating the asymmetry in this bin.

Still on the subject of the reference bin, the method assumes that in this region of the detector the calibration is well known and produces a stable jet energy scale in η. It is however important to note that the scale does not have to be stable at 1. This method evaluates the uniformity of the jet energy scale, regardless of its value, which is why it was referred to as relative method. With intercalibration in η, several regions of the detector are evaluated with respect to this reference region. Thus, the stability is evaluated also with respect to a reference region and the final energy scale established is relative to that region as well. Other *in-situ* calibration methods can be used afterwards, to establish the absolute and final jet energy scale.

5.3.2 Accuracy of the Method

As already mentioned, real collision data is still not available at ATLAS. Nonetheless, MonteCarlo simulated events can provide a powerful tool in preparing for the beginning of data taking. For example, applying intercalibration in η to MonteCarlo simulated dijets can help determining if this *in-situ* calibration method will serve its purpose when applied to real data. In particular, since truth jets are available and they represent jets at particle level, applying the method to truth jets will reveal its maximum potential.

Thus, in this section, the accuracy of the intercalibration in η method is obtained from the results of applying intercalibration in η to truth jets.

Basically, the selection criteria required by the method and described in section 5.3.1 were applied to truth dijet events (section 5.2). The following distributions in figure 5.3 are presented for completeness and show the effect of the selection cuts in the sample.

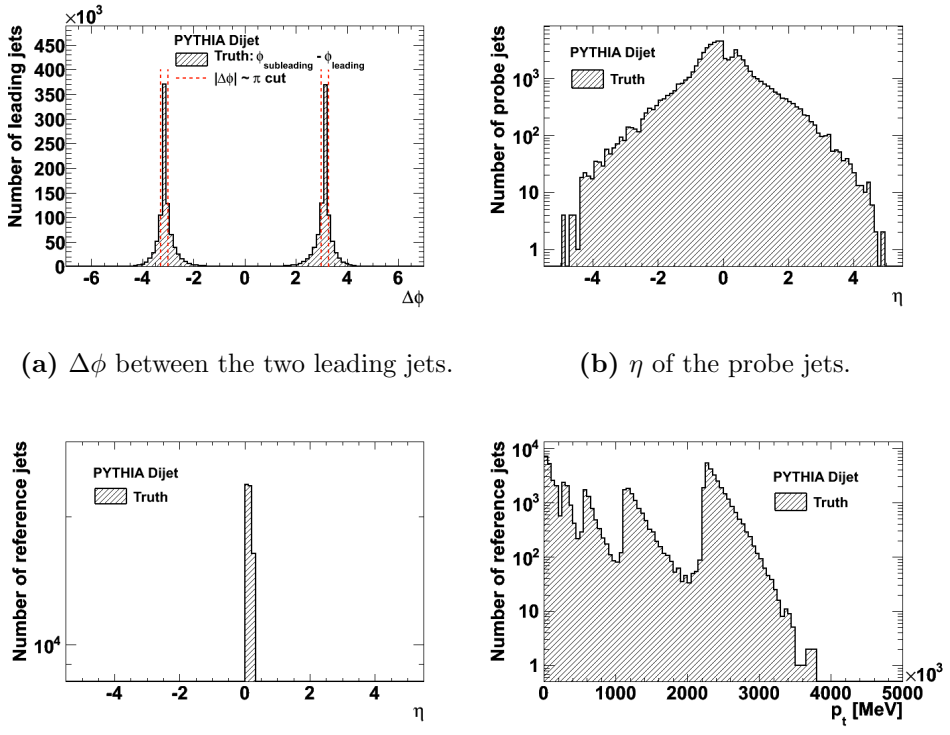

(a) $\Delta\phi$ between the two leading jets.

(b) η of the probe jets.

(c) η of the reference jets.

(d) p_t of the reference jets.

Figure 5.3: Distributions representing the selection criteria for the application of intercalibration in η to truth jets from QCD dijet events generated by PYTHIA.

For those events passing the selection criteria, A was calculated and the distribution of A was evaluated in η_{probe} and $p_t^{average}$ bins. To serve as an example, two of those distributions are presented in figure 5.4.

To better evaluate A across the η_{probe} range, the mean value of each gaussian fit was plotted as a function of η_{probe} for each $p_t^{average}$ bin. The plots are presented in figure 5.5.

From plots in figure 5.5 one can evaluate the accuracy of the method.

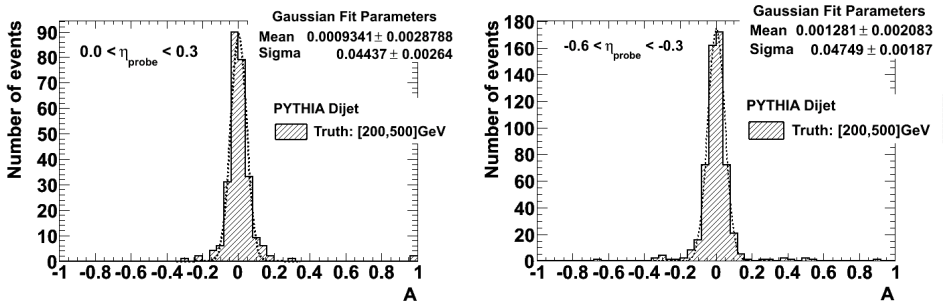

(a) $0.0 < \eta_{probe} < 0.3$. **(b)** $-0.6 < \eta_{probe} < -0.3$.

Figure 5.4: Examples of asymmetry distributions for truth jets from QCD dijet events generated by PYTHIA with 200GeV$< p_t^{average} <$ 500GeV.

This is in the sense that calibration is meant to correct the energy of the jets to particle level, so applying intercalibration in η to any other type of calibrated jets will always reveal more asymmetries than for truth jets (or the same if the calibration is "perfect"). Thus, table 5.2 presents the maximum and minimum values of the asymmetries obtained for truth jets, i.e., the approximate accuracy of the method.

Intercalibration in η of Truth Jets		
	A Minimum	*A Maximum*
$50\,GeV < p_t^{average} < 200\,GeV$	-0.0080	0.0290
$200\,GeV < p_t^{average} < 500\,GeV$	-0.0100	0.0090
$500\,GeV < p_t^{average} < 1000\,GeV$	-0.0020	0.0040
$1000\,GeV < p_t^{average} < 2000\,GeV$	-0.0015	0.0020
$p_t^{average} > 2000\,GeV$	-0.0010	0.0010

Table 5.2: Approximate accuracy of intercalibration in η determined from applying the method to truth jets from QCD dijet events generated by PYTHIA.

Analyzing now the values in table 5.2, one can see that the asymmetries decrease as $p_t^{average}$ increases. Also, there is a tendency for the maximum value of the asymmetry to be higher than the absolute minimum value. This reflects a tendency visible in the distributions of figure 5.5, for the distribution of A to shift towards positive asymmetries as $|\eta|$ in-

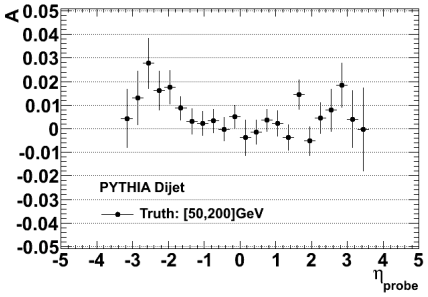

(a) 50GeV$< p_t^{average} <$ 200GeV

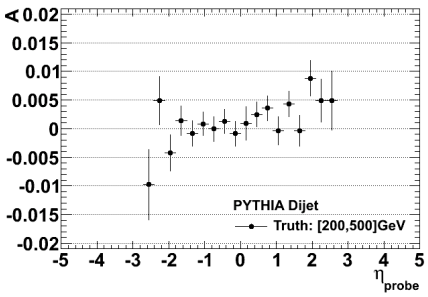

(b) 200GeV$< p_t^{average} <$ 500GeV

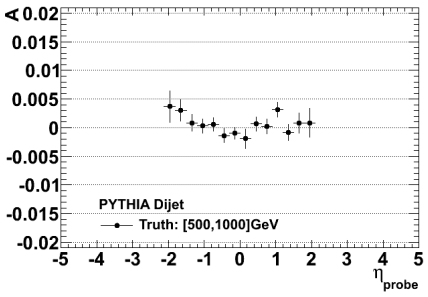

(c) 500GeV$< p_t^{average} <$ 1000GeV

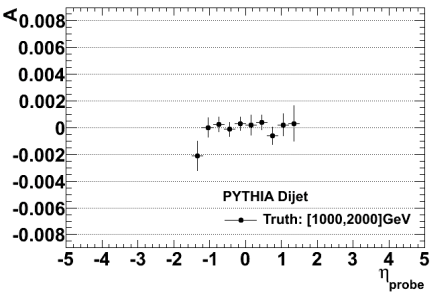

(d) 1000GeV$< p_t^{average} <$ 2000GeV

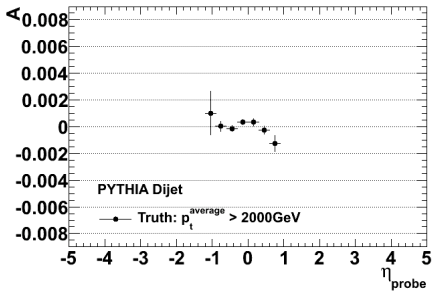

(e) $p_t^{average} >$ 2000GeV

Figure 5.5: Mean value of the asymmetry for truth jets from QCD dijet events generated by PYTHIA.

creases. Given the definition of A, this means that for higher pseudorapidities $p_t^{probe} > p_t^{reference}$. Since jets at particle level are being analyzed and the reconstruction of these jets does not suffer from calorimeter effects, this shift in the asymmetry can only be caused by the jet algorithm.

Indeed, a possible explanation is related to the shape of the jets and the fact that a small cone algorithm is used in the reconstruction. In theory, one should have $p_t^{probe} = p_t^{reference}$. However, as one moves forward in η_{probe}, p^{probe} becomes larger than $p^{reference}$. Usually, jets with high momenta are narrower and more collimated than low momenta jets. This means that even though we may have $p_t^{probe} = p_t^{reference}$ in a high η_{probe} bin, the reference jet is, very likely, wider than the probe jet. Consequently, the small cone jet algorithm might not collect all the particles belonging to the reference jet, hence the observed inequality $p_t^{probe} > p_t^{reference}$.

Taking all into consideration, one can say that this effect is expected to decrease for higher $p_t^{average}$ bins. Indeed, that is observed, both in figure 5.5 and in table 5.2.

5.4 Intercalibration in η of LVL2 Jets

5.4.1 Validation of the LVL2 Jet Energy Scale

As mentioned in section 3.2.2, the jet trigger applies a simple calibration step at LVL2 to try to bring trigger jets to the hadronic scale. Once more, after this calibration step, the energy scale should be flat and uniform across the whole η range of the detector. Thus, intercalibration in η can be applied to LVL2 jets to validate this calibration. The results are presented next.

Intercalibration in η was applied to LVL2 jets as described in section 5.3.1. Figure 5.6 shows the mean values of the asymmetry distributions for several η_{probe} and $p_t^{average}$ bins.

The results reveal that even after the calibration was applied, the asymmetries between LVL2 jets in the reference and probe regions are still large, indicating that the calibration did not produce an energy scale uniform in η. This conclusion is drawn also by comparing these plots to the ones obtained for truth jets (figure 5.5). Because calibration is supposed to bring the energy of the jets to particle level, a "perfect" LVL2 calibration would produce asymmetries like the ones seen for truth jets and presented in table 5.2. Thus, larger asymmetries indicate the calibration was not fully effective.

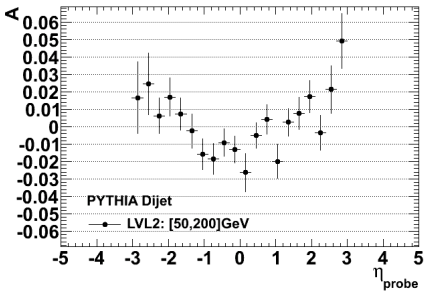

(a) 50GeV$< p_t^{average} <$ 200GeV

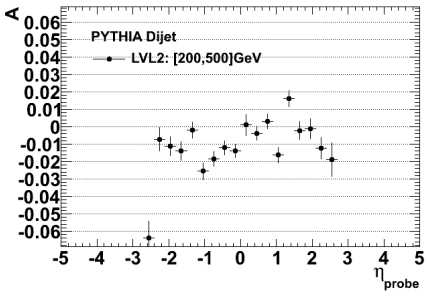

(b) 200GeV$< p_t^{average} <$ 500GeV

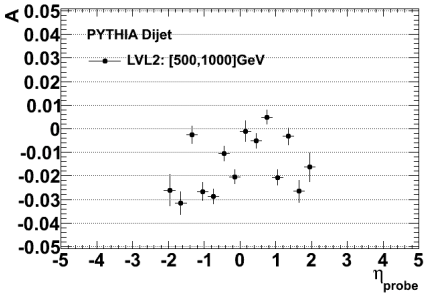

(c) 500GeV$< p_t^{average} <$ 1000GeV

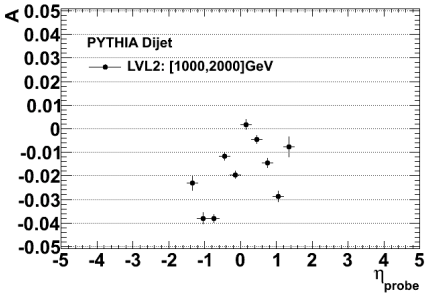

(d) 1000GeV$< p_t^{average} <$ 2000GeV

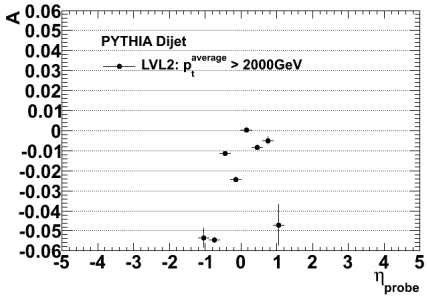

(e) $p_t^{average} >$ 2000GeV

Figure 5.6: Mean value of the asymmetry for LVL2 jets from QCD dijet events generated by PYTHIA.

5.4.2 Correction of the LVL2 Jet Energy Scale

The previous section showed that the calibration applied to LVL2 trigger jets did not produce a uniform hadronic scale. Thus, one can try to apply

the technic described in section 5.3.1.2 to tune the calibration and improve the asymmetries observed in figure 5.6. According to what was seen in section 5.3.2, the improvement should be possible within the limitations indicated in table 5.2.

To apply the correction method (section 5.3.1.2), the full sample was divided in three. Two thirds of the sample were used to extract the several values of k[4], that were then used to correct p_t of the probe jets in the remaining third of the sample.

The correction constants (and associated uncertainties) obtained for each analyzed bin are presented in figure 5.7. The asymmetries, both before and after the correction constants were applied, are shown in figure 5.8. Finally, the minimum and maximum values obtained for the asymmetries presented in table 5.3.

Intercalibration in η of LVL2 Jets				
	A Before		*A After*	
	Min.	*Max.*	*Min.*	*Max.*
$50\,GeV < p_t^{average} < 200\,GeV$	-0.0450	0.0600	-0.0520	0.0440
$200\,GeV < p_t^{average} < 500\,GeV$	-0.0300	0.0250	-0.0240	0.0300
$500\,GeV < p_t^{average} < 1000\,GeV$	-0.0420	0.0080	-0.0160	0.0150
$1000\,GeV < p_t^{average} < 2000\,GeV$	-0.0360	0.0040	-0.0080	0.0140
$p_t^{average} > 2000\,GeV$	-0.0600	0.0010	-0.0100	0.0015

Table 5.3: Approximate asymmetry of LVL2 jets from QCD dijet events generated by PYTHIA before and after applying the corrections derived with intercalibration in η.

By looking at figure 5.8, one can already see that the corrections derived from intercalibration in η can severely improve the asymmetries, particularly for the high $p_t^{average}$ bins. Nonetheless, the comparison between tables 5.2 and 5.3 allows a more qualitative analysis.

In particular, one can see that, indeed, the calibration applied to LVL2 jets did not bring the jet energy scale to particle level. This is because the maximum values of A for LVL2 jets are always larger than the ones for

[4]There should be 160 values of k but the low statistics in some bins prevented the extraction of the correction constant.

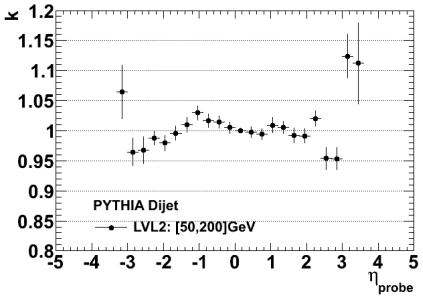

(a) 50GeV$< p_t^{average} <$ 200GeV

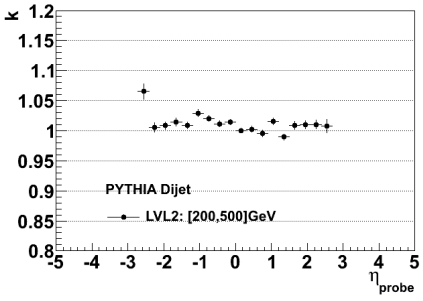

(b) 200GeV$< p_t^{average} <$ 500GeV

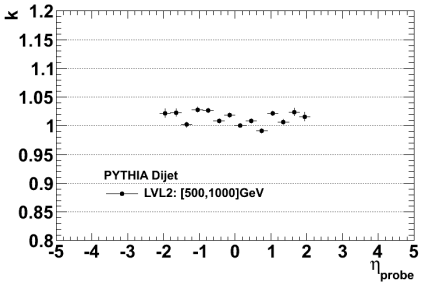

(c) 500GeV$< p_t^{average} <$ 1000GeV

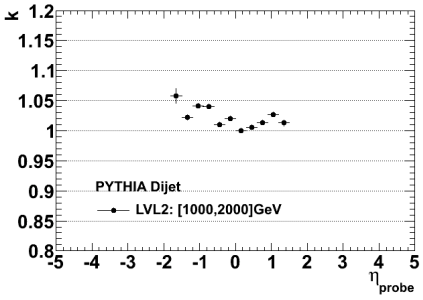

(d) 1000GeV$< p_t^{average} <$ 2000GeV

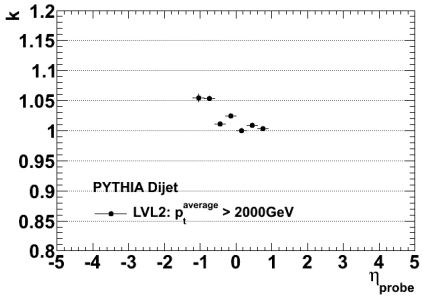

(e) $p_t^{average} >$ 2000GeV

Figure 5.7: Correction constants for LVL2 jets from QCD dijet events generated by PYTHIA.

truth jets (or equal, in the highest $p_t^{average}$ bin) and the minimum values are smaller for LVL2 jets in every $p_t^{average}$ bin. In other words, the asymmetries for LVL2 jets span a larger range than for truth jets.

The situation is actually the same even after the corrections derived

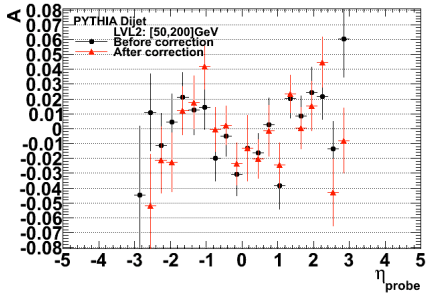

(a) 50GeV$< p_t^{average} <$ 200GeV

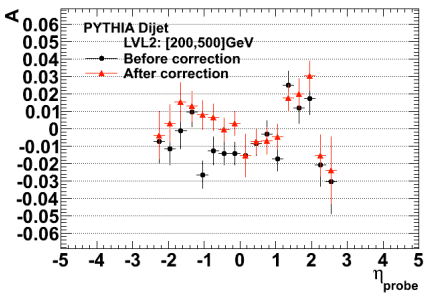

(b) 200GeV$< p_t^{average} <$ 500GeV

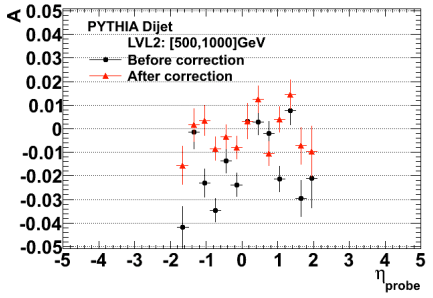

(c) 500GeV$< p_t^{average} <$ 1000GeV

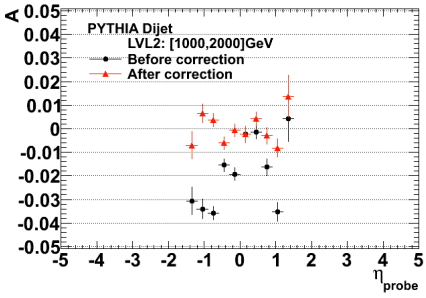

(d) 1000GeV$< p_t^{average} <$ 2000GeV

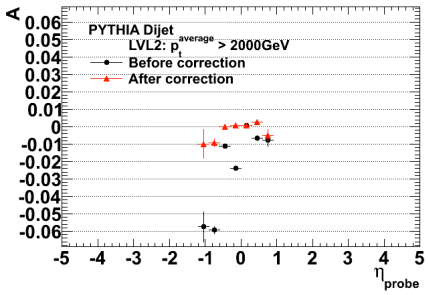

(e) $p_t^{average} >$ 2000GeV

Figure 5.8: Mean value of the asymmetry for LVL2 jets (before and after correction) from QCD dijet events generated by PYTHIA.

from intercalibration in η are applied, meaning that the corrected LVL2 jet energy scale is still not at particle level. Moreover, the results show that the corrections only improve either the minimum or the maximum value of A, worsening the other. Nonetheless, it is important to note that the range of

the asymmetries is reduced for every $p_t^{average}$ bin, which is why we declare the corrections improve the asymmetries.

5.4.3 Closure Test

The previous section showed that with intercalibration in η one is able to extract correction constants that tune the calibration applied to LVL2 trigger jets. In fact, it was verified that the corrections improved the asymmetries across η between reference and probe jets, which suggests that the LVL2 jet energy scale was also improved. Nonetheless, since MonteCarlo simulated data was used and truth jets are available, a final test can be done for confirmation.

Remember truth jets are jets at particle level and constitute the reference for the calibration applied to LVL2 jets. So basically, for the closure test, one can compare the LVL2 energy of the jets to the corresponding truth energy. This is done by analyzing the response

$$R = \frac{E^{LVL2}}{E^{truth}}$$

i.e. the ratio between the energy of LVL2 jets, before and after the corrections derived with intercalibration in η, and the energy of the matching truth jets.

The first step of this closure test is, thus, to match LVL2 and truth jets. The matching process used was similar to the one described in section 4.4.2, intended to match trigger and offline "cosmic jets". Essentially, a truth jet in one event is matched to the LVL2 jet in that event that is the closest in the (η, ϕ)-space. "Closest" is evaluated by calculating the distance between the jets:

$$\Delta R = \sqrt{(\eta_{LVL2} - \eta_{truth})^2 - (\phi_{LVL2} - \phi_{truth})^2}$$

Also, the matching is done so that the same LVL2 jet can be matched to several truth jets of the same event. Finally, matched jets with $\Delta R > 0.2$ are excluded from the analysis, in order to guarantee a more efficient matching.

After the matching was done, R was calculated for every pair of matched truth and LVL2 jets. The distributions of R were plotted in 32 bins of η_{truth} (from $\eta_{truth} = -4.8$ to $\eta_{truth} = 4.8$, 0.3 wide) and 5 bins of p_t^{LVL2} ($[50, 200]$GeV, $[200, 500]$GeV, $[500, 1000]$GeV, $[1000, 2000]$GeV and $p_t^{LVL2} >$

2000GeV). Similarly to what was done with the asymmetry distributions, the resulting response distributions were fitted with a gaussian[5]. The mean value and associated error of each fit was extracted from the several R distributions and they were plotted as a function of η_{truth} for the five p_t^{LVL2} bins. The results are presented in figure 5.9.

Finally, this procedure was repeated, only E^{LVL2} was corrected by the factors calculated earlier using intercalibration in η (figure 5.9). In reality, the correction factors were applied to p_t^{LVL2} (since they were extracted using p_t balance) and, from there, the momentum was calculated by doing $p = p_t \times \eta$. The energy was obtained by doing $E = p$, since at trigger level the mass of the jet is not calculated.

Figure 5.9 shows that the intercalibration in η method clearly improves the uniformity of the jet energy scale in pseudorapidity, particularly in the high p_t range, as suggested before by the results in figure 5.8. In fact, only the lowest p_t bin showed no improvement. Overall, the improvement is more significant in the the barrel and extended barrel regions of the detector ($|\eta| < 1.5$). For the endcap region, larger fluctuations appear in the corrected energy scale but still the stability of the scale was improved. Finally, the method appears to be ineffective in the forward regions of the calorimeter ($|\eta| > 3.2$), where the jet energy scale actually becomes more unstable after the corrections are applied (this can be seen in figure 5.9(a)). Table 5.4 summarizes the improvements in the LVL2 jet energy scale obtained with the corrections from intercalibration in η.

5.4.4 Efficiencies and Uncertainties of the Method

From section 5.3.1, one can see that the applying the intercalibration in η method requires selecting events in the full data sample, which severely reduces the statistics. Thus, to conclude the analysis of this *in-situ* calibration method, an evaluation was done to determine how, given the efficiencies of each cut, the statistical uncertainty varies with the integrated luminosity. The main goal of this analysis is to determine if this method can indeed be used in real data.

To do this, a smaller sample (section 5.2) was chosen. This sample had

[5]The gaussian fits were applied in the R range of $[0.5, 1.4]$ and distributions with less than 60 entries were discarded because of low statistics.

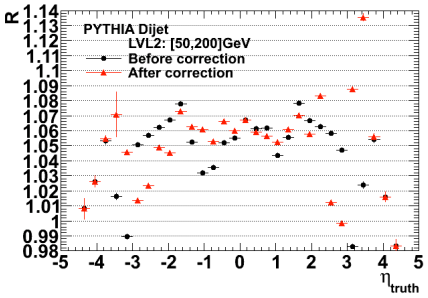

(a) 50GeV$< p_t^{LVL2} <$ 200GeV

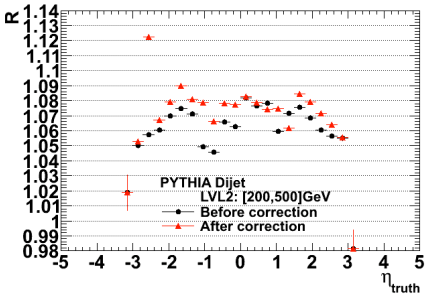

(b) 200GeV$< p_t^{LVL2} <$ 500GeV

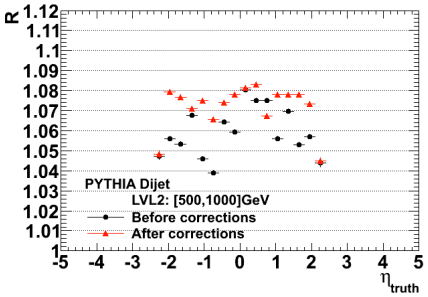

(c) 500GeV$< p_t^{LVL2} <$ 1000GeV

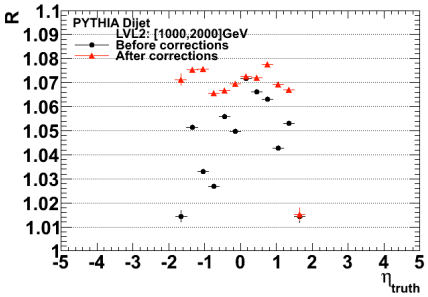

(d) 1000GeV$< p_t^{LVL2} <$ 2000GeV

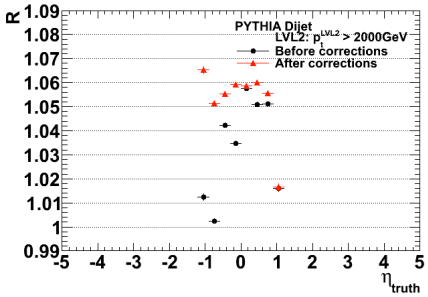

(e) $p_t^{LVL2} >$ 2000GeV

Figure 5.9: Mean value of the response for LVL2 and truth matched jets (before and after correction using intercalibration in η) from QCD dijet events generated by PYTHIA.

224861 events and a parton cut of 70GeV$< p_t^{parton} <$ 140GeV. LVL2 jets with 90GeV$< p_t^{LVL2} <$ 120GeV were used. In real data, LVL2 jets in this range have to pass a LVL1 threshold of 70GeV (section 3.2.4). Thus, the first

Intercalibration in η of LVL2 Jets		
	Energy Scale Before	*Energy Scale After*
$50\,GeV < p_t^{LVL2} < 200\,GeV$	$\pm 5\%$	$\pm 5\%$
$200\,GeV < p_t^{LVL2} < 500\,GeV$	$\pm 3.5\%$	$\pm 3\%$
$500\,GeV < p_t^{LVL2} < 1000\,GeV$	$\pm 4\%$	$\pm 1.5\%$
$1000\,GeV < p_t^{LVL2} < 2000\,GeV$	$\pm 5.5\%$	$\pm 0.5\%$
$p_t^{LVL2} > 2000\,GeV$	$\pm 5.5\%$	$\pm 1\%$

Table 5.4: Approximate precision of the LVL2 jet energy scale from QCD dijet events generated by PYTHIA before and after applying the corrections derived with intercalibration in η.

selection cut applied to this sample was to only keep events that passed this LVL1 threshold, i.e. events that had at least one LVL1 jet with $p_t > 70$GeV.

Afterwards, the cuts related to the intercalibration in η method were applied, as described in section 5.3.1. In summary, at least two jets in each event, leading jets back-to-back, cut on p_t^{third}, at least one of the leading jets in the reference region, transverse momentum binning of 90GeV$< p_t^{LVL2} <$ 120GeV and η_{probe} binning. It is important to remark that in the η_{probe} binning, the range of the gaussian fit applied was considered, i.e., only events with $|A| < 0.35$ were considered.

Finally, trigger prescales were also considered in this analysis, as they highly influence the statistics. In the considered range, LVL1 applies a prescale of 50, which means only one in every 50 events are actually kept.

The following table (table 5.5) summarizes the efficiencies (ϵ) obtained for each cut and the associated uncertainties ($\delta\epsilon$). Only two η_{probe} bins were analyzed: the reference bin and the bin $[-0.6, -0.3]$, which were the bins with the lowest and the highest statistics.

The efficiency of a particular cut is the ratio between the number events remaining after the cut and the number of events existing before the cut. In other words, suppose one has a sample with a total of N events, where a particular cut is applied. If m is the number of events that satisfy the selection criteria (that "pass the cut"), then $\epsilon = m/N$. The uncertainty of the efficiency, on the other hand, was calculated considering Poisson errors [62], i.e., $\delta\epsilon = \epsilon\sqrt{1+\epsilon}$.

Intercalibration in η of LVL2 Jets		
		$\epsilon \pm \delta\epsilon$
$E_t^{LVL1} > 70 GeV$ *threshold*		0.437 ± 0.002
At least two LVL2 jets per event		0.100 ± 0.004
$\lvert\Delta\phi\rvert \approx \pi$		0.410 ± 0.002
$p_t^{third} < 15 GeV$		0.660 ± 0.005
At least one leading jet as reference		0.120 ± 0.002
$p_t^{average}$ *binning*		0.53 ± 0.02
η_{probe} *binning with prescale*	*[0,0.3]*	0.0007 ± 0.0006
	[-0.6,-0.3]	0.0014 ± 0.0009
Total	*[0,0.3]*	0.0000053 ± 0.0000049
	[-0.6,-0.3]	0.000010 ± 0.000007

Table 5.5: Efficiencies and associated uncertainties of the cuts applied to LVL2 jets from QCD dijet events generated by PYTHIA when using the intercalibration in η method (trigger selection is included as well).

The cross section for jets in the conditions considered in the sample used in this analysis is $\sigma = 3.28 \times 10^6$pb. Let us consider m the number of events remaining in a particular η_{probe} bin after all cuts have been applied, but before prescale. Since $N = 224861$ events were produced, the efficiency of the cuts is given by $\epsilon = m/N$. The integrated luminosity necessary to produce events in these conditions is: $L = \int \mathcal{L} = \frac{m}{\epsilon\sigma} = 0.038\text{pb}^{-1}$. Since σ and ϵ are constant in the considered range, L/m is constant as well. This can also be written as $L/m = L'/m'$, where m' is the number of events obtained at a luminosity L' with the same cross section and efficiency considered for L and m.

The statistical relative uncertainty of m is $\delta_r m = \sqrt{m}/m$. However, because a prescale of 50 is applied by LVL1 (meaning the final number of events in the reference η_{probe} bin will actually be $n = m/50$), the final statistical error has to be rescaled. Thus, one has

$$\delta_r n = \frac{\sqrt{n}}{n} = \frac{\sqrt{m/50}}{m/50} = \frac{\sqrt{m}}{m}\sqrt{50} = \delta_r m\sqrt{50}$$

Because the prescale is constant in the considered conditions, $L/m = L'/m'$ can be written as $\delta_r n = \frac{L'}{L} \times \sqrt{\frac{L}{L'}} \times \delta_r n'$. In summary, it is possible to ex-

trapolate how the statistical uncertainty of the intercalibration in η method will decrease as the integrated luminosity in the LHC increases with data taking. This is shown in figure 5.10.

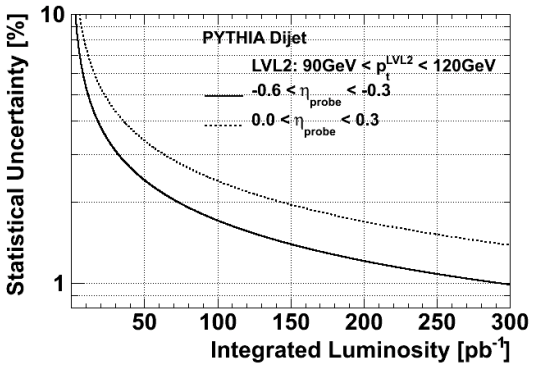

Figure 5.10: Distribution of $\Delta\phi$ between the two leading jets in QCD dijet events generated by PYTHIA.

Figure 5.10 shows that, after one year of data taking, corresponding to $\approx 200\text{pb}^{-1}$ of integrated luminosity, the statistical uncertainty in the low-statistics η_{probe} bin and for a low p_t range reaches practically 1%. Since it was already shown that the intercalibration in η method can, indeed, improve the uniformity of the jet energy scale, this was the final test that demonstrated this *in-situ* calibration method is viable and can be used in real data.

5.5 Summary and Conclusions

In this chapter a *in-situ* calibration method called intercalibration in η was presented. The method allows the validation and tuning of the hadronic calibration by evaluating and correcting the uniformity in η of the hadronic jet energy scale. It is a relative method, since probe jets are compared to reference jets and corrected with respect to these. The asymmetry variable is used as an indicator of the uniformity of the hadronic jet energy scale and of how good the hadronic calibration applied is.

The studies developed consisted of applying intercalibration in η to PYTHIA simulated dijet events. The goal was to determine whether the

method it could be used in the beginning of data taking to validate and tune, if necessary, the calibration applied to LVL2 trigger jets.

The *in-situ* method was first applied to truth jets. Because these jets constitute the reference for LVL2 calibration, this procedure allows the determination of the limitations of the method. In other words, if one assumes that the calibration applied to LVL2 jets is "perfect" then one should expect the asymmetries for LVL2 jets to be within the same ranges obtained for truth jets. The results showed that the asymmetries vary according to p_t of the jets and are usually lower for higher transverse momenta. Furthermore, the results suggested that A was slightly shifted towards positive values for high η_{probe} bins. This was considered a consequence of the fact that small cone algorithms may not collect all the energy of low momenta jets, because they are usually wider than high momenta jets.

The next step consisted of applying the in-situ calibration method to LVL2 jets. The asymmetries observed led to the conclusion that the calibration applied to these jets was not very good, since it did not produce a hadronic scale stable and uniform in η. Thus, intercalibration in η was then used to derive correction constants. The goal was to tune the calibration and try to improve the asymmetries.

The results obtained for the tuning of the hadronic calibration suggested that intercalibration in η can indeed improve the uniformity in η of the jet energy scale, since the asymmetries observed for the corrected LVL2 jets were reduced especially in the high p_t range.

The improvements in the asymmetry obtained with the correction constants derived from intercalibration in η suggested the method can improve the uniformity of the LVL2 jet energy scale. Since MonteCarlo simulated data was being used, the "new" LVL2 jet energy scale (i.e. corrected with the constants derived from intercalibration in η) could actually be evaluated by comparing the corrected energy of the LVL2 jets with the energy of the truth jets.

This final closure test confirmed that, indeed, intercalibration in η was able to improve the uniformity of the LVL2 jet energy scale, particularly in the high p_t bins, as had already been implied by the evaluation of the asymmetry. Even though the jet energy scale was not improved in the lowest p_t bin, we expect the LVL2 jet energy scale to be worst in the beginning of

data taking, particularly in the low p_t bins, in which case the corrections from intercalibration in η should be able to produce some improvements. Still it is important to note that the method did provide an energy scale within 1% for jets with $p_t^{LVL2} > 1000$GeV.

Since intercalibration in η was applied to MonteCarlo simulated data, the final step was trying to assess if the method could be applied to real data in the beginning of data taking. Thus, the efficiencies of the selection criteria required by the method were evaluated, as well as the variation of the statistical uncertainty of the method with the integrated luminosity at the LHC. It was observed that, for jets with 90GeV$< p_t <$ 120GeV, with $\approx 50\text{pb}^{-1}$ of integrated luminosity at the LHC, the statistical uncertainty of the method was $\approx 3\%$, which is comparable to the uncertainty of the LVL2 jet energy scale found for that p_t bin. Moreover, since the jet trigger menu applies thresholds and prescales in order to have a constant jet rate with p_t, similiar statistics and uncertainties are expected for the higher p_t bins.

Conclusions

This thesis presents two separate studies on the ATLAS jet trigger.

The first study compared trigger jets to offline reconstructed jets, in order to evaluate the performance of the three levels of the ATLAS jet trigger, and provided a good test of the quality of the data from cosmic muon runs. The overall workings of the ATLAS jet trigger system were analyzed. The method was simple and straightforward but allowed the identification of some problems. For example, noisy calorimeter cells were identified and jets reconstructed from these cells were eliminated so the subsequent analysis would not be biased. Also, LVL2 only applied calibration to jets with transverse energies above 20GeV, a behavior that has already been corrected. Finally, offline was overestimating the energy of jets identified in the extended barrel region of the TileCal and this problem has been solved as well. As for the reconstruction of the jets positions and energies results showed that each trigger level improves the reconstruction performed by the previous one, getting closer to offline. Globally, the trigger energy scale compared to offline was uniform and stable both in pseudorapidity and in transverse energy. In particular, LVL2 was reconstructing $\approx 95\%$ of the offline jet energy in the central pseudorapidity region of ATLAS.

The second study used PYTHIA simulated dijet events to assess if intercalibration in η could be used in trigger jets in the beginning of data taking, to validate and tune the calibration applied at LVL2. Validation and tuning with this in-situ calibration method were based on the evaluation and correction of the non-uniformities in η of the hadronic LVL2 jet energy scale. Results suggested that the calibration applied to the analyzed LVL2 jets was not perfect in the sense that it did not produce a uniform jet energy scale, calibrated to particle level. Consequently correction constants were

derived to tune the LVL2 calibration, which severely improved the LVL2 scale, particularly in the high transverse momentum bins, where an uncertainty of 1% in the energy scale was reached. Finally, the analysis showed that, with $\approx 50\text{pb}^{-1}$ of integrated luminosity at the LHC, a statistical uncertainty of 3% in the method could be achieved for jets with transverse momenta between 90GeV and 120GeV.

Bibliography

[1] B. Martin and G. Shaw, *Particle Physics*. The Manchester Physics Series. Wiley, 3^{rd} ed., 2008.

[2] D. Perkins, *Introduction to High Energy Physics*. Addison-Wesley Publishing Company, Inc., 1987.

[3] D. Griffiths, *Introduction to Elementary Particles*. Wiley-VCH, 2^{nd} ed., 2008.

[4] Particle Data Group Collaboration, S. Eidelman et al., *Review of Particle Physics*, Physics Letters B **667** (September, 2008) .

[5] D. R. Clements, *Jet Physics at ATLAS*. PhD thesis, University of Glasgow, June, 2008.

[6] P. D. B. Collins and A. D. Martin, *Hadron Interactions*. Graduate Student Series in Physics. Adam Hilger Ltd, Bristol, UK, 1984.

[7] V. Mukhanov, *Physical Foundations of Cosmology*. Cambridge University Press, Cambridge, UK, 2005.

[8] R. K. Ellis, W. J. Stirling, and B. R. Webber, *QCD and Collider Physics*. Cambridge Monographs on Particle Physics, Nuclear Physics and Cosmology. Cambridge University Press, Cambridge, UK, 1996.

[9] F. Halzen and A. Martin, *Quarks and Leptons: An Introductory Course in Modern Particle Physics*. John Wiley & Sons, Inc., 1984.

[10] R. Marshall, *Jets: the materialization of quarks and gluons*, Proc. R. Soc. Lond. A (1986) no. 404, 167–188.

[11] T. J. LeCompte, *QCD 101*, First ATLAS Physics Workshop of the Americas, SLAC, USA, August, 2007.

[12] D. Froidevaux and V. A. Mitsou, *Experimental prospects at the Large Hadron Collider*, J. Phys. Conf. Ser. **171** (2009) 012021, [arXiv:hep-ex/0905.0258].

[13] P. Weber, *ATLAS Calorimetry: Trigger, Simulation and Jet Calibration*. PhD thesis, Ruperto Carola University of Heidelberg, Germany, February, 2007.

[14] V. A. Abramovsky and N. V. Radchenko, *Multiplicity Distribution of Secondary Hadrons at LHC Energy and Total Cross Sections of Hadron-Hadron Interactions*, [arXiv:hep-ph/0812.2465].

[15] ATLAS Collaboration, *Introduction*, Expected Performance of the ATLAS Experiment: detector, trigger and physics (2008) no. CERN-OPEN-2008-020, , [arXiv:hep-ex/0901.0512].

[16] D. de Florian and M. Grazzini, *Higgs production through gluon fusion: updated cross sections at the Tevatron and the LHC*, Phys. Lett. **B674** (2009) 291–294, [arXiv:hep-ph/0901.2427].

[17] S. D. Ellis, J. Huston, K. Hatakeyama, P. Loch, and M. Tonnesmann, *Jets in hadron-hadron collisions*, Prog. Part. Nucl. Phys. **60** (2008) 484–551, [arXiv:hep-ph/0712.2447].

[18] G. P. Salam, *Towards Jetography*, [arXiv:hep-ph/0906.1833].

[19] G. C. Blazey et al., *Run II jet physics*, arXiv:[arXiv:hep-ex/0005012].

[20] P. Loch and M. Lefebvre, *Introduction to Hadronic Calibration in ATLAS*, Hadronic Calibration Workshop, Milano, Italy, April, 2007.

[21] C. Joram, L. Ropelewski, M. Moll, C. D'Ambrosio, T. Gys, and G. Mornacchi, *Particle detectors: principles and techniques. Detector techniques*, CERN, Geneva, April, 2005.

[22] P. Loch, *Introduction to Jet & Missing Transverse Energy Reconstruction in ATLAS*, ATLAS Hadronic Calibration Workshop, Foz do Arelho, Portugal, June 23, 2009.

[23] ATLAS Collaboration, *Jets and Missing Transverse Energy*, Expected Performance of the ATLAS Experiment: detector, trigger and physics (2008) no. CERN-OPEN-2008-020, , [arXiv:hep-ex/0901.0512].

[24] *CERN - the European Organization for Nuclear Research*, www.cern.ch.

[25] *LHC - Homepage*, http://lhc.web.cern.ch/lhc/.

[26] *CERN F.A.Q. - LHC: the guide*. CERN, Geneva, 2006.

[27] *CERN Press Office*, http://press.web.cern.ch/press/.

[28] O. S. Bruning, P. Collier, P. Lebrun, S. Myers, R. Ostojic, J. Poole, and P. Proudlock, *LHC Design Report*. CERN, Geneva, 2004.

[29] *ATLAS*, http://atlas.ch/,http://atlas.web.cern.ch/Atlas/index.html.

[30] *CMS Public Web Page*, http://cms.web.cern.ch/cms/index.html.

[31] *ALICE Public Web Page*, http://aliceinfo.cern.ch/Public/Welcome.html.

[32] *LHCb Public Web Page*, http://lhcb-public.web.cern.ch/lhcb%2Dpublic/.

[33] ATLAS Collaboration, *The ATLAS Experiment at the CERN Large Hadron Collider*, JINST (2008) no. **3**, S08003, .

[34] ATLAS Collaboration, *ATLAS Trigger Performance: Status Report*, Tech. Rep. CERN-LHCC-98-015, CERN, Geneva, Jun, 1998.

[35] ATLAS Collaboration, *Trigger*, Expected Performance of the ATLAS Experiment: detector, trigger and physics (2008) no. CERN-OPEN-2008-020, , [arXiv:hep-ex/0901.0512].

[36] R. Achenbach et al., *The ATLAS Level-1 Calorimeter Trigger*, Tech. Rep. ATL-DAQ-PUB-2008-001, ATL-COM-DAQ-2008-002, CERN, Geneva, January, 2008.

[37] D. Adams, D. Barberis, C. P. Bee, R. Hawkings, S. Jarp, R. Jones, D. Malon, L. Poggioli, G. Poulard, D. Quarrie, and T. Wenaus, *The ATLAS Computing Model*, Tech. Rep. ATL-SOFT-2004-007, ATL-COM-SOFT-2004-009, CERN-ATL-COM-SOFT-2004-009, CERN-LHCC-2004-037-G-085, CERN, Geneva, December, 2004.

[38] *The ATLAS Computing Workbook*, `https://twiki.cern.ch/twiki/bin/view/Atlas/WorkBook`.

[39] P. Conde-Muíño, *Implementation and Performance of the ATLAS Jet Trigger*, Tech. Rep. ATL-DAQ-PROC-2009-029, ATL-COM-DAQ-2009-112, CERN, Geneva, September, 2009.

[40] J. P. Dishaw, *The Production of Neutrinos and Neutrino Like Particles in Proton - Nucleus Interactions*, FERMILAB-THESIS-1979-08.

[41] I. Abt et al., *The tracking, calorimeter and muon detectors of the H1 experiment at HERA*, Nuclear Instruments and Methods in Physics Research Section A: Accelerators, Spectrometers, Detectors and Associated Equipment **386** (1997) no. 2-3, 348 – 396.

[42] A. Watson, *Private Communication*, .

[43] P. Conde-Muíño, I. Aracena, B. Brelier, K. Cranmer, P. A. Delsart, M. A. Dufour, S. Eckweiler, J. Ferland, J. Idarraga, K. Johns, T. LeCompte, C. Potter, S. Robertson, C. Santamarina-Rios, E. Segura, D. Silverstein, and B. Vachon, *Implementation and Performance of the ATLAS Second Level Jet Trigger*, J. Phys.: Conf. Ser. **119** (September, 2007) 022029. 7 p.

[44] N. Anjos, P. Conde-Muíño, I. Aracena, C. Santamarina-Rios, and M. Schram, *Hadronic Calibration for the ATLAS Jet Trigger*, Tech. Rep. ATL-DAQ-PROC-2009-001, ATL-COM-DAQ-2008-019, CERN, Geneva, December, 2008.

[45] A. Sen-Gupta, F. S. Merritt, and J. Proudfoot, *Jet Energy Correction Using Longitudinal Weighting*, Tech. Rep. ATL-COM-PHYS-2006-062, CERN, Geneva, Aug, 2006.

[46] G. Kertzscher, *Jet Trigger Proposal*, Trigger menus meeting, CERN, Geneva, June 6, 2009.

[47] 10^{31} *Trigger Menu justification documentation*, `https://twiki.cern.ch/twiki/bin/view/Atlas/L31TriggerMenu`.

[48] J. Maneira, *Commissioning of the ATLAS offline software with cosmic rays*, October, 2007.

[49] *Commissioning of the ATLAS high-level trigger with single beam and cosmic rays*, Tech. Rep. ATL-DAQ-PROC-2009-007, ATL-COM-DAQ-2009-028, CERN, Geneva, April, 2009.

[50] A. Di Mattia, *Commissioning of the ATLAS High Level Trigger with Single Beam and Cosmic Rays*, Tech. Rep. ATL-DAQ-PROC-2009-013, ATL-COM-DAQ-2009-037, CERN, Geneva, May, 2009.

[51] *Preliminary Results from Highly Energetic Cosmic Rays in the ATLAS Calorimeter*, `https://twiki.cern.ch/twiki/bin/view/Atlas/ApprovedCosmicPlotsJetEtMiss`.

[52] *AMI - ATLAS Metadata Interface*, `http://ami.in2p3.fr/opencms/opencms/AMI/www/`.

[53] *Run Details for Run 90272*, `http://atlas-service-db-runlist.web.cern.ch/atlas-service-db-runlist/php/runDetails.php?run=90272`.

[54] J. T. Shank, *The ATLAS Detector: Status and Results from Cosmic Rays*, `[arXiv:hep-ex/0910.3081]`.

[55] D. Oliveira Damazio, *ATLAS High Level Calorimeter Trigger Software Performance for Cosmic Ray Events*, Tech. Rep. ATL-DAQ-PROC-2009-020, ATL-COM-DAQ-2009-045, CERN, Geneva, May, 2009.

[56] J. Edsjo, E. Lundstrom, S. Rydbeck, and J. Sjolin, *Early search for supersymmetric dark matter models at the LHC without missing energy*, [arXiv:hep-ph/0910.1106].

[57] V. Rossetti, *Understanding the Jet Trigger and the Calorimeters with Cosmic Data*, Jet slice meeting, cern, geneva, May 12, 2009. http://indico.cern.ch/getFile.py/access?contribId=8&resId=0&materialId=slides&confId=50131.

[58] T. Sjostrand, S. Mrenna, and P. Skands, *PYTHIA 6.4 Physics and Manual*, JHEP **05** (2006) 026, [arXix:hep-ph/0603175].

[59] *PYTHIA*, http://home.thep.lu.se/~torbjorn/Pythia.html.

[60] *ATLAS Detector Simulation with Geant4*, https://twiki.cern.ch/twiki/bin/view/Atlas/AtlasG4Simulation.

[61] E. S. i Solé, *Simulation of the Measurement of the Inclusive Jet Cross Sections in $Z(\rightarrow e^+e^-/\rightarrow \mu^+\mu^-)$+jets Events in pp Collisions at 14TeV with the ATLAS experiment.* PhD thesis, Institut de Física d'Altes Energies - Universitat Autònoma de Barcelona, June, 2009.

[62] M. Paterno, *Calculating Efficiencies and Their Uncertainties*, February, 1996.